Max-Planck-Institut für Meteorologie
Max Planck Institute for Meteorology

Examensarbeit Nr. 86

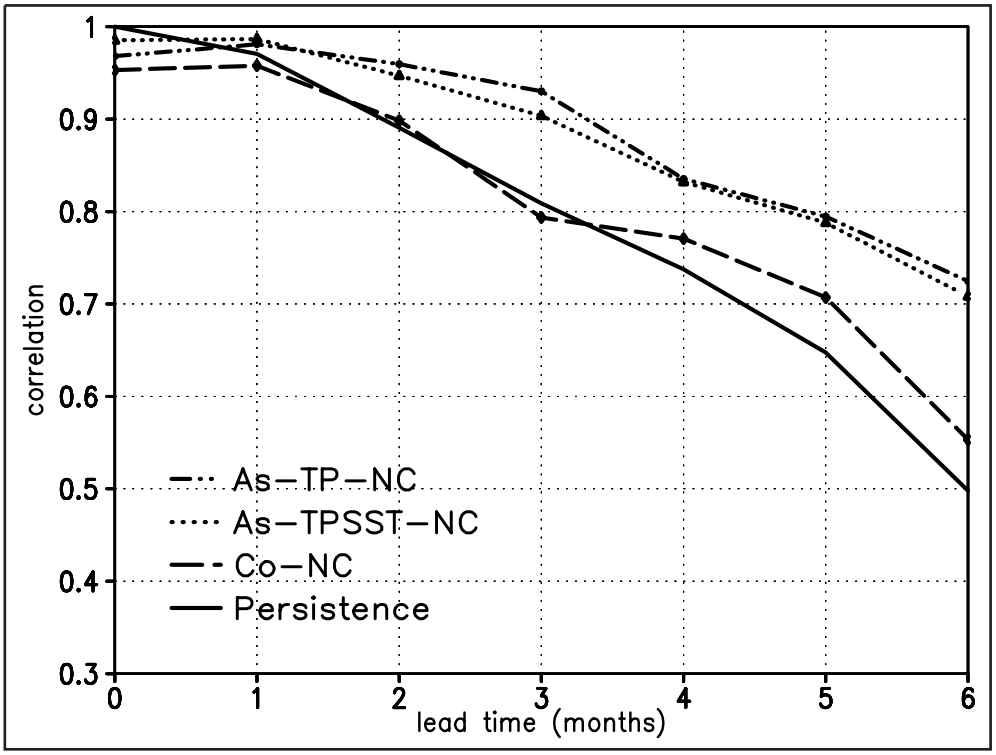

The Impact of Sea Surface Height Data Assimilation on El Niño Analyses and Forecasts

(Auswirkungen der Assimilation von Meereshöhen-Daten auf Analysen und Vorhersagen von El Niño)

von

Sigrid Schöttle

Hamburg, April 2002

Dissertation zur Erlangung des Doktorgrades

Autorin:

Sigrid Schöttle Max-Planck-Institut für Meteorologie

Max-Planck-Institut für Meteorologie
Bundesstrasse 55
D - 20146 Hamburg
Germany

Tel.: +49-(0)40-4 11 73-0
Fax: +49-(0)40-4 11 73-298
e-mail: <name>@dkrz.de
Web: www.mpimet.mpg.de

The Impact of Sea Surface Height Data Assimilation on El Niño Analyses and Forecasts

(Auswirkungen der Assimilation von Meereshöhen-Daten
auf Analysen und Vorhersagen von El Niño)

Dissertation zur Erlangung des Doktorgrades
der Naturwissenschaften im Fachbereich
Geowissenschaften
der Universität Hamburg

vorgelegt von
Sigrid Schöttle
aus Hamburg

Hamburg
2002

ISSN 0938-5177

Als Dissertation angenommen vom Fachbereich Geowissenschaften
der Universität Hamburg

auf Grund der Gutachten von Dr. habil. Mojib Latif
und Prof. Dr. Werner Alpers

Hamburg, den

Prof. Dr. Ulrich Bismayer
(Dekan des Fachbereichs Geowissenschaften)

Abstract

This thesis investigates the impact of sea surface height (SSH) data assimilation on El Niño simulations and forecasts. SSH measured by the Topex/Poseidon (T/P) altimeters were assimilated into the Pacific version of the E-HOPE ocean general circulation model (OGCM). The method of assimilation is based on the projection of the sea surface heights at each grid point onto the first two leading vertical empirical orthogonal functions (EOF) of temperature. Assimilation of T/P data reduced the errors of the ocean simulations that were used later on for initialisation of the coupled model forecasts. Remaining errors in the ocean simulations were identified to be invoked by unrealistic fresh water flux estimates of the simulation itself. Tests with projections onto both, temperature and salinity EOFs together, were less satisfying.

Coupled model integrations were performed with the OGCM coupled to a statistical atmosphere model to investigate the ENSO forecast skill. The initial conditions for the coupled integrations were taken from ocean simulations with and without T/P data assimilation and from ocean simulations with assimilation of TAO/TRITON data. Furthermore, the sensitivity of the El Niño simulations and forecasts to bivariate data assimilation, using SSH and sea surface temperatures (SST) together, was tested. Assimilation of T/P SSH generally led to an improved ENSO forecast skill. Both TAO/TRITON as well as bivariate data assimilation yielded a similar skill improvement.

A sensitivity study with different atmospheric forcing data sets showed that the choice of the atmospheric forcing considerably influences the ocean initialisation runs and the coupled model forecasts. Furthermore, comparison of two experiments with assimilation of SSH data which differ only in their forcing data sets showed that the errors of the atmospheric forcings were corrected by assimilation of SSH data.

Contents

Chapter 1

Introduction

Forecasts of the El Niño-Southern Oscillation (ENSO) phenomenon span a time range of a few months up to two years ahead and thus fall in the group of seasonal climate predictions. Weather, in contrast, as it is known from everybody's daily experience, has a much more limited predictability. As the evolution of weather is chaotic in nature, individual weather phenomena are on average only predictable up to two weeks ahead. Seasonal climate prediction itself is a natural extension of numerical weather prediction (NWP). In contrast to NWP, seasonal climate prediction does not attempt to predict individual weather phenomena. The predicted quantities dealt with on these longer time scales are rather "mean quantities", i.e. quantities averaged over months or seasons, like seasonal rainfall or temperature.

Seasonal climate prediction requires the development of coupled ocean-atmosphere models which need to be initialised adequately. The memory of the system resides in the slowly responding components of the climate system (Hasselmann, 1976). For the ENSO phenomenon the ocean constitutes this component (Neelin et al., 1998) so that ocean measurements are crucial in the initialisation of the coupled model forecasts. In particular, the lower boundary conditions of the atmosphere, the sea surface temperature (SST), may determine its evolution on seasonal and longer time scales. Thus, if it is possible to predict the SSTs several months ahead, the state of the atmosphere may be predictable, too. In the tropics, the SST have a rather strong impact on the atmosphere. In the midlatitudes, however, a much more chaotic character of flow prevails. Therefore, short-range climate

predictions are most successful in the tropics.

This work investigates the impact of sea surface height (SSH) data assimilation on ENSO forecasts, which brings together 3 big issues: the ENSO phenomenon spreading half way around the world in the tropics with disastrous consequences in some regions; the extremely precise measurements of SSH from the Topex/Poseidon (T/P) satellite mission, measuring the SSH with an accuracy of 2 cm from an orbit of 1336 km above the earth's surface; and the bringing together of the T/P measurements and the ENSO phenomenon through the assimilation of SSH data into an ocean general circulation model.

The ENSO phenomenon itself is the strongest climate variation on the short-term climatic timescale ranging from a few months to several years. ENSO results from the coupled interaction between ocean and atmosphere and is characterised by an irregular interannual oscillation of eastern tropical Pacific SST. Anomalously warm SST in the eastern Pacific invoke a weakening of the atmospheric Walker circulation (whose lower branch is formed by the trade winds) and anomalously cold SST an intensification of the Walker circulation. The warm phase is referred to as "El Niño" and the cold phase as "La Niña". As mentioned before, the memory of this coupled system is believed to reside within the ocean. The importance of this oceanic subsurface memory has been shown in many observational and modelling studies (e.g.: Wyrtki, 1975; White et al., 1987; Latif and Graham, 1992; McPhaden et al., 1998) and this forms the basis of this work. For further characteristics of ENSO the reader is referred to Philander (1990), Schöttle (1997) (in German) and Rothstein et al. (1998) and references therein.

Although ENSO originates in the tropical Pacific, it affects not only regional but also global climate (e.g. Trenberth et al., 1998). Furthermore, ENSO-related climate anomalies also influence the ecosystem in and around the tropical Pacific and the economies of several countries, for example Australia, Indonesia and Peru. The successful prediction of ENSO is therefore not only of scientific but also of practical interest.

From SSH as provided by the Topex/Poseidon (T/P) satellite, an estimation of the vertically integrated density over the whole water column can be derived. As density variations in the region of the tropical Pacific are primarily dependent on temperature changes (e.g. Chambers et al., 1998) and the strongest temperature changes occur in the upper 200 m (McPhaden et al., 1998), variations of SSHs are mainly induced by these upper ocean tem-

perature variations. These thermal variations are in turn precursors of ENSO extremes (White et al., 1987; Latif and Graham, 1992), which is referred to as the "subsurface memory paradigm" (Neelin et al., 1998). The T/P SSH data might thus contain precursors of changes in the state of ENSO and has the potential to improve the initialisation of ocean models. Therefore they can be valuable for ENSO forecasting.

The difficulty of assimilating SSH data lies in the projection of the surface signal onto the subsurface density structure. Numerous papers have been published in the field of SSH assimilation into ocean models. Some have focused on improving the simulation of the dynamics in higher latitudes (e.g.: Stammer and Wunsch, 1996; Oschlies and Willebrand, 1996; Gavart and De Mey, 1997), while others have focused on the tropics (e.g.: Carton et al., 1996; Fischer et al., 1997; Segschneider et al., 2000a; Ji et al., 2000). Studies assimilating T/P data in the tropical Pacific found that the assimilation can help to resolve major features of the seasonal cycle (Carton et al., 1996) and that improvements of sea level variability can be obtained, although inadequate salinity information still limit the accuracy in temperature (Ji et al., 2000).

Here, the main goal is to provide improved ocean initial conditions for hybrid coupled ocean-atmosphere forecast experiments. The improved ocean initial conditions should correct for errors in the ocean thermal field that are caused by model errors or by errors in the atmospheric forcing. The improved representation of the ocean model's upper ocean heat content should then lead to improved forecasts made by the coupled system. The assimilation of altimeter-observed SSH anomalies in this context has also been performed by Fischer (1996), Segschneider et al. (2000a), Segschneider et al. (2000b) and Perigaud et al. (2000).

Perigaud et al. (2000) used an intermediate coupled model to test several techniques for model initialisation with sea level data including the Kalman Filter, but none of them led to improved forecasts. This suggested that more complete physics than included in the intermediate model are needed for climate predictions. The studies of Segschneider et al. (1999, 2000a and 2000b) are all based on vertical shifts of the model's local temperature and in the latest paper also of an adjustment of the salinity in order to match the observed sea level, based on the assimilation technique of Cooper and Haines (1996) and the extension by Troccoli and Haines (1999).

Apart from this technique, which results in squeezing or stretching of the water masses, another major group of projection techniques is based on the statistical relationships between the sea surface height and the subsurface structures. Mellor and Ezer (1991), Rienecker and Adamec (1995), Fischer (1996), Gavart and De Mey (1997), Fischer et al. (1997) and Fischer (2000) use previously calculated statistical relations between either the subsurface temperature and salinity anomalies directly (Mellor and Ezer, 1991), the EOFs of temperature only, or the combined EOFs of temperature and salinity at every ocean water column and the corresponding SSH anomalies. The projection of the SSHs onto the leading EOF modes of variability also has the advantage of filtering noise from the system.

Based on such a statistical method using EOFs, Fischer et al. (1997) assimilated SSH into a primitive equation model of the tropical Pacific, using a successive correction scheme. They have found that the benefit of assimilating either SSHs or subsurface temperatures is comparable for the purposes of ENSO prediction. However, the interpretation of forecast results also depended critically on the definition of the measure of skill. Furthermore, Fischer (1996) highlighted that altimeter data with their high temporal and spatial resolution can be useful for El Niño investigations.

Until now, the statistical projection has neither been used with a high precision dataset as that of Topex/Poseidon nor a dataset covering a period of more than 3 years. Here, the statistical projection scheme using EOFs of temperature is applied using the Topex/Poseidon data, covering a period of about 8 years. This relatively long period of continuous altimeter measurements allows better statistical evaluations of the results than any of the shorter periods of previous altimeter missions.

For in situ measurements of subsurface temperature, the "TAO/TRITON buoy array" (McPhaden et al., 1998) has been installed in the tropical Pacific. However, buoys are expensive to deploy and maintain, and are hence only sparsely distributed. Satellite measurements, on the other hand, provide only indirect measurements of subsurface structures, but they have the advantages of near global and high spatial resolution, combined with less maintenance effort compared to an equivalent global buoy measurement system. Also, with a 10-day repeat cycle, as in the case of the T/P satellite, a relatively high temporal resolution is still obtained. In order to compare the impacts of both measurement systems on ENSO simulations and forecasts, both datasets are assimilated separately. Ocean only

as well as coupled forecast simulations are performed and discussed within this thesis.

Fischer et al. (1997) also found that results with assimilation of SSH only, sometimes appeared to be even worse than those without assimilation. In a subsequent paper, Fischer (2000) suggested that a multivariate projection, using SSH together with SST, improves ocean initial conditions. This is especially the case, when precursors of ENSO events in form of temperature anomalies are already to be seen in the subsurface. However, whether the improvements of the ocean initial conditions by this multivariate projection improve the ENSO forecast skill remained an open question. This question is also addressed in this thesis.

Any simulation with an ocean model requires the specification of forcing fields at the surface of the ocean, and it is these fields that drive and largely determine the behaviour of the ocean model (Stockdale et al., 1998). Therefore the sensitivity of the results to different atmospheric forcing fields has been additionally tested in this study.

Throughout this work, "forecast" and "prediction" are used synonymously and both are referring to retrospective forecasting. Forecasts into the real future were only performed once, in boreal summer 2000, when the ocean state within the tropical Pacific suggested a high potential for an approaching El Niño event (Schöttle and Latif, 2000).

The structure of this thesis is as follows: the data which are used within this study are described in chapter 2; the ocean and atmosphere models with which the simulations are performed are presented in chapter 3; chapter 4 describes the methods of assimilation and chapters 5, 6 and 7 the results. A comprehensive summary, a discussion and an outlook are given in chapter 8.

Chapter 2

Data: Characteristics and Preparation

Observations are used for three different purposes in this study: to force the ocean model, to assimilate the data into the model, and to validate the results. The four data products used in this study are the sea level data derived from the Topex/Poseidon (T/P) satellite mission (AVISO, 1998b), the in situ measured temperature data from the TAO/TRITON buoy array (McPhaden et al., 1998) and the atmospheric data sets from the ECMWF[1] (Gibson et al., 1999) and NCEP/NCAR[2] (Kalnay et al., 1996) re-analyses projects. All of these data sets are derived from observations, but they differ a lot in the extent of their processing. It ranges from quality control for the TAO/TRITON data up to a mixture of model and observed data for the re-analysis products.

2.1 TOPEX/POSEIDON Altimeter Data

From sea surface heights (SSH) as provided by the T/P satellite an estimation of the vertically integrated density over the whole water column can be derived. This measure contains precursors of changes in the state of ENSO and can thus be valuable for ENSO forecasting (Neelin et al., 1998). ENSO precursors are in particular to be found in the

[1] European Centre for Medium-Range Weather Forecasting

[2] National Centers for Environmental Prediction/National Center for Atmospheric Research

Investigated Aspect of the Signal	Derived Geophysical Quantity
return time	geoid undulation, rotation of the earth, bottom topography, barotropic and baroclinic ocean tides, ocean circulation, wave dynamics, oceanic heat content
form of rising edge	significant wave height, ice coverage
amplitude	ocean surface winds, precipitation

Table 2.1: *Geophysical quantities and phenomena, which are investigated by means of altimeter signals (after Esselborn, 2001).*

thermal field of the upper 200 m (McPhaden et al., 1998). Therefore also in situ measured temperatures like those of the TAO/TRITON buoy array can help to predict ENSO, but in contrast to satellite data they are expensive to deploy and maintain and cannot provide the high spatial resolution of T/P satellite data. Hence, although a surface parameter, the SSH allows a look into the ocean interior whose utility for ENSO predictability is investigated in this study.

2.1.1 Method of Measurement/ The Satellite

An altimeter is an active microwave radiometer emitting electromagnetic pulses perpendicular to the surface of the earth and receiving the backscattered signal. Three different aspects of the backscattered signal are generally investigated, the return time, the shape of the signal and the amplitude. The geophysical quantities which can generally be derived from these aspects are listed in table 2.1.

By recording the return time of the electromagnetic pulse the range between the satellite and the ocean surface can be determined. A number of geophysical quantities and corrections are necessary to translate these observations into a real sea surface topography (i.e. the deviation of the sea surface from the hypothetical surface of an ocean at rest, see figure 2.1), which should at the end depend on nothing but the actual ocean state. These geophysical quantities and corrections are listed in table 2.2.

In October 1992 the American National Aeronautics and Space Administration (NASA)

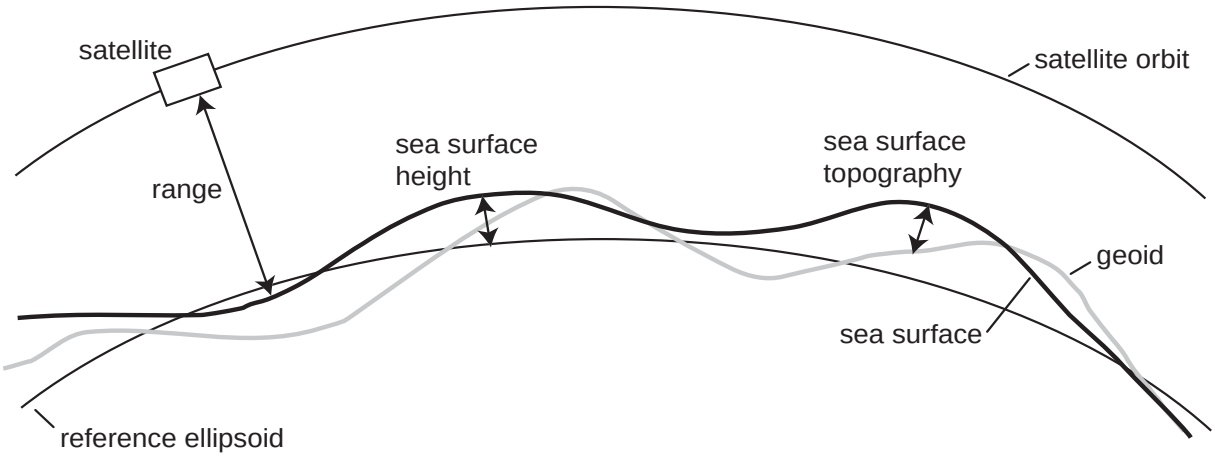

Figure 2.1: *Phrases used in connection with altimeter measurements and corrections.*

together with the French "Centre National d'Études Spatiales" (CNES) launched a satellite carrying two altimeters on board: the American "ocean TOPographic EXperiment" altimeter TOPEX and the French altimeter POSEIDON. The TOPEX altimeter measures at two frequencies with the advantage that this allows for reduction of errors due to free electrons, which emerge when the radar pulse travels through the ionosphere.

Further payload of the satellite consists of a microwave radiometer to measure the atmospheric water content and three instruments for precise orbit determination. These are a Global Positioning System (GPS) receiver, a laser retroreflector array and the microwave Doppler DORIS (Détermination d'Orbite et Radiopositionnement Intégrés par Satellite) (Fu et al., 1994; AVISO, 1996).

The TOPEX/POSEIDON satellite delivers data with an unprecedented accuracy (Fu et al., 1994). For all altimeter missions before, the uncertainty of orbit determination was the predominant error of sea level measurements. The satellite's comprehensive tracking system as described above together with an improved knowledge of the earth's gravitational field lead to an orbit accuracy which is approaching the other measurement uncertainties of the TOPEX/POSEIDON altimeters. This high orbit precision in turn with the high performance of the two altimeters are the reason that TOPEX/POSEIDON delivers altimeter observations with the smallest errors compared to previous altimeter satellite missions.

Several studies investigated the accuracy of the T/P altimeter data (e.g.: Fu et al., 1994; Shum et al., 1995; AVISO, 1999, 2001). With improved correction terms, the accuracy of

denotation:	correcting for:
sensor bias correction	instrumental bias of radiometer
dry and wet tropospheric corrections	distortion of the signal in the troposphere
ocean wave correction	over-estimation of sea surface topography due to waves
solar and lunar ocean tides	part of the signal induced by these tidal constituents
tidal loading	effect on SSH by the force activated by tides on the ocean sea floor
solid earth tides	part of the signal induced by solar and lunar tides of the solid earth
pole tide	changing centrifugal force due to oscillation of the earth's rotational axis
inverse barometer effect	SSH being pushed by changing atmospheric pressure

Table 2.2: *Correction terms and geophysical quantities which have to be accounted for when SSH are estimated from the satellite range.*

SSH determination was enhanced from about 5 cm in the early years of the T/P satellite (Fu et al., 1994; Shum et al., 1995) to 3 to 4 cm later on (AVISO, 1999, 2001). For the tropical Pacific region, where this study focuses on, special surveys have been performed. In particular, the RMS difference at two stations in the western tropical Pacific between the altimeter data and in situ measurements of moorings and inverted echo sounders was estimated to about 2 to 3 cm. Furthermore, the precision of the altimeter signal has been found to be statistically indistinguishable from the one of in situ measurement methods for the frequencies resolvable by the altimeter (Katz et al., 1995; Picaut et al., 1995).

2.1.2 Data Processing at CLS

The TOPEX/POSEIDON data used in this study were obtained from the company "Collecte Localisation Satellite" (CLS) located in Toulouse, France. The data were processed

there in three steps.

First the original along-track data are quality controlled, validated and geophysical corrections like improved orbit corrections, the latest state of the art models (e.g. ocean tide models) and homogeneous corrections (concerning environmental perturbations of the radar pulse e.g. in the troposphere) are applied. The obtained dataset is called Corrected Sea Surface Heights (CORSSH) (AVISO, 1998a).
Next, the data are subjected to a repeat-track analysis method. For a given track and for each cycle, corrected data are re-sampled every 7 km using cubic spline and differences relative to a 3-year mean from January 1993 to December 1995 (AVISO, 1998b). The data are referenced relative to this 3-year mean rather than to the geoid as the geoid is the primary limitation in the measurement of the sea surface topography. The resulting dataset is called Sea Level Anomalies by CLS. Here, they are termed Sea Level Deviations (SLD), to distinguish these data relative to a long-term mean from data relative to the annual cycle, for which the term SLA is used.
The third step is a mapping of the data. A newly developed space/time objective analysis method is applied to the data. This method accounts for long wavelength errors denoting inconsistencies between neighbouring tracks due to orbit error, residual tidal error and inverted barometer errors (Le Traon et al., 1998).

The obtained maps of SLD have a spatial resolution of $1/4^\circ \times 1/4^\circ$, a temporal one of approximately 10 days and are called Historical Homogeneous (HH) data. In this study the HH data are used for the period October 1992 until the middle of January 2000. For the time from January 2000 until the end of June 2000 T/P, near real time (NRT) data have been used, as the HH data for this period have not been available at the start time of the experiments. The NRT data are identically processed like the HH data, except that a less precise orbit has to be taken into account. This less precise orbit is due to the quick processing time of just 2 days after measurement. Therefore an orbit error correction by crossover minimisation together with a subtraction of the along-track bias is applied additionally. The latter one is based on the mapping method described in Le Traon et al. (1998). The main difference is that, instead of mapping the oceanic signal, the along-track bias is calculated directly for each track.

2.1.3 Additional Data Processing

The mapped data provided by CLS cannot directly be used for the assimilation. Before they are in a first step interpolated onto the ocean model grid by box averaging. This method has been chosen as the original $1/4^\circ \times 1/4^\circ$ resolution of the CLS data is much finer than the ocean model grid (see chapter 3.1).

As a second step the annual cycle of the T/P data is estimated. Our assimilation method is based on anomalies with respect to a mean annual cycle, while the T/P data supplied by CLS are deviations with respect to a 3-year mean. Therefore, a good estimate of the climatological annual cycle of sea level is needed. The climatological annual cycle is usually computed using monthly data of a long period (about 30 years) and averaging these data for each calendar month of the year. The 5 years of sea level data which were available for this calculation are such a short period that it does not provide a reliable estimate of the annual cycle.

To improve the quality of the estimated annual cycle we computed the annual cycle by fitting a Fourier series with a period of one year to the T/P data using a least square fitting method based on singular value decomposition (SVD) of the normal equation (Press et al., 1988). The resulting annual cycle for the Niño3 index region (150°W-90°W, 5°N-5°S) is shown in figure 2.2, where the base period and 4 harmonics are used to estimate the annual cycle. The figure also highlights a basic problem of the assimilation method used in this study which is based on anomalies. The estimates of the annual cycle in the Niño3 region are quite different depending on whether the strong El Niño year 1997 is included or not. For example, at the end of the 4th year, only a minor anomaly would be assimilated when the annual cycle is estimated from the four year period. If, however, all 5 years of data are considered for the estimate of the annual cycle, a strong negative anomaly would be assimilated in the Niño3 region. One should keep in mind that, the selected region, Niño3, shows the strongest interannual signal which makes the estimate particularly difficult. Here, the SLA are calculated with respect to the annual cycle estimated from the four year period.

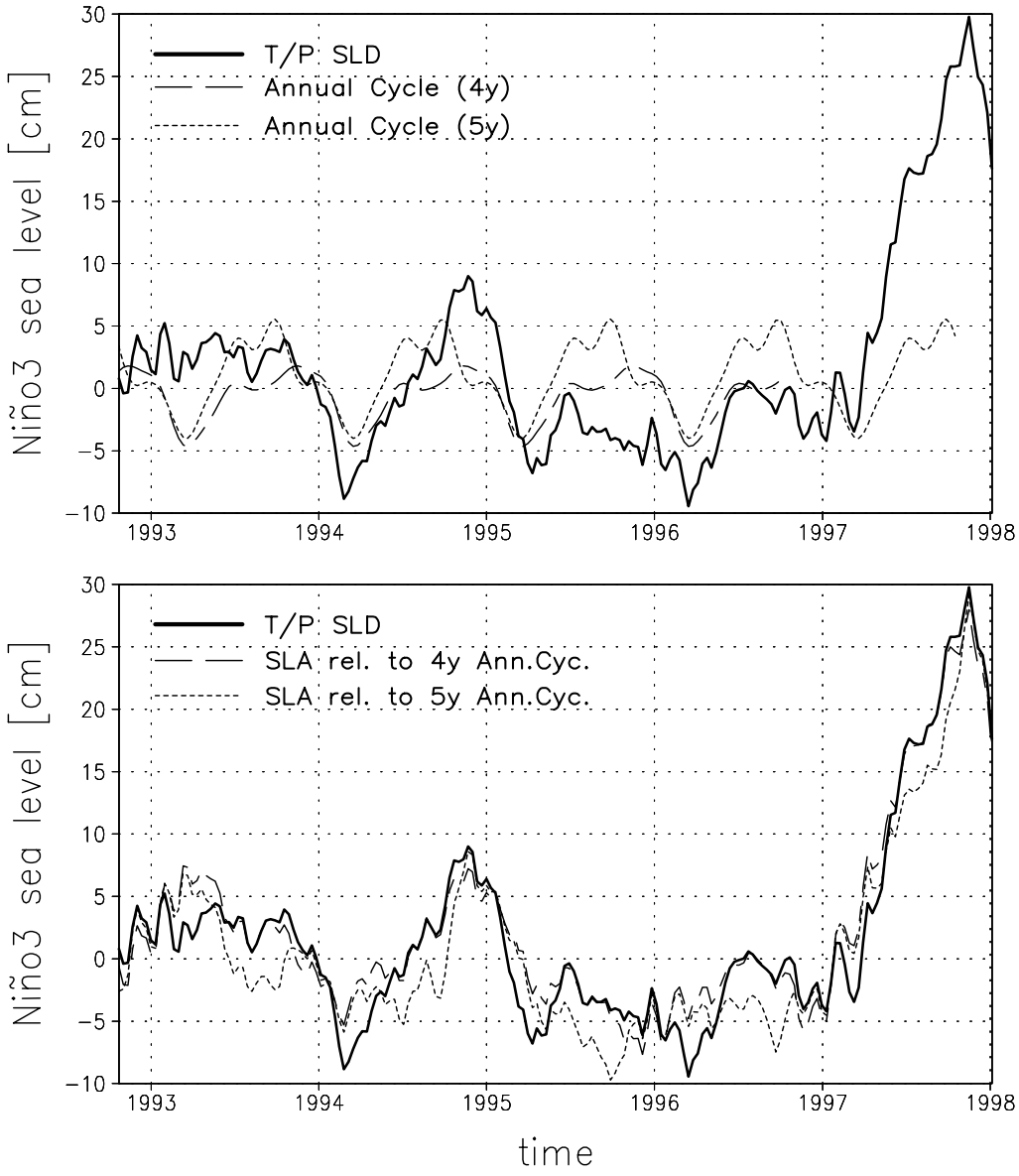

Figure 2.2: *Sea level deviation in the Niño3 region. Upper panel: full data (solid line), estimated annual cycle from four years (long dashes) and from five years (short dashes). Lower panel: full data (solid line), anomalies with respect to the annual cycle over the first 4 years of data (long dashes) and over the first 5 years of data (short dashes).*

2.2 TAO/TRITON Temperature Data

The subsurface temperature measurements which are used in this study were derived from a network of buoys in the tropical Pacific, firstly called the Tropical Atmosphere Ocean (TAO) array. They are utilised here for comparison with model data as well as to assimilate them into the ocean model.

2.2.1 The TAO/TRITON Buoy Array

The motivation to develop the TAO array arose from the 1982-1983 El Niño event, the strongest of the century up to that time, which was neither predicted nor detected until nearly at its peak. The event highlighted the need for real-time data from the tropical Pacific for both monitoring, prediction, and improved understanding of El Niño (Rothstein et al., 1998). In 1985 the first buoys were installed within the 10-year (1985-94) international Tropical Ocean Global Atmosphere (TOGA) program (McPhaden et al., 1998).

After TOGA ended in 1994, the TAO array continued under sponsorship of the international Climate Variability and Predictability (CLIVAR) program, the Global Ocean Observing System (GOOS), and the Global Climate Observing System (GCOS). In January 2000, the TAO array officially became the TAO/TRITON array, with sites west of 165°E occupied by TRITON (Triangle Trans Ocean Buoy Network) buoys maintained by the Japan Science and Technology Center (JAMSTEC). The whole array currently consists of about 70 buoys as shown in figure 2.3. The thermistors are installed so as to optimally resolve the vertical temperature structure at each station. Thus for layers with larger temperature gradients more thermistors are available. Due to the different depths of the thermocline in the eastern and western equatorial Pacific, the measurement depths can mainly be subdivided into one eastern and one western arrangement.

Additional to the temperature measurements used in this work, the TAO/TRITON array also measures winds, relative humidity and air temperature operationally. Five moorings along the equator also measure ocean velocity with acoustic doppler current profilers (ADCP).

The temperature sensors measure the water temperature once every ten minutes. These

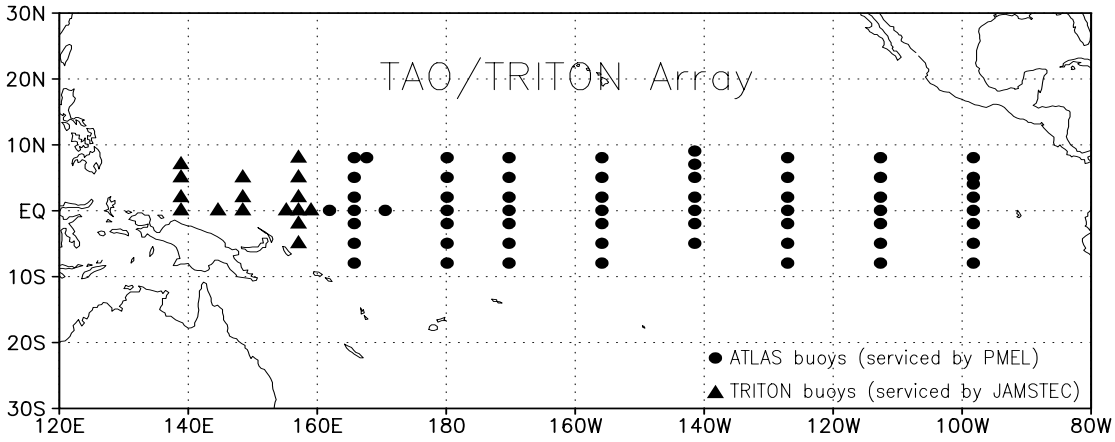

Figure 2.3: *Map of the TAO/TRITON buoy array. All of the depicted buoys delivered data for the period October 1992 to June 2000, which are used in this study.*

measurements are resolved with 0.001°C in the range between 6 and 32°C with an accuracy of ±0.09°C for older systems and ±0.01°C for newer systems. In spring 2001 already half of the moorings in the TAO/TRITON array use the newer technology. It is planned that all moorings will be next generation systems by 2002.

2.2.2 Data Processing

Daily mean values from the array are telemetered in near-real-time via satellites. The buoy data are processed every night by the TAO Project at the Pacific Marine Environmental Laboratory (PMEL), where calibration coefficients and quality controls are applied, and the data are finally made available.

For this study only these data are vertically interpolated onto the levels of the ocean model. As there are more levels with measurements for the buoys (up to 19 per station) than there are levels of the ocean model down to 500m depth (12 levels), a refined box averaging method has been used to interpolate the data. Normally, a box averaging method has got one defined value for the minimum percentage (mp) of area to be covered with defined data boxes. In this case, this mp value has been set to different values in different regions. For example, in depths with small temperature gradients a low coverage is sufficient, whereas in regions with large temperature gradients a high coverage is necessary. As the depth of largest gradient shows the largest differences between eastern and western sites, the mp

value is defined for each level and eastern and western conditions separately. The horizontal interpolation is part of the assimilation scheme and discussed in chapter 4.4.

2.3 NCEP/ECMWF Re-Analysis Data

Ocean model simulations need atmospheric forcing fields on a regular grid and in a temporally consistent form. Observations generally do not meet these requirements as they are often neither homogeneous in time nor in space. Therefore so-called re-analysis projects are carried out by two weather prediction centers. For these projects all obtainable observations are assimilated in one weather prediction model for a long period. The observations are mainly from satellites, aircrafts, radiosondes and land- and ship-based measurements. For consistency the formulation of the model is kept constant over the whole time. The calculated atmospheric variables are thus temporally consistent and regularly gridded.

Data from two re-analysis projects are used within this study. One is the NCEP/NCAR re-analysis project, the other the ECMWF re-analysis (ERA-15) project. The NCEP/NCAR re-analysis project covers a period of 40 years (1958 - 1997). The atmospheric model used for this re-analysis has got a horizontal spectral resolution of T62, corresponding to a Gaussian grid resolution of 1.875° or about 208 km and a vertical resolution of 28 layers (Kalnay et al., 1996). Daily data output is used for the experiments carried out here. Secondly, the ECMWF re-analysis project covers data over a period of 15 years (1979 - 1993). An ECMWF re-analysis project covering a longer period (40 years) is underway but not yet available. ECMWF analysis data are used for the time of 1994 and onwards, which implies updates of the atmosphere model code and thus from time to time temporally inconsistent data fields. The ECMWF data were accomplished with a horizontal spectral resolution of T106, corresponding to a Gaussian grid resolution of 1.125° (about 125 km) and a vertical resolution of 31 levels (Gibson et al., 1999).

The fields from the re-analysis projects, which are used to force the ocean model in this study are the following:

heat fluxes:	net heat flux	W/m^2	total, time dependent fields
	net short wave radiation	W/m^2	annual cycle only
wind stresses:	zonal wind stress	N/m^2	total, time dependent fields
	meridional wind stress	N/m^2	total, time dependent fields

The net heat flux is a composite of all parts of heat fluxes between ocean and atmosphere, i.e. latent heat flux, sensible heat flux, net long wave radiation and net short wave radiation. Only the latter is allowed to penetrate beneath the surface layer.

The fresh water flux is determined indirectly within the ocean model run by restoring to the climatological sea surface salinity (SSS), see chapter 3.1. Furthermore, the sea surface temperature (SST) fields of the re-analysis are used as well, see also chapter 3.1.

The climatological daily annual cycle of the net short wave radiation is computed over the period from 1973-1997 and 1979-1998 for the data sets of NCEP/NCAR and ECMWF respectively and both are smoothed with a 31 day running mean. All fields are interpolated onto the ocean model grid. For the scalar fields (SST and heat fluxes), a bi-linear method was used. For the vector fields, i.e. zonal and meridional wind stresses, a 3rd order Bessel interpolation method was applied to avoid the introduction of artificial wind stress curl.

Chapter 3

Ocean, Atmosphere and Coupled Model

The ENSO phenomenon results from a coupled interaction between ocean and atmosphere. Hence, to study ENSO and its predictability a coupled system consisting of both an ocean and an atmosphere model is required. Furthermore, the memory of the coupled system is assumed to reside in the ocean subsurface thermal structure according to the "subsurface memory paradigm" (Neelin et al., 1998). Therefore the ocean model chosen for this study is an ocean general circulation model including full dynamics, whereas the atmosphere model chosen is a statistical atmosphere model which responds passively to the variations in the SST.

3.1 The E-HOPE Ocean Model

The ocean model used is the Hamburg Ocean Primitive Equation model (HOPE - Wolff et al. (1997)). It is based on the nonlinear balance equations for momentum ("Navier-Stokes" equations), the continuity equation for an incompressible fluid and conservation equations for temperature and salinity. The hydrostatic and Boussinesq approximations are applied. The prognostic variables are temperature, salinity, horizontal velocities and sea surface elevation.

The horizontal momentum balance equations are:

$$\frac{d\mathbf{v}}{dt} - f(\mathbf{k} \times \mathbf{v}) = -\frac{1}{\rho_0}[\nabla_H(p + \rho_0 g\zeta)] + \nabla_H A_H \nabla_H \cdot \mathbf{v} + \frac{\partial}{\partial z}(A_V \frac{\partial \mathbf{v}}{\partial z}) \tag{3.1}$$

where $\mathbf{v} = (u, v)$ is the horizontal velocity vector, f the Coriolis parameter, $\mathbf{k}$ an upward vertical unit vector, ρ_0 a reference density, ∇_H the horizontal gradient operator, $p = g\int_0^h \rho dz$ the internal pressure, ζ the sea level, A_H the horizontal and A_V the vertical turbulent viscosity coefficients. Using the hydrostatic approximation the internal pressure is computed from

$$\frac{\partial p}{\partial z} = -g\rho \tag{3.2}$$

The vertical velocity is computed diagnostically from the incompressibility condition:

$$\frac{\partial w}{\partial z} = -\nabla \cdot \mathbf{v} \tag{3.3}$$

The surface elevation is computed from the linearised kinematic boundary condition:

$$\frac{\partial \zeta}{\partial t} = w(z = 0) = \nabla \cdot \int_{-H}^{0} \mathbf{v} dz \tag{3.4}$$

where $H(x, y)$ is the water depth. The density is computed with the equation of state, a nonlinear polynomial depending on salinity, temperature and pressure (UNESCO, 1983). In the case of static instabilities convective adjustment is applied, i.e. each pair of vertically adjacent unstably stratified layers is vertically mixed with heat and salt being conserved. Salinity and temperature are determined from the prognostic equations

$$\frac{dT}{dt} = \frac{\partial}{\partial z}(D_V \frac{\partial T}{\partial z}) + D_H \nabla_H^2(T) \tag{3.5}$$

$$\frac{dS}{dt} = \frac{\partial}{\partial z}(D_V \frac{\partial S}{\partial z}) + D_H \nabla_H^2(S) \tag{3.6}$$

where D_H and D_V are the horizontal and vertical eddy diffusivity coefficients. Bottom friction is computed applying a Newtonian friction law. No-slip boundary conditions are

used at lateral boundaries. The model setup used here has a domain limited to the Pacific Ocean (120°E-70°W, 55°S-67°N) and a realistic bottom topography. The model has a 2.8125° resolution with an equatorial refinement, i.e. the meridional resolution increases gradually to 0.5° within the region 10°N to 10°S. Vertically, there are 20 irregularly spaced levels, with ten levels within the upper 300m. The numerical scheme is computed on the Arakawa E-grid (Arakawa and Lamb, 1977). Therefore this model version is called the E-HOPE version of the HOPE model. The time step is two hours. An idealised 360-day year subdivided into 12 equal-length months of 30 days is used. There is no diurnal cycle in the forcing fields. The model is forced by the surface wind stresses specified in chapter 2.3:

$$\tau = \rho_0 A_V \frac{\partial \mathbf{v}}{\partial z} \tag{3.7}$$

Surface heat flux forcing is also imposed, whereas no explicit fresh water flux forcing is provided. Although salinity may play a role for ENSO dynamics (Vialard and Delecluse, 1998) and therefore also precipitation and evaporation, this aspect is disregarded here as this work focuses on the improvement of the thermal fields. Additionally, the true magnitude of precipitation over the oceans is a major uncertainty and re-analyses appear to have large biases (WCRP, 2000). Instead of direct fresh water forcing a Newtonian relaxation is employed to restore the surface salinity within the whole domain to the monthly climatology of Levitus et al. (1994) using a time constant of 40 days. The according fresh water flux can thus be deduced. Furthermore, a Newtonian relaxation to daily SST is applied with a relaxation constant of $40 W/m^2 K$. The SSTs are also provided by the re-analyses, described in chapter 2.3.

3.2 The Statistical Atmosphere Model

The atmosphere model which is used in this study is a statistical model, based on anomalies. The idea behind this model is that in the coupled system, atmospheric wind stress and net heat flux depend only on sea surface temperature (SST). Thus the atmospheric state is regarded as a "slave" which responds passively to the SST anomalies and which has no internal dynamics.

The statistical model is derived from 42 years (1949-1990) of monthly SST, surface wind stress and net heat flux anomalies. These data were obtained from the "ECHAM-3" general circulation atmosphere model (Roeckner et al., 1992; DKRZ, 1992) forced by data from the Global sea-Ice and Sea Surface Temperatures (GISST, Parker et al. (1995)) dataset. The latter are denoted as $T_{obs}(x,t)$ in the following.

The construction of the statistical atmosphere model was done similar to the one described in Barnett et al. (1993): wind stress anomalies and surface heat flux anomalies were combined in one dataset as atmospheric flux anomalies $\mathcal{F}_{echam}(x,t)$. These atmospheric flux anomalies and the SSTA $T_{obs}(x,t)$ were expressed in terms of empirical orthogonal functions (EOFs, Lorenz (1956)) (the anomalies in this section are computed relative to the annual cycle):

$$T_{obs}(x,t) = \sum_n \alpha_n(t) e_n(x) \tag{3.8}$$

$$\mathcal{F}_{echam}(x,t) = \sum_m \beta_m(t) f_m(x) \tag{3.9}$$

where x denotes space and t time. α and β are the EOF time series ("principal components") and e and f are the spatial EOF patterns ("eigenvectors").

The linear regression between the principal components of the two datasets yields a matrix of regression coefficients C:

$$C_{mn} = \frac{\langle \alpha_n \beta_m \rangle}{\langle \alpha_n^2 \rangle} \tag{3.10}$$

where angle brackets ("$\langle\rangle$") indicate time averages. The linear regressions are computed with the SSTs leading wind stress and surface heat flux anomalies by one month as the atmospheric forcing is always computed for the coming month's time steps. The atmospheric flux anomalies were thus estimated from the relations

$$\alpha_n(t) = \sum_x T_{obs}(x,t) e_n(x) \tag{3.11}$$

and

$$\widehat{\beta}_m(t) = \sum_n C_{mn}\alpha_n(t) \tag{3.12}$$

which finally yields

$$\widehat{\mathcal{F}}(x,t) = \sum_m \hat{\beta}_m(t) f_m(x) \tag{3.13}$$

where a hat ("^") denotes a statistically estimated value.

To capture the modes of interannual variability well, the first 10 EOFs of the anomalies are retained for the linear regression. Thus n and m are both taken to be 10. These EOFs explain 63% of the field variance in case of the SSTA and 49% in case of the combined atmospheric flux anomalies.

3.3 The Hybrid Coupled Model

For the forecasts performed in this study the HOPE ocean model (3.1) is coupled to the statistical atmosphere model described in the previous section. Combining such a sophisticated ocean general circulation model (OGCM), as the HOPE ocean model, with a simpler atmospheric model is generally referred to as building a hybrid coupled model (HCM).

In case of the HCM used in this study, the statistical atmosphere model is built using observed SSTA. Since the SSTA simulated by the ocean model show systematic differences to those observed, an interface is included which relates the ocean model SSTA to the observed SSTA and allows to calculate "observed" SSTA from given simulated SSTA. The interface is constructed in the same way as the statistical atmosphere model: both SSTA fields, simulations ($T_{sim}(x,t)$) and observations (T_{obs}), were expressed in terms of EOFs (from equation 3.8):

$$T_{sim}(x,t) = \sum_l \gamma_l(t) g_l(x) \tag{3.14}$$

The linear regression between their temporal coefficients yields the regression matrix C:

$$C_{nl} = \frac{\langle \gamma_l \alpha_n \rangle}{\langle \gamma_l^2 \rangle} \tag{3.15}$$

and thus allows to estimate "observed" SSTA fields from the ocean model SSTA:

$$\gamma_l(t) = \sum_x T_{sim}(x,t) g_l(x) \tag{3.16}$$

and

$$\widehat{\alpha}_n(t) = \sum_l C_{nl} \gamma_l(t) \tag{3.17}$$

The corrected SSTA are than given by:

$$\widehat{T}_{obs}(x,t) = \sum_n \widehat{\alpha}_n(t) e_n(x) \tag{3.18}$$

As in the case of the statistical atmosphere, the first 10 EOFs are retained for the linear regression here as well. In the coupled case, the estimated time coefficient $\widehat{\alpha}_n(t)$ from (3.17) can be used directly in (3.11) to compute the atmospheric fluxes.

To avoid a slow model drift a weak relaxation is introduced:

$$\widehat{Q}_{cor}(x,t) = \lambda(T_{sim}(x,t) - \widehat{T}_{obs}(x,t)) \tag{3.19}$$

with the relaxation constant $\lambda = -10\,W/m^2K$.

In coupled mode the SSTA of the ocean model are passed to the statistical atmosphere once every month. The SSTA are used with (3.11) and (3.17) to estimate an according time coefficient $\widehat{\beta}$ from (3.12) and, hence, the atmospheric flux anomalies $\widehat{\mathcal{F}}(x,t)$ (3.13) for the following month. The sum of these atmospheric flux anomalies and their appropriate climatological values together with the according heat flux correction (3.19) compose the total forcing of the ocean model. These monthly computed fields are interpolated linearly

in time. As SST variations are slowly evolving, daily coupling with a daily computation of the fluxes instead of monthly is not expected to change the results significantly.

The coupled model shows ENSO-like behaviour with fairly regular oscillations of the Niño3 SSTA with periods of around 2.5 years (Eckert and Latif, 1997). The spatial structure and amplitude of the SSTA are comparable to those obtained with prescribed forcing (van Oldenborgh et al., 1999).

Chapter 4

Applied Methods of Assimilation

To compare their influence on the ENSO forecast skill three different types of data are assimilated into an OGCM. These data types are sea levels measured by the TOPEX/POSEIDON satellite, sea surface temperatures (SST) from NCEP/NCAR re-analysis and in situ temperature measurements from the TAO/TRITON array. The data are introduced in chapter 2. Each of these data types requires special adjustments of the assimilation scheme due to different collocation of their observational sites. That is, it has to be regarded whether the data are surface or subsurface data and whether they are spaced on fine or coarse grids. Therefore the assimilation scheme is split up into two parts, a projection scheme to bring the surface information (SST, SSH) also into deeper layers, and an insertion scheme to blend model data and observational data. The insertion scheme is adjusted individually for the different kinds of observational grids. The general insertion scheme of the data into the model is described first. Each of the three data dependent assimilation approaches is described thereafter, including the appropriate adjustment of the insertion scheme.

4.1 The Insertion Scheme

The insertion scheme describes how the model data are combined with the observational data. In this study, the data are inserted sequentially, correcting the model fields at every time step. The information of one measurement is spread over the model area and time

with characteristic time and length scales.

This approach is similar to the method of successive correction (Daley, 1991; Fischer et al., 1997) which itself is leading back to the meteorological spatial analysis of Bergthorsson and Doos (1955). It allows a smoother insertion of the observations compared to nudging, which pulls the model towards the data just at measurement points and times. In contrast to other sequential assimilation schemes like statistical interpolation (often also called optimal interpolation or Gauss-Markov method) and Kalman filter methods, the weighting of the data is estimated just once from observed correlation scales instead of being statistically derived at every ocean update for every single grid point.

The method of successive correction also takes into account expected error variances of model and observed fields. In this study the errors of the model field are not known, therefore neither the errors of the model field nor those of the observations are taken into account here. Within one assimilation step the model (background) field $\mathcal{X}_m$ is updated at each grid point i to obtain the analysed field $\mathcal{X}_a$ as follows:

$$\mathcal{X}_a = \mathcal{X}_m - F \sum_k W_{ik} \left(\mathcal{X}_m - \mathcal{X}_{obs}(k)\right) W_t \tag{4.1}$$

with $\mathcal{X}_{obs}$ being the observations, k the measurement points and F a relaxation constant. The spatial and temporal weights are defined as:

$$W_{ik} = exp\left(-\frac{(x_i - x_k)^2}{L_x^2} - \frac{(y_i - y_k)^2}{L_y^2}\right) \tag{4.2}$$

and

$$W_t = \begin{cases} 1 - \frac{|t-t_0|}{\delta t}, & |t - t_0| < \delta t \\ 0, & |t - t_0| \geq \delta t \end{cases} \tag{4.3}$$

The differences $(\mathcal{X}_m - \mathcal{X}_{obs}(k))$ are weighted with the spatial correlation weight W_{ik}. It is assumed that the correlation scales are only a function of the distance between points and not of their absolute position. A Gaussian shape function has been chosen with different characteristic e-folding scales L_x and L_y, in the zonal and meridional direction (4.2). Further, every difference between background and observed value is multiplied by

a temporal weight W_t, which changes linearly from zero to one and back to zero, as the difference between model time and observational time goes from $t_0 - \delta t$ to zero and to $t_0 + \delta t$ (4.3).

Finally, the obtained correction is multiplied by a constant factor F, here chosen to be $F = 0.1$. This factor determines how fast the data are inserted into the model.

4.2 The Univariate Assimilation Method

The first assimilation approach described here is the univariate method, assimilating sea level data only. Sea surface heights contain information about the vertical density structure of the water column underneath. In this study it is investigated if this information, given by the Topex/Poseidon (T/P) data, can be used to improve the ocean initial state and thus also El Niño forecasts. As the model carries sea surface elevation as a prognostic variable, it would be possible to assimilate sea level data directly into the ocean model. However, this would just excite short, fast gravity waves (Fischer, 1996), the information would be lost within a few time steps and the density structure of the ocean interior would not be improved. Therefore, the surface data are projected onto subsurface fields and these are then inserted into the model.

4.2.1 Projection

The idea is to compute a regression between sea level and the density of the water column underneath at each horizontal grid point. Thus, the observed sea level can be projected via this statistical relationship onto subsurface fields. This assumes a linear relation between small changes in sea level and a corresponding change in the vertical mass structure. This idea originates from Fischer and Latif (1995) and Mellor and Ezer (1991). The ocean model run, from which the statistics are deduced, is a run of the E-HOPE ocean model (described in chapter 3.1) over 45 years from 1945 to 1989 forced by atmospheric fields of ECHAM climatologies plus COADS (da Silva et al., 1994) anomalies. The advantage of taking model data for the calculation of the statistical relationship is that the projected data, which are to be inserted into the model, have structures which are consistent with the

mean state of the ocean model, taking into account that the anomaly assimilation scheme does not correct for errors in the mean state. Furthermore, an observational dataset, with a sufficient temporal and spatial resolution for these statistical derivations, i.e. with a resolution comparable to that of the ocean model does not exist.

The regressions could theoretically be calculated between the sea level and all grid points at every level underneath (as it has been done in Mellor and Ezer (1991)). This, however, may produce noise which would be fitted to the model. Therefore, in this study, as it has also been done in Fischer et al. (1997), the sea level is regressed onto the leading vertical modes of the system, expressed by the empirical orthogonal functions (EOFs, Lorenz (1956)) at each water column of the model grid.

As density is a function of temperature, salinity and pressure, tests are performed to relate the sea level to EOFs calculated from both, temperature only and temperature plus salinity profiles.

The statistical relations are computed between anomalies relative to the climatological annual cycle of the 45 year ocean model run as follows. For each vertical column the temperature anomalies (T') are expressed in terms of EOFs:

$$T'(z) = \sum_n \alpha_n(t) e_n(z) \tag{4.4}$$

with $z = 1, 20$ being the ocean model levels and $n \in 1, 2, \ldots, 20$. The principal components (α_n) of these EOFs are regressed onto the sea level anomaly (SLA, ζ'):

$$\alpha_n(t) = r_n \zeta'(t) \tag{4.5}$$

with the regression coefficients

$$r_n = \frac{S_{\zeta'\alpha_n}}{S^2_{\zeta'}} \tag{4.6}$$

where $S_{\zeta'\alpha_n}$ denotes the covariance between SLA (ζ') and the principal component (α_n). $S^2_{\zeta'}$ denotes the variance of the SLA. For the combined EOFs normalised time series of the

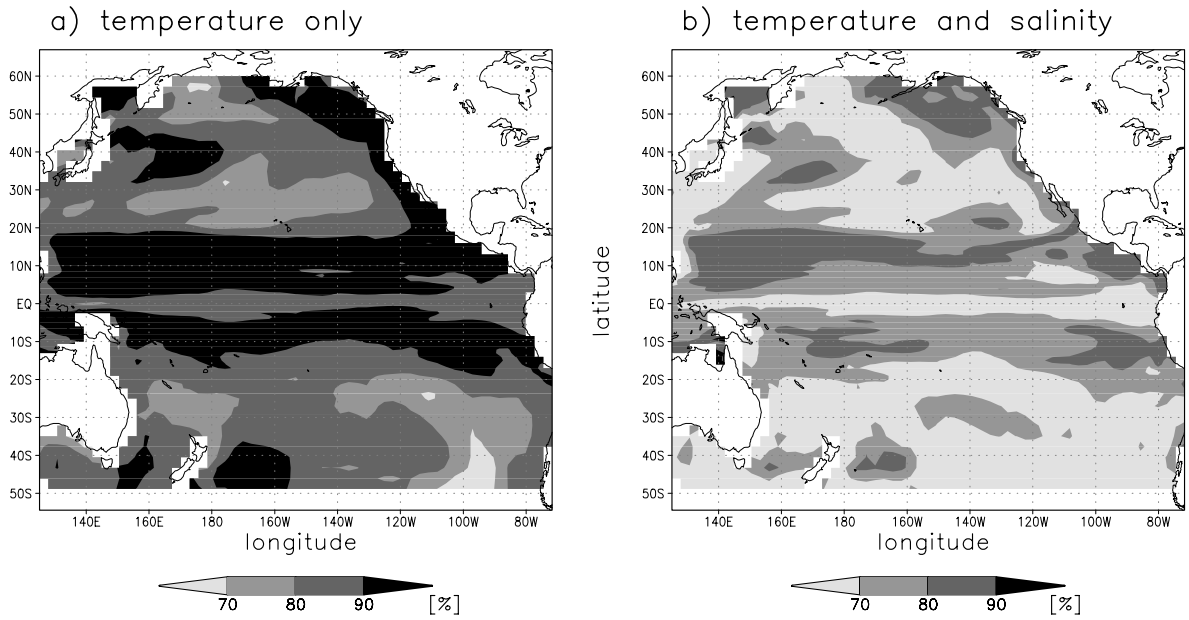

Figure 4.1: *Variances explained by the first two vertical EOFs for each water column of: a) temperature only and b) temperature and salinity combined.*

vertical profiles of temperature anomalies ($T'_{norm}(z)$) and salinity anomalies ($S'_{norm}(z)$) are computed:

$$F'(z) = \sum_n \alpha_n(t) e_n(z) \qquad \text{with} \quad z = 1, 40 \tag{4.7}$$

and

$$\begin{aligned} F'(z) &= T'_{norm}(z_1) \quad : \quad z = 1, 20 \quad \text{and} \quad z_1 = 1, 20 \\ F'(z) &= S'_{norm}(z_2) \quad : \quad z = 21, 40 \quad \text{and} \quad z_2 = 1, 20 \end{aligned} \tag{4.8}$$

The first two vertical EOFs of just temperature explain more than 80% of the total variance of temperature everywhere in the tropical Pacific between 15°N and 15°S, and in large regions even more than 90% (see figure 4.1). In the same region, the first two vertical EOFs of a combined EOF analysis of temperature and salinity together explain in some regions even less than 70% of their total variance, especially at the equator. Thus the variability of temperature has more pronounced leading modes of variability than the variability of temperature and salinity together. Further, the vertical EOF modes of temperature also correlate better with sea level than the combined modes of temperature and salinity

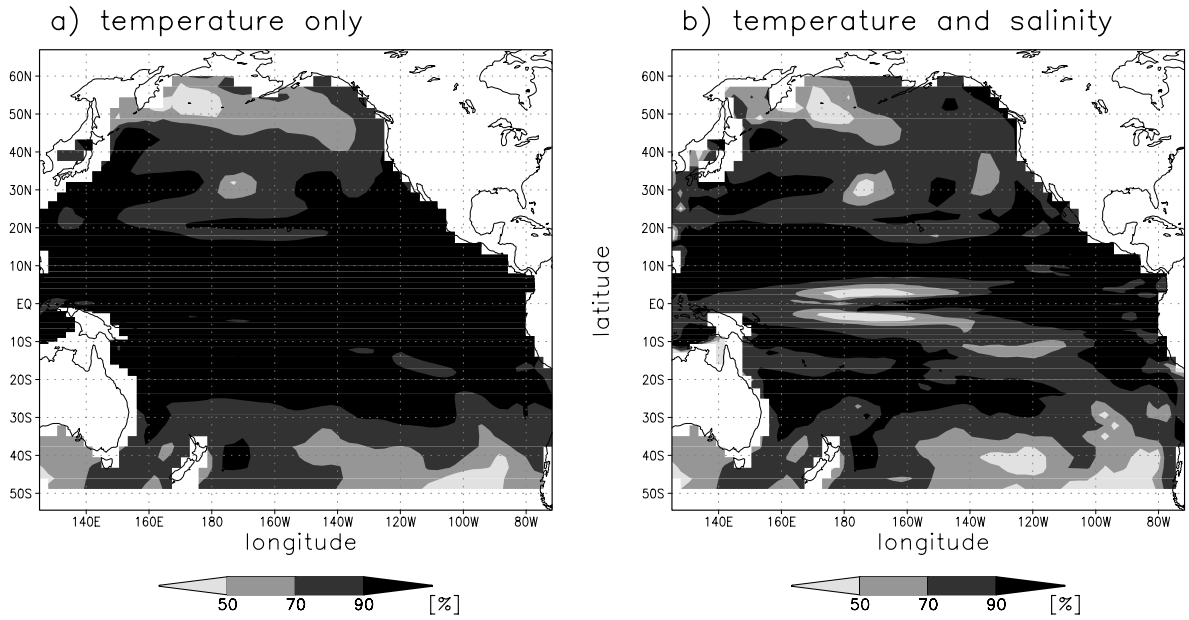

Figure 4.2: *Variances of SLA explained by the first two vertical EOFs for each water column of: a) temperature only and b) temperature and salinity combined.*

together (not shown). The two vertical EOFs of temperature only explain more variance of the sea level variability than the first two combined EOFs of temperature and salinity (figure 4.2). As the first two vertical EOFs of temperature explain already more than 80% (and in some regions more than 90%) of the total thermal variability in the tropical Pacific (figure 4.1a) and in most parts of the tropical Pacific even more than 90% of the sea level variability, these two were taken for the reconstruction of the anomalous temperature field from sea level.

At the equator, these two EOFs can be identified with the first and second baroclinic modes. The first baroclinic mode explains most of the variability at the equator, except near the date line and west of it, where the second baroclinic mode becomes the leading EOF (figure 4.3). The second EOF shows complementary structures to the first EOF with the second baroclinic mode in the eastern and central equatorial Pacific and a kind of first baroclinic mode at the date line and west of it (figure 4.4).

This distinction is reflected by the correlation with the sea level, shown in the top panels of figures 4.3 and 4.4. The first baroclinic modes and in particular those with the most pronounced loadings go along with the highest thermal expansions and therefore correlate

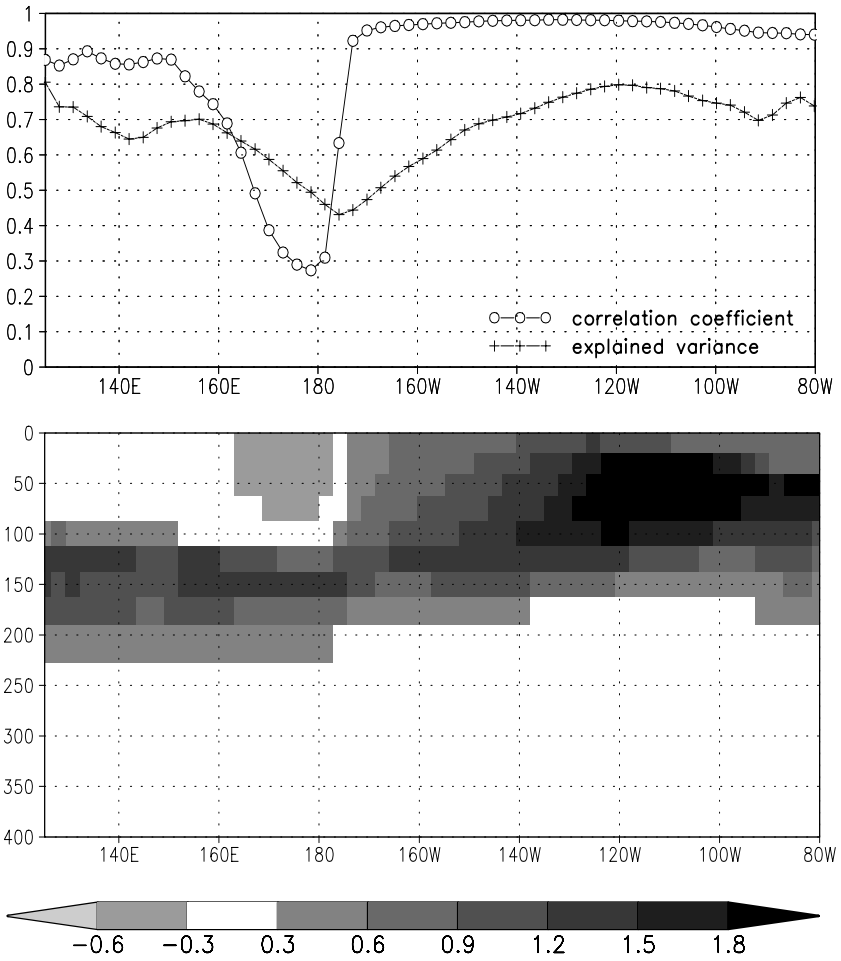

Figure 4.3: *The first (highest energetic) vertical EOFs of temperature for the profiles of each point at the equator are shown in the lower panel. The corresponding explained variances of the vertical EOFs and the correlation coefficients of their PCs and the sea level are shown in the upper panel.*

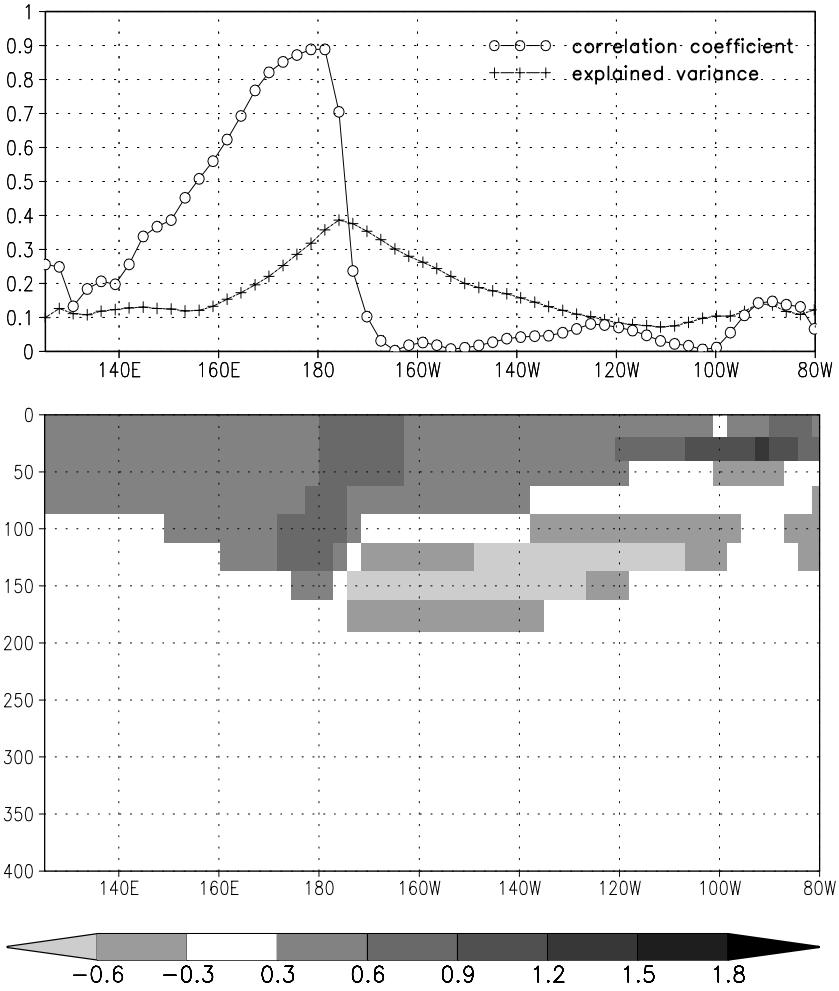

Figure 4.4: *The second most energetic vertical EOFs of temperature for the profiles of each point at the equator are shown in the lower panel. The corresponding explained variances of the vertical EOFs and the correlation coefficients of their PCs and the sea level are shown in the upper panel.*

best with the sea level, with correlation coefficients of above 0.95. On the contrary, the loadings with reverse signs in one water column of the second baroclinic mode tend to cancel each other in their influence on the sea level, thus the corresponding correlation coefficients range from nearly zero (i.e. values of 0.01) to values of 0.3, near the dateline.

4.2.2 Reconstruction

The two leading vertical EOFs (equation 4.4) and their relation to the SLA (equation 4.6) are used to reconstruct the 3-dimensional fields of temperature anomaly $T'_{re}(z)$ with observed SLA (ζ'):

$$T'_{re}(z) = \sum_i \zeta' r_i e_i(z) \qquad \text{with } i = 1, 2 \tag{4.9}$$

The temporal resolution of SLA is 10 days (Chapter 2.1). For equation 4.9 the SLA are interpolated linearly (following equation 4.3) onto the ocean model time step. As the ocean model has an idealised year with 360 days, this is done with one ocean model day representing $\frac{365.25}{360}$ real days.

4.2.3 Insertion

All mapped T/P SLA data points are available simultaneously. Therefore the above mentioned temporal interpolation is independent of any specific observational point and can be calculated after the spatial interpolation, directly together with the insertion. This simplifies insertion equation 4.1 for the case of the T/P data. Furthermore, the spatial interpolation can also be simplified. The grid of the T/P data is, at least zonally, more than one order of magnitude finer than the ocean model grid and the data are continuously available without any big gaps. Thus, for every T/P data time step, the T/P data can be interpolated with a box averaging method onto all ocean model surface grid points and equation 4.1 simplifies to:

$$T_a = T_m - F\,(T_m - T_{obs}) \tag{4.10}$$

with

$$T_{obs} = T_{clim} + T'_{re}(z) \tag{4.11}$$

and T_{clim} being the climatological annual cycle of temperatures calculated from the 45 years of ocean model run, described in section 4.2.1. The correction of the model solution is applied every ocean model time step to ensure that the corrections remain small, so that the internal dynamical balance of the model is disturbed only slightly. Thus the generation of high-frequency gravity waves can mainly be avoided. After each correction step a convective adjustment routine is applied to remove unstable stratification.

4.3 The Bivariate Assimilation Method

Before ENSO changes its state, precursors often signalise potentially emerging ENSO extremes up to half a year in advance. These precursors feature subsurface thermal anomalies in the central equatorial Pacific. Often, these subsurface temperature anomalies have reverse sign of those at the surface. TA in the western and central tropical Pacific, hidden from the surface, can lead to fast changes of the state of ENSO. Sea surface temperature anomalies (SSTA) in turn drive the atmospheric response. For successful forecasts, it is believed that it is necessary to capture both temperature anomalies, at and below the surface (Fischer, 2000).

Such a situation occurred for example in December 1997, displayed in figure 4.5. Warm El Niño conditions were found at the surface in the eastern and central equatorial Pacific. Cold TA were observed in the subsurface western-central equatorial Pacific, indicating the forthcoming La Niña event of 1998. Thus in the central tropical Pacific TA with reverse signs occurred in one water column in December 1997. These two signals cancel each other in their influence on the sea level. In terms of vertical EOFs, the TA in this region are consistent with those of the second baroclinic mode. Due to the cancelling effect this second baroclinic mode correlates only weakly with sea level (see also section 4.2.1). For this reason univariate projections of SLA onto TA do not work well in situations with stratified TA like in December 1997 (figure 4.6). As can be seen from the reconstruction,

zero temperature anomalies occur when the SLA vanish (near 160°W). Thus, additional information of another variable is necessary to improve the reconstruction of temperature fields in such situations.

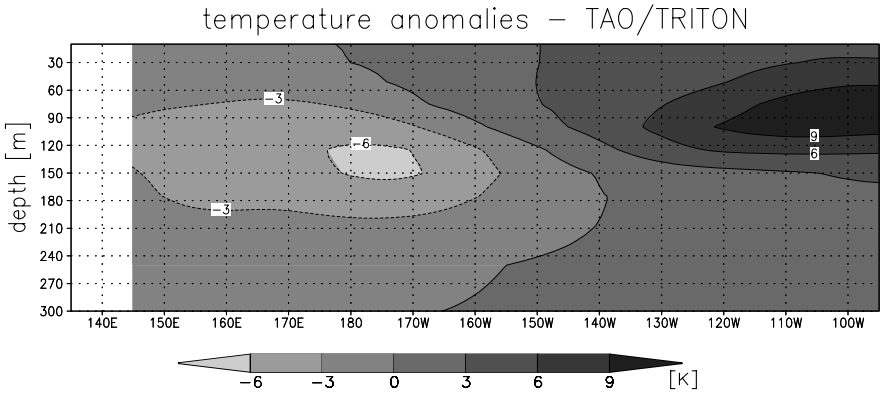

Figure 4.5: *Monthly mean equatorial temperature anomalies (relative to the annual cycle over 1993 to 1996) in December 1997 measured by the TAO/TRITON buoy array.*

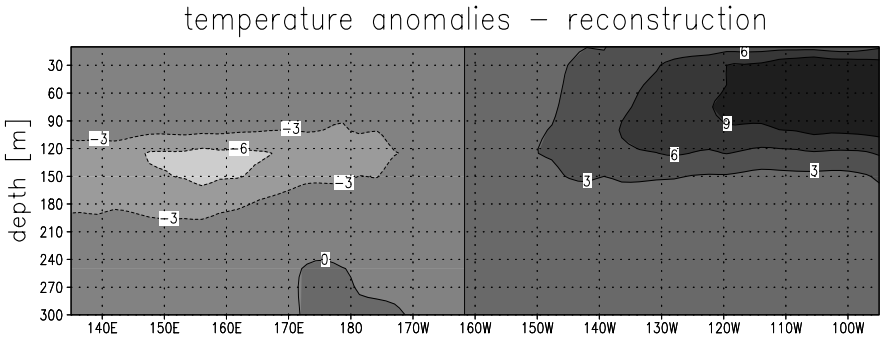

Figure 4.6: *Monthly mean equatorial temperature anomalies [K] (relative to the annual cycle over 1993 to 1996) in December 1997 as reconstructed by the univariate assimilation scheme, shading like in figure 4.5.*

SSTA is chosen as a second variable, as it includes the additionally wanted surface information. The multivariate assimilation scheme, including both, the SLA and the SSTA is referred to as the bivariate assimilation in the following. The derivation of this bivariate assimilation is analogous to the univariate assimilation, described in the previous section. The same EOFs and PCs of TA are used, but in this case the PCs ($\alpha_n(t)$, see equation 4.5) are regressed onto both, SLA (ζ') and SSTA (SST'):

$$\alpha_n(t) = r_{nm} \begin{bmatrix} \zeta'(t) \\ SST'(t) \end{bmatrix} \tag{4.12}$$

With the definition

$$\begin{bmatrix} X \\ Y \end{bmatrix} := \begin{bmatrix} \zeta'(t) \\ SST'(t) \end{bmatrix} \tag{4.13}$$

the regression coefficients become

$$r_{nm} = \alpha_n(t) \begin{bmatrix} X \\ Y \end{bmatrix}^T \left(\begin{bmatrix} X \\ Y \end{bmatrix} \begin{bmatrix} X \\ Y \end{bmatrix}^T \right)^{-1} \tag{4.14}$$

where " ^{T} " denotes the transposed and " $^{-1}$ " the inverted matrix. With $Z := \alpha_n(t)$ the regression coefficients are calculated as follows

$$r_{n1} = \frac{S_{ZY}S_{YX} - S_{ZX}S_{YY}}{S_{YX}^2 - S_{XX}S_{YY}} \tag{4.15}$$

$$r_{n2} = \frac{S_{ZX}S_{YX} - S_{ZY}S_{XX}}{S_{YX}^2 - S_{XX}S_{YY}} \tag{4.16}$$

where S_{XX} and S_{YY} denote the variances of SLA and SSTA, respectively. S_{ZX}, S_{ZY} and S_{YX} denote the according covariances between PCs and SLA, PC and SSTA and between SSTA and SLA, respectively.

The variances of sea level and sea surface temperature variability which are explained by the leading two vertical temperature EOFs are displayed in figure 4.7. Over most of the tropical Pacific the explained variances of both SLA and SSTA variability exceed 90%. The correlation coefficients, regression coefficients and the explained variances along the equator are displayed in figure 4.8 for the regression with the first EOF and in figure 4.9 for the regression with the second EOF. This shows the high connection of the SSTA with the first EOF near the dateline and explains the high correlation coefficient there, which is in marked contrast to the univariate case.

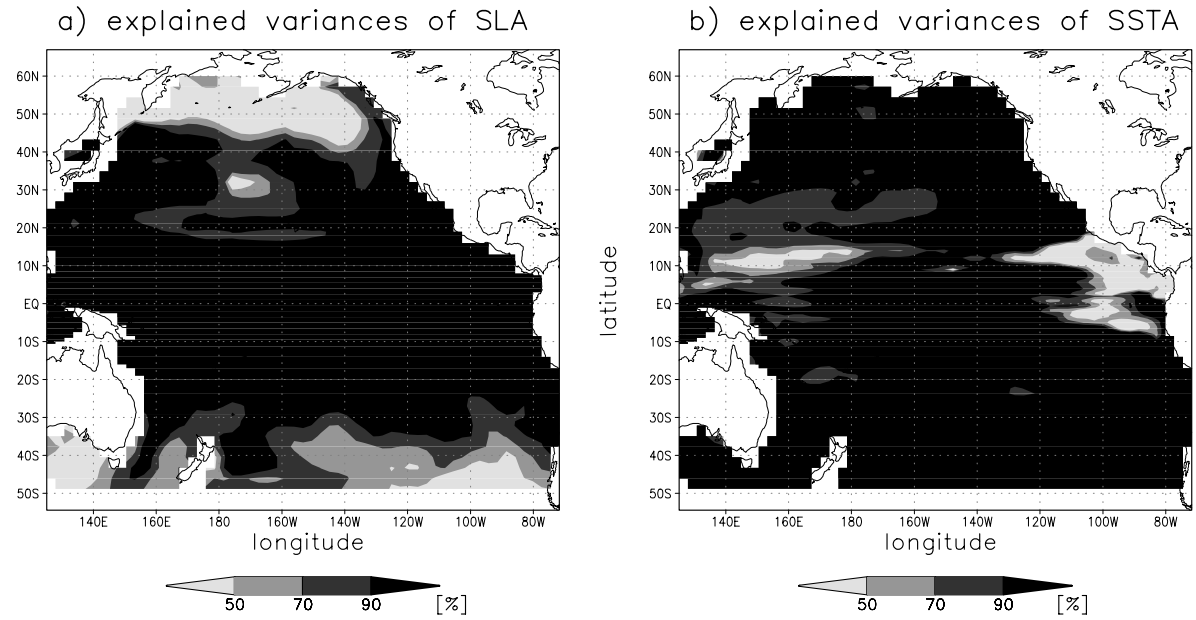

Figure 4.7: *Variances of a) SLA and b) SSTA variability explained with the bivariate method by the first two vertical temperature EOFs for each water column.*

The reconstruction of TA is calculated as follows:

$$T'_{re}(z) = \sum_i \zeta' r_{i1} e_i(z) + SST' r_{i2} e_i(z) \qquad \text{with } i = 1, 2 \tag{4.17}$$

The insertion of the reconstructed TA ($T'_{re}(z)$) is done in the same way as in the univariate case.

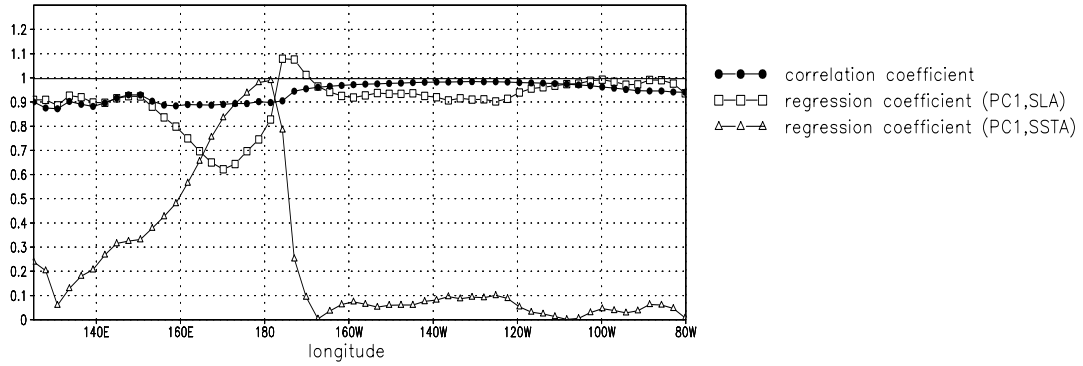

Figure 4.8: *Correlation and regression coefficients at the equator of the bivariate regression between the PCs of the first vertical EOFs of temperature (see figure 4.3) as the predictands and SLA and SSTA as the predictors and the according regression coefficients with SLA, SSTA respectively.*

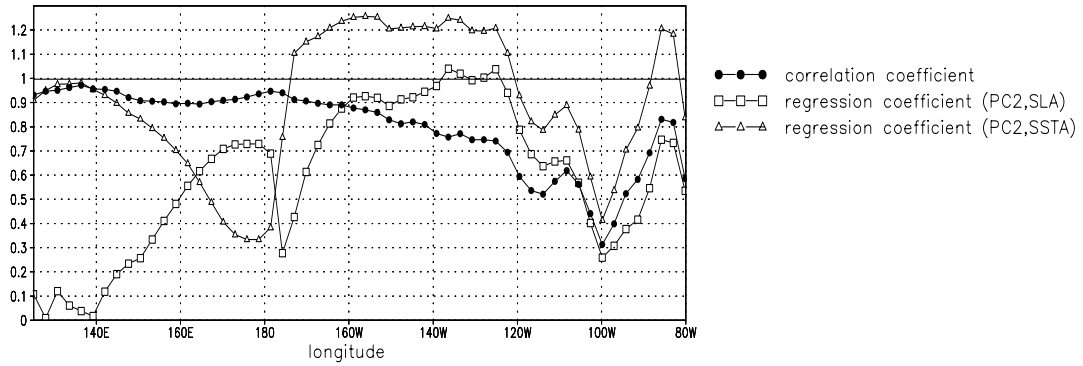

Figure 4.9: *Correlation and regression coefficients at the equator of the bivariate regression between the PCs of the second vertical EOFs of temperature (see figure 4.4) as the predictands and SLA and SSTA as the predictors and the according regression coefficients with SLA, SSTA respectively.*

4.4 Assimilation of TAO/TRITON Data

Subsurface temperatures of the TAO/TRITON buoy array (described in detail in chapter 2.2) only need insertion into the ocean model. Their vertical interpolation has been carried out independently and is described in chapter 2.2.

Decorrelation scales for the insertion (equations 4.1 and 4.2) have to be chosen. Kessler et al. (1996), Sprintall and Meyers (1991) and Meyers et al. (1991) estimated decorrelation scales of 3° meridionally and $12° - 15°$ zonally for monthly data. As daily data are used here and relatively fast propagating waves, like Kelvin waves, should be resolved, smaller scales are chosen in this study: 100 km meridionally (L_y, $\widehat{\approx}1°$ latitude) and 1000 km zonally (L_x, $\widehat{\approx}9°$ longitude). The daily subsurface temperature data are interpolated linearly onto each ocean model time step, following equation 4.3.

As many stations of the buoy array were not measuring continuously during the period 1993 to 1996, no reliable climatological annual cycle and thus no according temperature anomalies can be estimated. Thus, in contrast to the sea level data, full data of the TAO/TRITON subsurface temperatures are assimilated.

Therefore the insertion equation 4.1 becomes for TAO/TRITON temperature measurements T_{obs}:

$$T_a = T_m - F\, W_t \sum_k W_{ik}\, (T_m - T_{obs}(k)) \tag{4.18}$$

with k denoting every horizontal measurement point with an according weight W_{ik} larger than 0.05. This equation is evaluated at every ocean model time step.

Chapter 5

Results of Topex/Poseidon Data Assimilation

Three experiments have been performed to evaluate the impact of Topex/Poseidon (T/P) data assimilation, one without any assimilation (Co-EC), one with assimilation of T/P sea level anomalies (As-TP-EC) and the third with assimilation of TAO/TRITON in situ measured temperatures (As-TAO-EC). All experiments in this chapter are forced by ECMWF (re-)analysis data (chapter 2.3) and are analysed for the period from January 1993 until June 2000. Coupled forecast experiments are initialised every 3rd month, using the statistical atmosphere model described in chapter 3.2. An overview of the experiments is given in table 5.1.

The ocean analyses are described in section 5.1, the forecast results in section 5.2 and the

Name	Initialisation	Period	Forcing	Assimilation
Co-EC	Dec'89 of Co-NC[1]	Jan'90-Jun'00	ECMWF	no
As-TP-EC	Dec'92 of Co-EC	Jan'93-Jun'00	ECMWF	T/P
As-TAO-EC	Dec'92 of Co-EC	Jan'93-Jun'00	ECMWF	TAO/TRITON

Table 5.1: *Characteristics of the control experiment (Co-EC), the Topex/Poseidon assimilation experiment (As-TP-EC) and the TAO/TRITON subsurface assimilation experiment (As-TAO-EC).*

[1] NCEP/NCAR-forced run, see table 6.1

seasonality of the forecast results in section 5.3.

5.1 Ocean Analysis

The SLA as well as all other anomalies described in this thesis are computed relative to the annual cycle over the period of 1993 to 1996 unless otherwise noted. This reference period has been chosen to enable a better comparison of the different experiments. The year 1997 itself could not be included, as it would bias the annual cycle too much towards anomalously strong El Niño conditions.

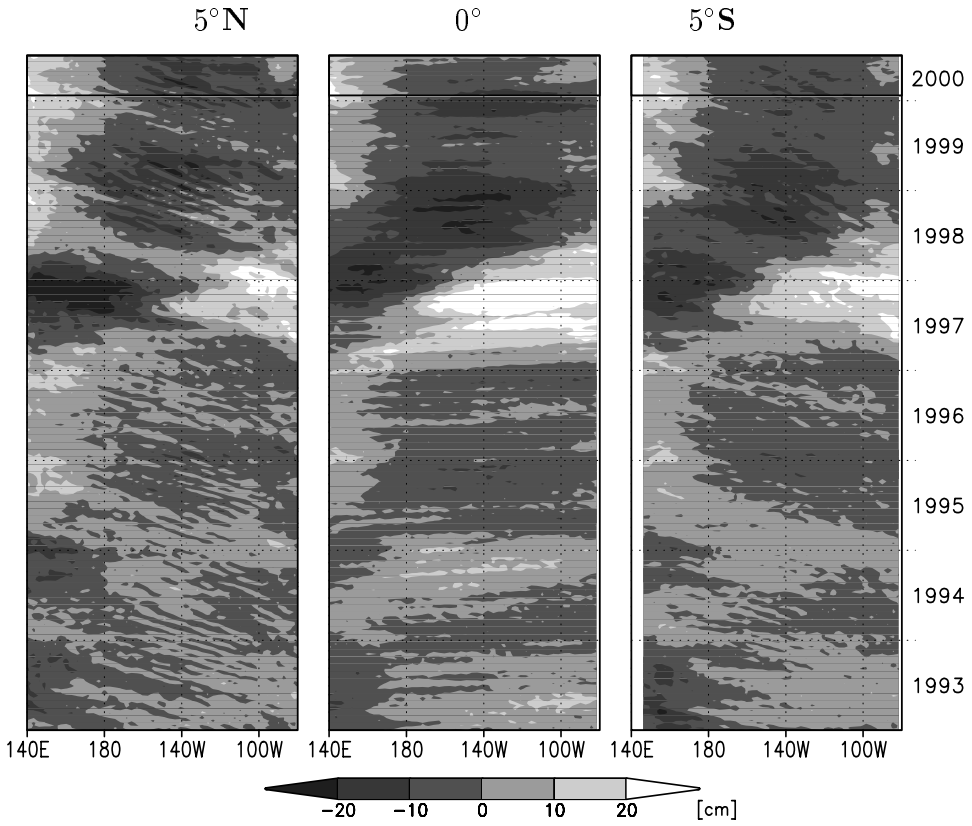

Figure 5.1: *Hovmöller diagrams of T/P SLA along: 5°N (left), the equator (middle) and 5°S (right).*

Observations of SLA at the equator (figure 5.1, middle panel) show positive SLA propagating eastward (2-3 m/s) in early 1993, late 1994 and in 1997. This eastward propagation reflects the memory of the equatorial Pacific. Negative anomalies in the eastern Pacific

show up in early 1994, 1995 and 1996 and even more pronounced in 1998 and 1999. The strongest anomaly is observed in 1997 when El Niño caused an anomalous sea level rise of up to 40 cm in the eastern Pacific. Off the equator (figure 5.1, left and right panel) at 5°N and 5°S, signals propagate mostly westward, consistent with Rossby wave propagation. The propagation speed is about 0.5 m/s on both sides of the equator.

In December 1997, at the peak of the 1997/98 El Niño event (McPhaden, 1999), the highest temperature anomalies (TA) are found in the eastern tropical Pacific at 80 m depth (figure 5.2, upper panel). Simultaneously, negative TA have already developed in the western tropical Pacific and will propagate to the east. This particular month has been chosen to

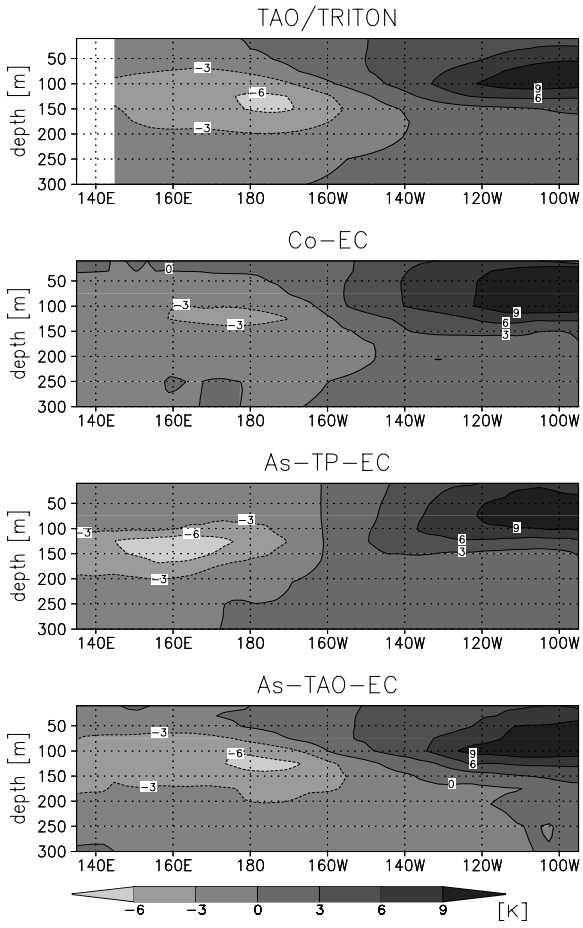

Figure 5.2: *Mean temperature anomalies in December 1997 for the zonal section along the equator: TAO/TRITON observations (upper), control run Co-EC (upper middle), assimilation run As-TP-EC (lower middle), assimilation run As-TAO-EC (lower). Anomalies are relative to the annual cycle.*

investigate if the simulations can capture both, the strong anomalies in the east as well as the developing structures underneath the surface in the western/central part of the equatorial Pacific. The control run, without assimilation, captures the developing TA in the west, but with only half of the observed strength (figure 5.2, upper middle panel). Both assimilation runs help to improve the simulation (figure 5.2, lower middle and lower panels). However, the negative anomalies in As-TP-EC are centered approximately 20° too far to the west. The equatorial TA of the As-TAO-EC run (figure 5.2, lower panel) is similar to the TAO observations (figure 5.2, top panel), as one would expect, since the TAO/TRITON data themselves were assimilated.

To investigate if assimilation of sea level or subsurface temperatures generally reduces errors compared to the control run, Hovmöller diagrams of the SLA difference between T/P data and the three model experiments are shown in figure 5.3.

The experiment Co-EC shows too high SLA in late 1997 (figure 5.3), due to underestimated cold TA in the west and overestimated warm TA in the east (figure 5.2). An overestimation of the strong ENSO signal in the east in late 1997 is also seen in the experiment As-TP-EC, although less pronounced than in the experiment Co-EC. The largest parts of these errors of the simulated SLA in late 1997 of the experiments Co-EC and As-TP-EC can all be explained by errors in the thermal structures of the upper 300m (as displayed in figure 5.2). However, some unexplained errors remain. Experiment As-TAO-EC, for example, shows too low SLA in 1997 but no corresponding error in the thermal structures.

Generally, there are three main sources for errors in the simulation of SLA:

1. errors in wind stress forcing or in ocean model formulation
2. errors due to the fresh water flux (and therefore sea surface salinity)
3. errors due to the assimilation scheme

Errors in the wind stress forcing cannot be distinguished from deficiencies in ocean model parameterisations that deal with the wind stress effects, as there is neither “ground truthing” for wind stress forcing (WCRP, 2000) nor for ocean model formulation. Both of these effects have an influence on the vertical density structure and can thus lead to errors in SLA. If in turn the density field of the ocean model is correct, the sea level may still be wrong

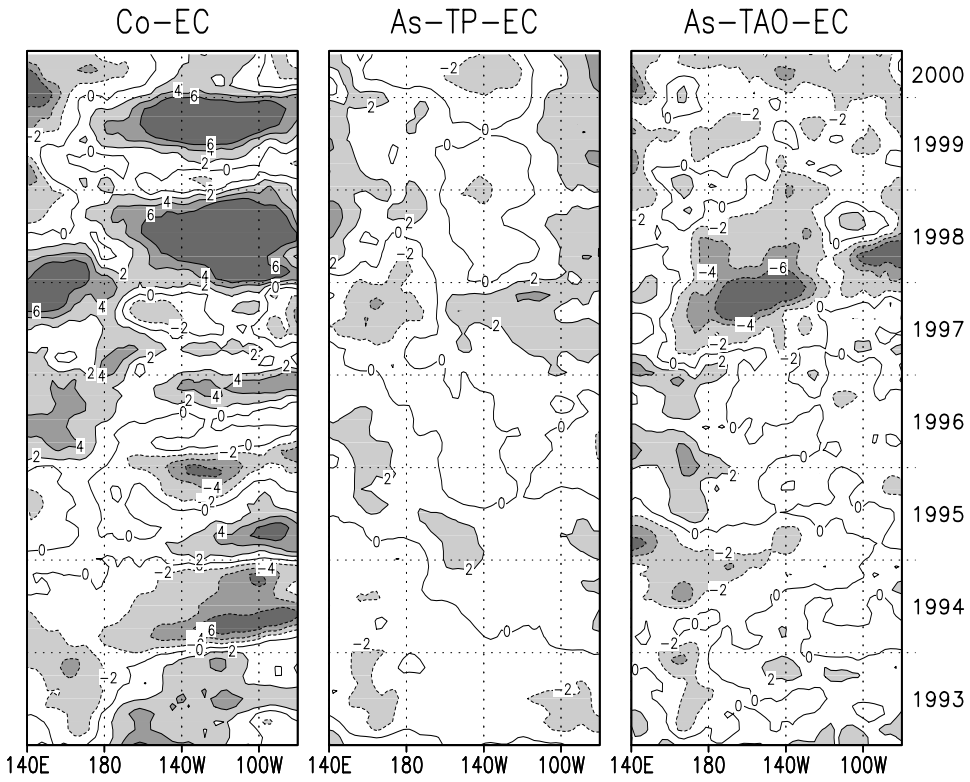

Figure 5.3: *SLA errors [cm] as Hovmöller diagrams along the equator of the three simulations: Co-EC minus T/P observations (left), As-TP-EC minus T/P observations (middle) and As-TAO-EC minus T/P observations (right). The T/P observations have been averaged to monthly data and interpolated onto the ocean model grid. Annual cycles have been removed before computing the differences. For clarity, a 9-point smoothing over space and time has been applied and differences of more than ± 2 cm are shaded.*

due to an incorrect representation of rainfall. Anomalously strong rainfall during El Niño may lead to a fresh water layer at the surface which itself leads to a sea level rise. The model cannot simulate these anomalously high fresh water fluxes, as will be shown below, which causes errors in SLA. Finally, errors may arise also from the assimilation scheme itself, which simplifies the relation between SLA and the density field of the ocean to a linear and thermal driven case.

To evaluate the different error sources, the errors of the mean temperature averaged over the upper 500 m of all three experiments are shown in figure 5.4. The variability of the mean temperature over the whole water column is steered by the thermal variations within the upper 500 meters. This has been checked for all model experiments (not shown).

Considering the upper 500 m only has the additional advantage that it can be compared with observed data from the TAO/TRITON buoy array (chapter 2.2). Anomalies of zonal wind stresses and an estimation of precipitation minus evaporation anomalies (PME) derived from observations are shown in figure 5.5 for comparison with figure 5.3. Both sets of anomalies are calculated relative to their annual cycles, which are estimated from the period 1993 to 1996. As precipitation is not well known over the oceans (WCRP, 2000), two precipitation datasets are shown in figure 5.6 to exemplify the uncertainties in the estimation of rainfall.

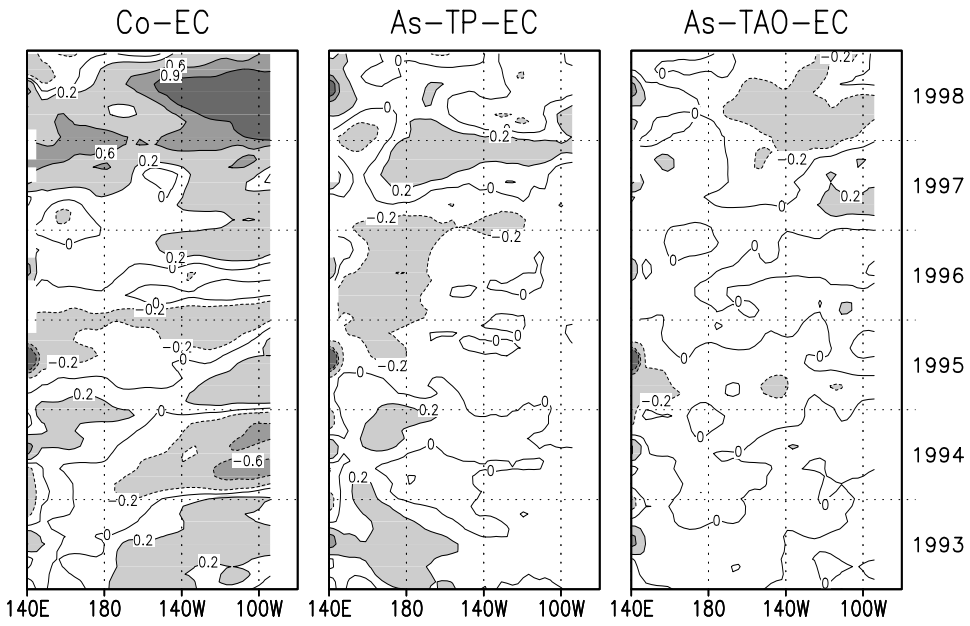

Figure 5.4: *Differences of TA averaged over the upper 500 m [K] as Hovmöller diagrams along the equator: Co-EC minus observations (left), As-TP-EC minus observations (middle) and As-TAO-EC observations (right).*

Errors in SLA of experiment Co-EC (figure 5.3) are relatively large with values over 6 cm. The largest errors in the eastern equatorial Pacific coincide with errors in the thermal field. E.g. in 1994 and at the end of 1995/beginning of 1996 the SLA were too low in Co-EC (figure 5.3) consistent with too low upper ocean temperatures (figure 5.4). The reversed situation appears during 1993, 1995, at the end of 1996 and most extremely during 1998. The errors in the thermal field in the eastern part of the equatorial Pacific, where they are largest, are connected with anomalies of the zonal wind stress in the eastern central part (between 100°W and 140°W, figure 5.5). This suggests that the errors are caused by either

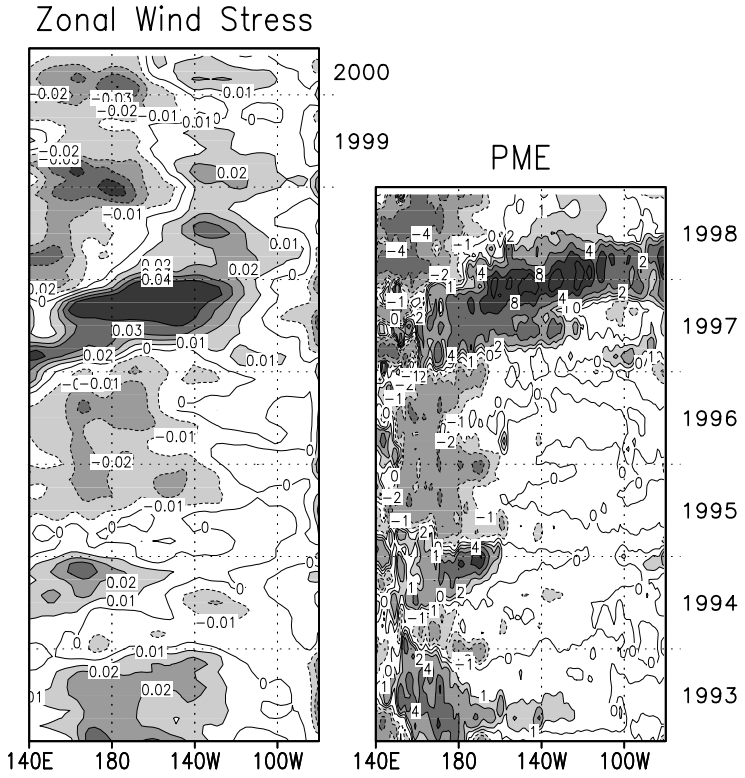

Figure 5.5: *Hovmöller diagrams along the equator of: ECMWF re-analysis zonal wind stress anomalies [N/m^2] (left) and precipitation minus evaporation (PME) anomalies [mm/day] from the satellite-only derived HOAPS dataset (Graßl et al., 2000) (right).*

errors in the wind stress forcing or by an incorrect ocean model response.

Assimilation of T/P SLA and TAO/TRITON in situ measured temperature diminishes these errors (figures 5.3 and 5.4). However, some substantial residual errors remain. Furthermore, errors in SLA of experiment Co-EC appear which are not related to errors in the thermal field, particularly in the western part of the basin in 1993 and 1996 (figure 5.3 left panel). Errors in the same longitudinal band occur also in experiments As-TP-EC and As-TAO-EC (figure 5.3 middle and right panels).

In the first case, 1993, PME anomalies were high over the same area in the western part of the basin (figure 5.5), but simultaneously, anomalously high evaporation, exceeding precipitation is simulated in the three model experiments (figure 5.7). PME is not explicitly prescribed in the ocean simulations, but implicitly derived through restoring of the sea surface salinity (SSS) towards values of its annual cycle as described in chapter 3.1. Hence,

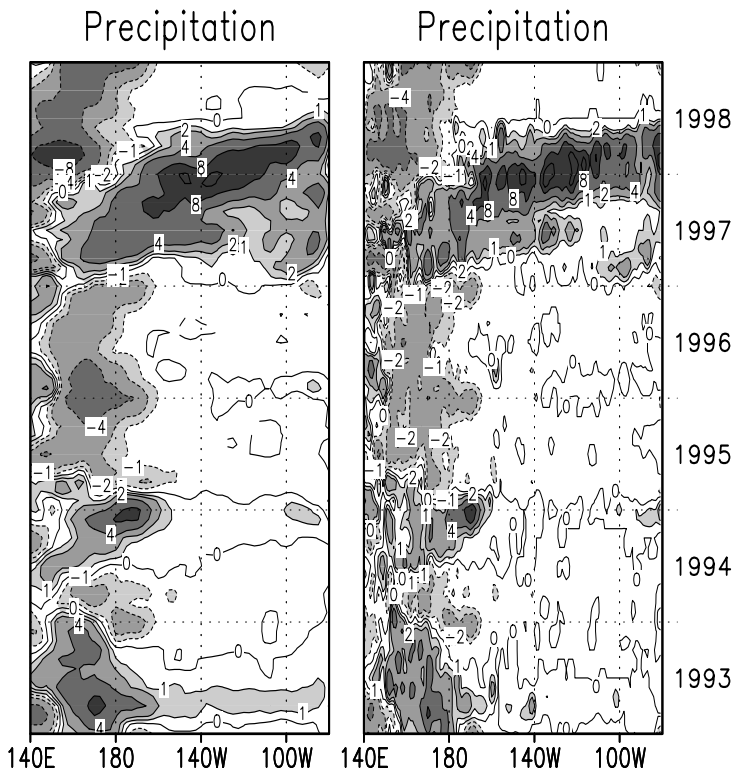

Figure 5.6: *Hovmöller diagrams along the equator of: Xie and Arkin (1997) precipitation anomalies [mm/day] (left) and precipitation anomalies [mm/day] from the satellite-only derived HOAPS dataset (Graßl et al., 2000) (right).*

this parameterisation of PME does not invoke realistic patterns.

In reality, the high precipitation anomalies lead to a fresh water layer at the surface in 1993, which causes a rise of the sea level. This rise is not captured by the ocean simulations due to their unrealistic PME rates, and hence the SLA are underestimated in all three model experiments in the western equatorial Pacific in 1993. The opposite effect takes place in 1995-96, with less than normal PME in the western equatorial Pacific in the observations (figure 5.5), but near normal or higher than normal PME in the simulations (figure 5.7). This induces overestimation of SLA to varying degrees in the three experiments. The differences in the errors of SLA in these two years and in this area are due to the differences in induced PME by SSS restoring (figure 5.7) plus simulated errors in the thermal field (figure 5.4), but all experiments show a net effect of too high SLA due to the errors in the fresh water flux.

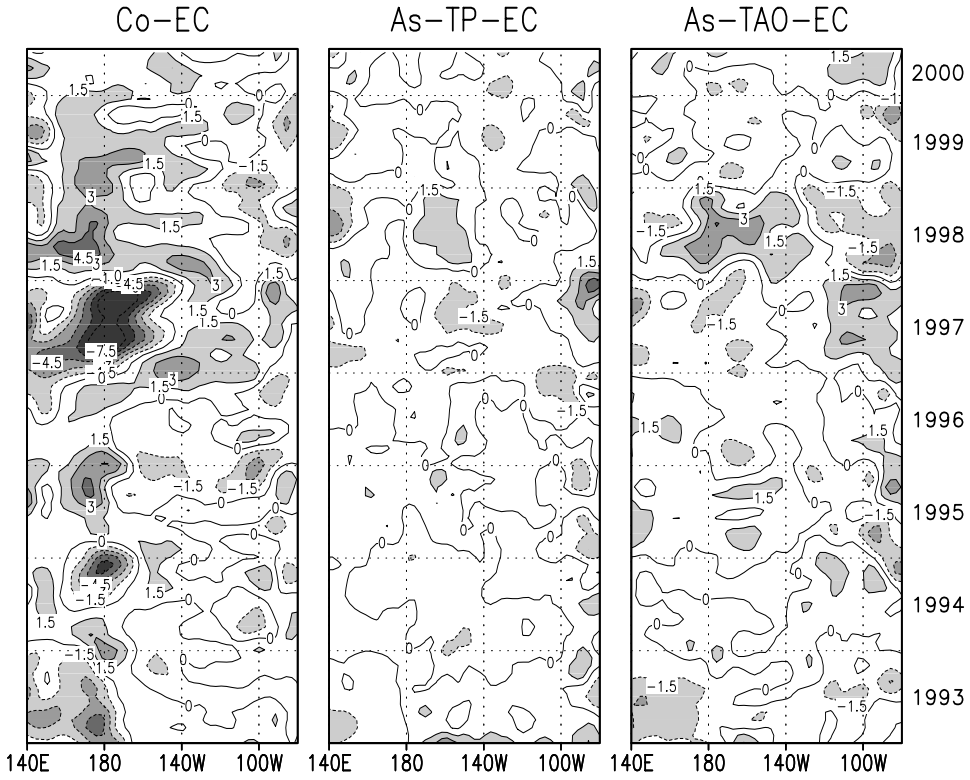

Figure 5.7: *Precipitation minus evaporation (PME) anomalies [mm/day] relative to the annual cycle as Hovmöller diagrams of: Co-EC (left), As-TP-EC (middle) and As-TAO-EC (right).*

With the high SSTA spreading eastward during the development of the 1997 El Niño (figure 5.8) the area of high PME also spreads eastward to the central equatorial Pacific and even further to the east towards the end of 1997 (figure 5.5). These high PME rates are not captured in any of the three model experiments (figure 5.7). Therefore large errors occur in the simulations of the SLA at these times (figure 5.3). This is most easily seen in experiment As-TAO-EC, in which the thermal field is corrected by temperature assimilation. The remaining errors in SLA in this experiment are thus most likely due to the errors in the fresh water flux.

As the assimilation scheme for SLA takes just thermal variations into account, errors may occur if the sea level has changed due to changes in the fresh water flux. That is, the component of sea level signal due to the fresh water flux is projected misleadingly onto the thermal field within the assimilation scheme. Therefore errors in the thermal field of experiment As-TP-EC emerge when fresh water flux anomalies are extreme. For example,

during 1993, the end of 1994/beginning of 1995 and in 1997 PME anomalies were extremely high (figure 5.5) and too high temperature anomalies were induced in the thermal field of the upper 500 m (figure 5.4). On the contrary, when PME anomalies were extremely low in 1995 and 1996 in the western equatorial Pacific, too low temperature anomalies were induced in the thermal field of the upper 500 m (figure 5.4).

Overall, errors in SLA are largest in experiment Co-EC (figure 5.3, left panel; RMS=4.19 cm, averaged along the equator over the period January 1993 until June 2000) and they mainly arise from errors in the wind stress forcing or in ocean model formulation. In experiment As-TP-EC (figure 5.3, middle panel), errors are substantially reduced (RMS=1.88 cm), compared to those of Co-EC and do not exceed 6.0 cm at any time. The errors which occur in As-TP-EC are mainly invoked by misinterpretation of the sea level signal, as surface salinity variations caused by anomalous fresh water fluxes are disregarded. The error reduction of experiment As-TAO-EC (figure 5.3, right panel; RMS=2.93 cm) is less than in the experiment As-TP-EC. The cause of the errors in this experiment is also the fresh water flux, just the effect is another, as in this case temperature instead of SLA is assimilated. However, wind induced or ocean model errors in the SLA of the experiment Co-EC are corrected by both assimilation experiments (As-TP-EC and As-TAO-EC). Nevertheless, new errors are induced with highest values in 1997 and 1998 mostly due to erroneous simulation of fresh water fluxes.

While ocean heat content is crucial for the evolution of ENSO, the SST is important for ocean-atmosphere interactions and therefore essential to force the atmospheric fields in coupled mode. Figure 5.8 shows the temporal evolution of monthly SSTA along 5°N, the equator and 5°S. The anomalies are calculated with respect to the annual cycle over the period from January 1993 to December 1996. The SST data originate from the optimal interpolated dataset by Reynolds and Smith (1994) (hereafter called Reynolds SST), which includes both satellite and in situ data. These SST data are used for and contained in the ECMWF re-analysis dataset (section 2.3). Positive anomalies of SSTA along 5°S as well as 5°N coincide with positive anomalies of SLA (figure 5.1) and vice versa. At the equator, changes of SLA in the central and eastern part appear slightly earlier than changes in SSTA. Propagating structures are less visible in SSTA than in SLA as internal equatorial waves exhibit strongest signals near the thermocline and have thus more influence on SLA than on SSTA.

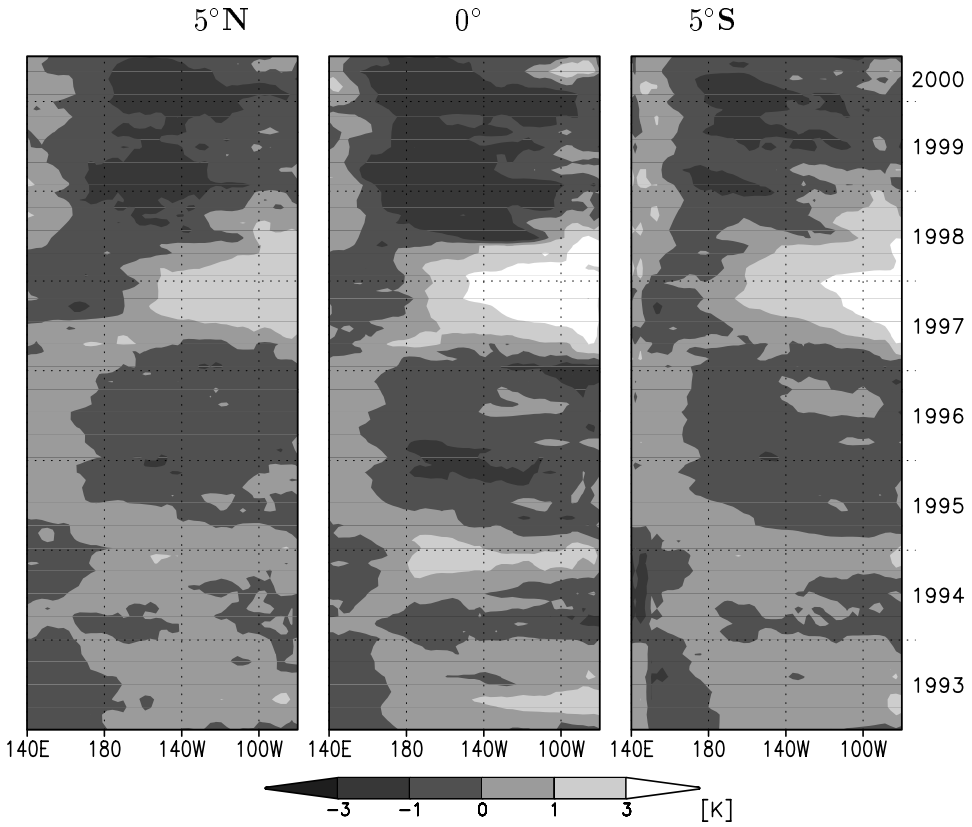

Figure 5.8: *Reynolds SSTA as Hovmöller diagrams along: 5° N (left), the equator (middle) and 5° S (right).*

To investigate whether the model simulates the interannual variability of SST and if assimilation of sea level or in situ measured temperatures reduces errors compared to the experiment Co-EC, Hovmöller diagrams of the difference between SST observations and the three model experiments are shown (figure 5.9). In the experiment Co-EC without assimilation (left panel) errors are largest (RMS=1.11 K), with the strongest errors in the eastern part of the basin. These errors correspond to the errors of SLA (figure 5.3) and to errors of the mean temperature averaged over the upper 500 m (figure 5.4). For the experiment As-TP-EC (figure 5.9, middle panel) errors are substantially reduced (RMS=0.73 K), but they still exceed 2 K in 1997/1998. In 1997 too high SSTA are simulated and correspond with strong heat content errors (figure 5.4, middle panel) at the same time. The erroneously low SSTA in 1998 have no corresponding signatures in the heat content anomalies. The overestimation of SSTA in 1997 may result because of three different reasons together. First, as mentioned before, the precipitation part of the SLA signal might be projected

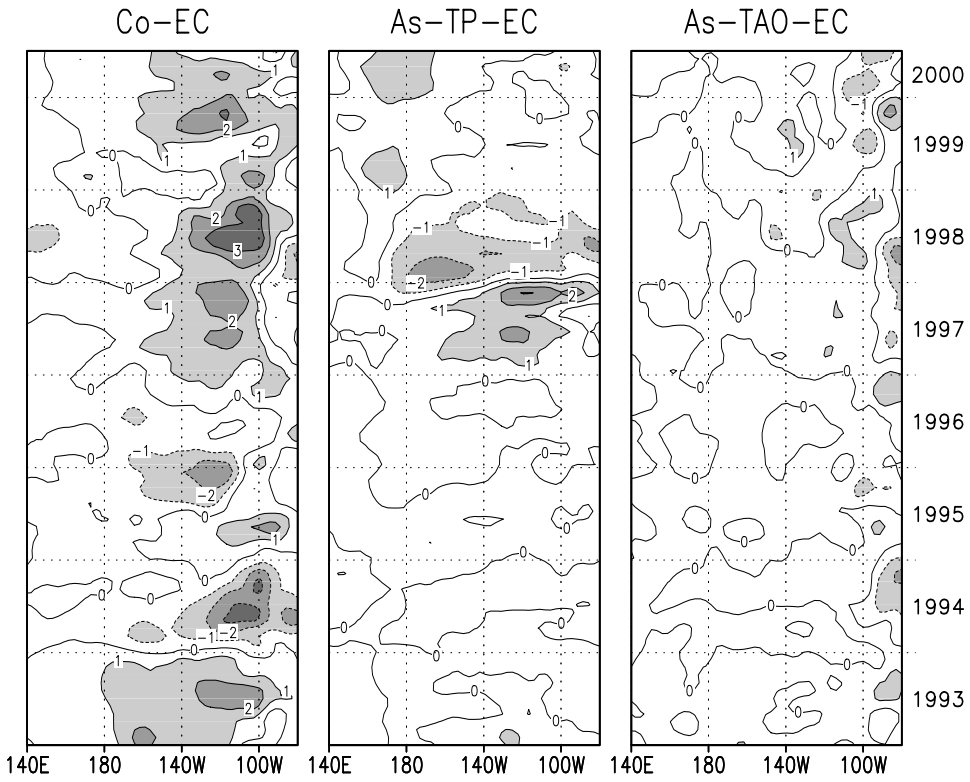

Figure 5.9: *SSTA differences [K] as Hovmöller diagrams along the equator: Co-EC minus Reynolds SSTA (left), As-TP-EC minus Reynolds SSTA (middle) and As-TAO-EC minus Reynolds SSTA (right). A 9-point smoothing over space and time has been applied and errors of more than 1 K are shaded.*

onto the thermal structures by the assimilation. Secondly, the core of the highest anomalies in the eastern equatorial Pacific lies too high beneath the surface in the ocean model simulations. Comparisons with the TAO/TRITON observations have shown this, which can e.g. also be seen in December 1997 in figure 5.2. Thirdly, the assumption of a linear relationship between the PCs of the vertical EOFs and the SLA might not hold for strong anomalies and furthermore this model-derived relationship might be different in reality. Figure 5.10 illustrates this in terms of SSTA and SLA. An observed, high SLA of about 20 cm relates to a SSTA of about 3 K, whereas the same observed SLA projected with the model relation yields a SSTA of about 5 K. However, the linear relationship between the PCs of the vertical EOFs and the SLA might change this difference in the SSTA.

The error reduction of SSTA in the experiment As-TAO-EC (figure 5.9, right panel, RMS=0.55 K) is even better than in the experiment As-TP-EC. However, one would ex-

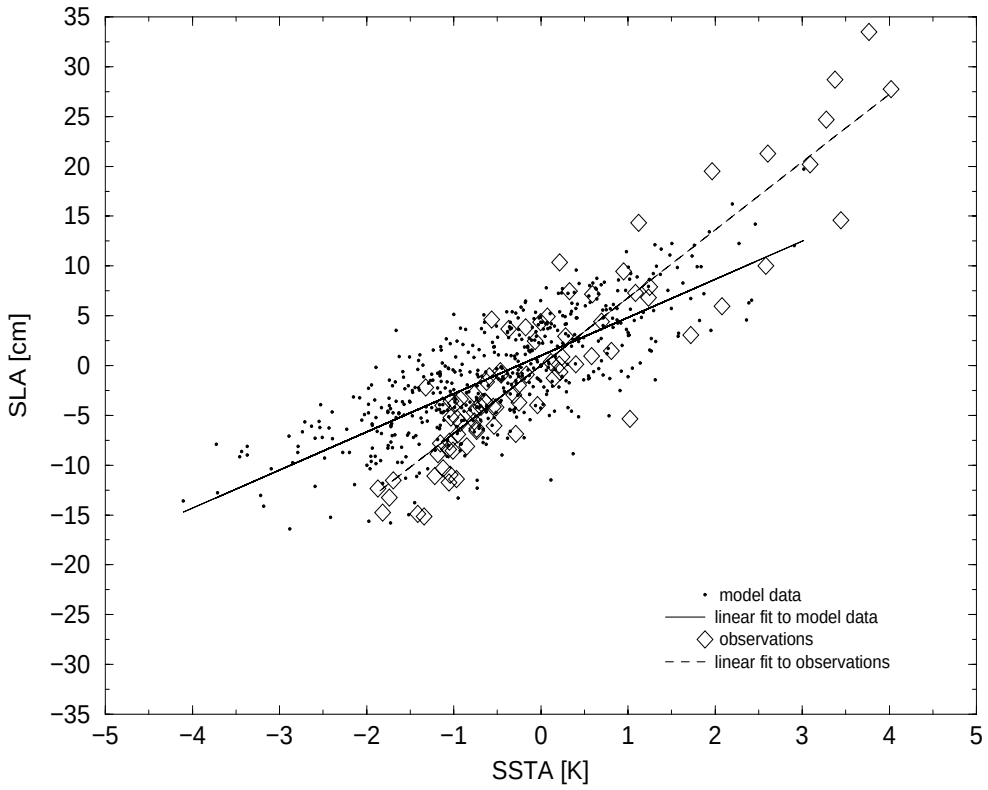

Figure 5.10: *Scatter diagram of SSTA [K] and SLA [cm] in the eastern equatorial Pacific (averaged over 150 W to 90 W at the equator). Simulated data are taken from the same 45 year ocean model simulation from which the assimilation scheme was calculated and are marked with dots. The observations are T/P SLA and Reynolds SSTA from 1993 to 1999 and are marked with diamonds. The corresponding regression lines are depicted with solid and dashed lines respectively.*

pect this, as surface temperature data are also assimilated in this experiment. Hence, the erroneously low SLA in 1997 of As-TAO-EC (figure 5.3, right panel) has neither a corresponding signature in the SST, nor in mean upper ocean temperature (figure 5.4, right panel). It is thus probably caused by unrealistic salinity.

5.2 Analysis of Forecast Experiments

The effect of SLA assimilation (experiment As-TP-EC) on ENSO forecasting is determined by the comparison with the no assimilation case (experiment Co-EC) and the experiment with assimilation of in situ measured temperatures (As-TAO-EC). The Niño3 region, rang-

ing from 150-90°W and from 5°N-5°S is taken for verification. The relative performance of the three forecast ensembles initialised with the three different ocean analyses (Co-EC, As-TP-EC and As-TAO-EC, table 5.1) is estimated by comparing the predicted SSTA with the observed values of the Reynolds SSTA. According to their initialisation experiments the forecast ensembles are referred to as Co-EC-fc, As-TP-EC-fc and As-TAO-EC-fc respectively. The ensembles consist of one coupled ocean-atmosphere forecast experiment initialised every 3rd month.

Anomalies of the predicted SST of each experiment are computed relative to their respective seasonal climatologies. The climatology is calculated separately for 1-year forecasts started in March, June, September and December. Thus, the climatology for forecasts started in March covers March to February, the one for June starts covers June to May etc..

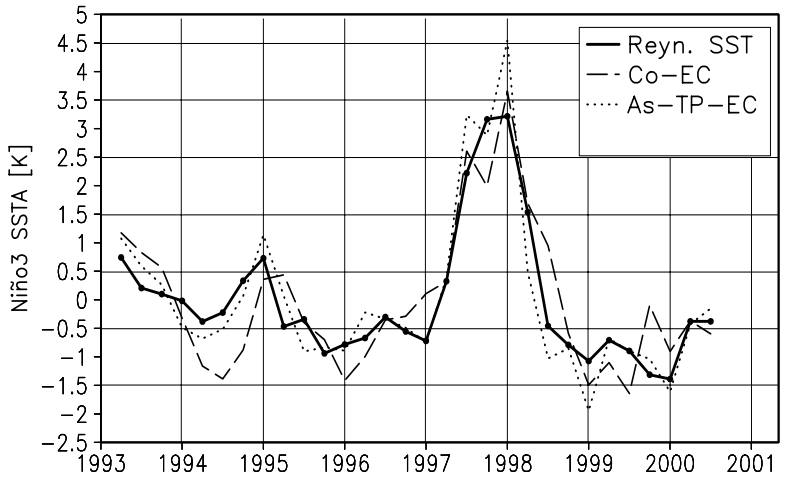

Figure 5.11: *Seasonal means of SSTA averaged over the Niño3 region of: Reynolds SST observations (solid line) and predicted SSTA at lag = 1 season (month 1-3) from the forecast ensemble Co-EC-fc (dashed line) and from the forecast ensemble As-TP-EC-fc (dotted line).*

In mid 1994 forecast ensemble Co-EC-fc shows more than 1 K deviation from the observed anomaly (figure 5.11), whereas forecast ensemble As-TP-EC-fc corresponds generally much better to the observations. However, at the peak of the 1997 El Niño, the forecasts from As-TP-EC-fc predict too warm conditions due to the overestimation of heat content, manifesting itself as too high SLA in 1997 (figure 5.3) and too high SSTA (figure 5.9) in the initialisation run. As-TAO-EC-fc forecasts December 1997 better for 1 to 3 months lead time (figure 5.12) but overestimates the subsequent La Niña in mid 1998. For better clear-

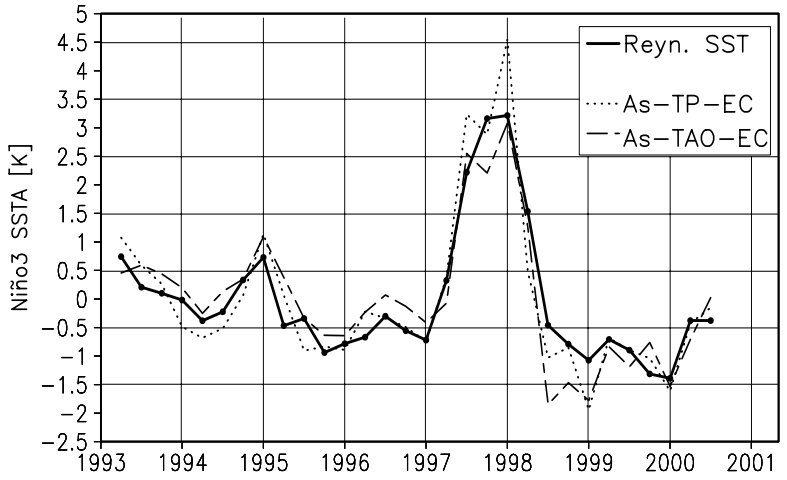

Figure 5.12: *Seasonal means of SSTA averaged over the Niño3 region of: Reynolds SST observations (solid line) and predicted SSTA at lag = 1 season (month 1-3) from the forecast ensemble As-TP-EC-fc (dotted line) and from the forecast ensemble As-TAO-EC-fc (dashed line).*

ness the results are displayed in two figures for each seasonal lag. The observations and the results from As-TP-EC-fc are displayed in all figures, whereas the results of Co-EC-fc and As-TAO-EC-fc are only displayed in one of them appropriately (e.g. figures 5.11 and figure 5.12).

All three forecast ensembles capture basically the strong warming in 1997 at short lead times up to one season. With increasing lead time of the forecasts this is not the case anymore (figures 5.13 and 5.14). The forecasts still show a warming, but it is slightly delayed in the case of SLA assimilation (As-TP-EC-fc). The peak value of the warming in 1997, however, is predicted better at 2 seasons lead time.

Figures 5.15 and 5.16 show the anomaly correlation coefficients (ACC) and the root mean square errors (RMS) between monthly mean SSTA of the forecasts from the three ensembles and monthly mean Reynolds SSTA observations for the Niño3 region. The SSTA at initial time (lead time 0) are not perfect for ensemble As-TP-EC-fc, with an ACC of about 0.9 and an RMS error of 0.6 K. The same is true for the ensemble Co-EC-fc, which has even worse initial errors. The Hovmöller diagrams and their RMS errors of SSTA of the initialisation runs (figure 5.9 and description in previous section) showed relatively large errors in SSTA for both of these experiments. However, the initial subsurface structures seem to be reasonable, as the ACC do not drop much after 3 months. For the ACC as well

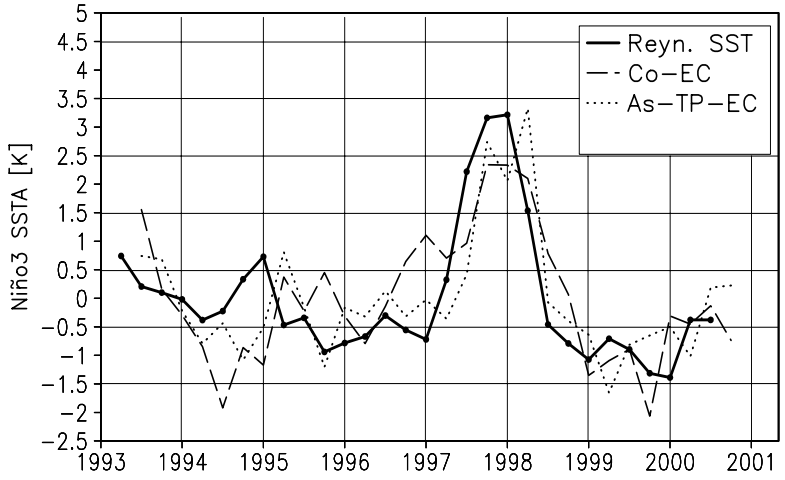

Figure 5.13: *Seasonal means of SSTA averaged over the Niño3 region of: Reynolds SST observations (solid line) and predicted SSTA at lag = 2 seasons (month 4-6) from the forecast ensemble Co-EC-fc (dashed line) and from the forecast ensemble As-TP-EC-fc (dotted line).*

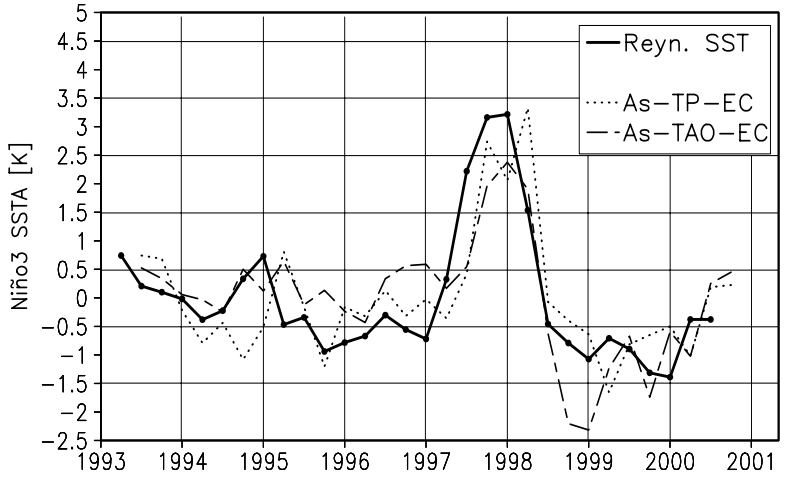

Figure 5.14: *Seasonal means of SSTA averaged over the Niño3 region of: Reynolds SST observations (solid line) and predicted SSTA at lag = 2 seasons (month 4-6) from the forecast ensemble As-TP-EC-fc (dotted line) and from the forecast ensemble As-TAO-EC-fc (dashed line).*

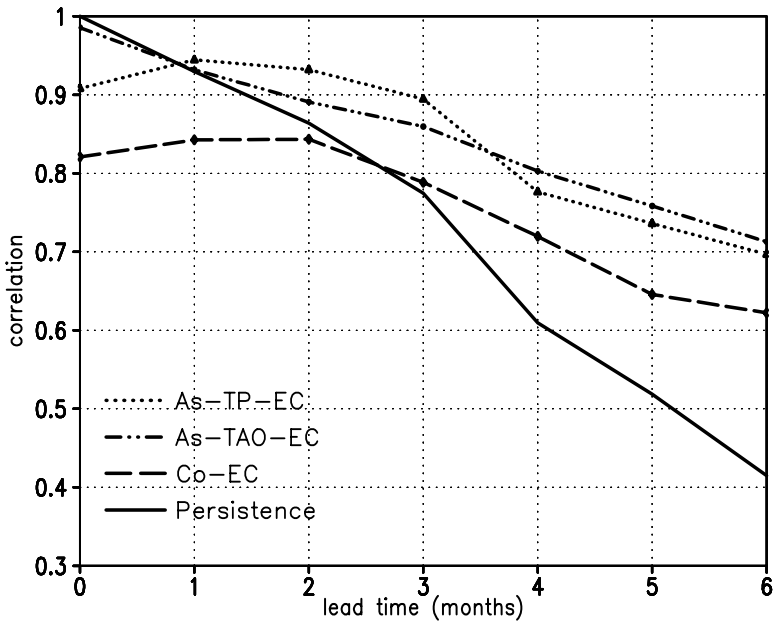

Figure 5.15: *Anomaly correlation coefficients of predicted and observed (Reynolds SST) monthly mean SSTA averaged over all forecasts for the three ensembles Co-EC-fc, As-TP-EC-fc and As-TAO-EC-fc and for persistence, calculated for the Niño3 region as a function of lead time.*

as the RMS errors, forecasts started without assimilation can just beat persistence from 3 months lead time onwards. On the contrary, both assimilation experiments beat persistence from one month lead time onwards for the ACC and from two months lead time onwards for the RMS error. The skills of both assimilation experiments show no clear difference at any time lag.

A Mann-Whitney test (Conover, 1980) has been applied to investigate if the mean of the probability density function of the absolute error is significantly shifted between the two assimilation experiments (As-TP-EC-fc and As-TAO-EC-fc). Their mean values are not significantly shifted from each other at the 95% confidence level for all lead times.

Comparing each of the assimilation experiments with the experiment without assimilation (Co-EC-fc) leads to the result that Co-EC-fc and As-TP-EC-fc show only for the first two months significantly shifted means at the 95% confidence level. Co-EC-fc and As-TAO-EC-fc in turn show significantly shifted means at the 99% confidence level for one month lead and no significance at the 95% confidence level for lead times beyond the first month.

Overall, this shows that the impact of altimeter data assimilation cannot be distinguished

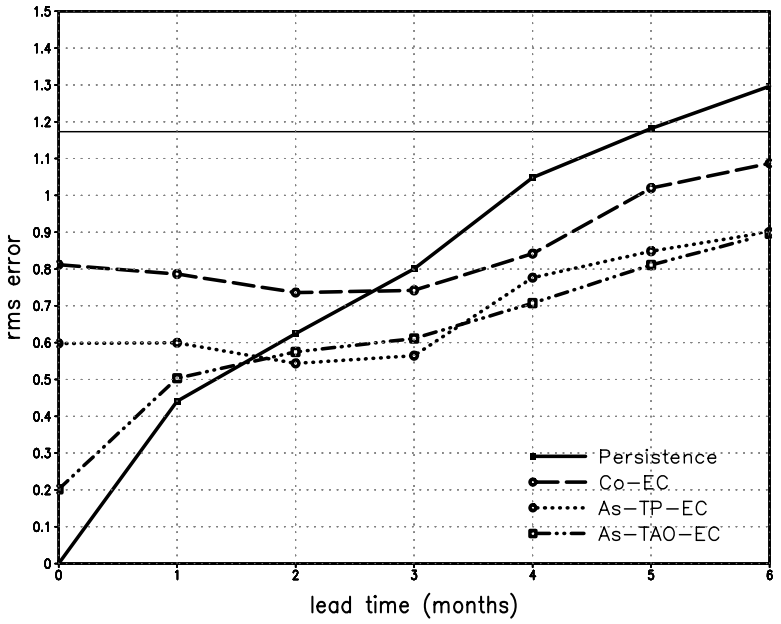

Figure 5.16: *RMS error [K] between monthly mean SSTA of the forecasts from the three ensembles (Co-EC-fc, As-TP-EC-fc and As-TAO-EC-fc) and those of the Reynolds observations for the Niño3 region as a function of lead time. The RMS of the Niño3 SST observations is marked as a straight line.*

from the impact of subsurface temperature data assimilation in their predictive skill. However, both show better forecast skill for all lead times in terms of ACC and RMS error relative to the control experiment. Although this indicates that data assimilation improves the forecasts, it cannot be shown rigorously by a statistical test.

5.3 Seasonality of Forecast Skill

The seasonal dependence in the persistence of the eastern tropical Pacific SST anomalies is well established and has been described in many papers (e.g. Wright, 1988). This autocorrelation of tropical Pacific SSTA attains a minimum in boreal spring/summer and a maximum in boreal fall/winter. This can also be seen for the period regarded here. Many ENSO prediction models show similar seasonal dependence in skill, with ACC values dropping in spring (e.g. Goswami and Shukla, 1991; Latif and Flügel, 1991). This phenomenon is called the spring predictability barrier. However, Latif et al. (1998) state that the cause

of the spring barrier is still unclear and that the spring predictability barrier may even be a problem of the models.

In the following, it is investigated if there is a seasonality in forecast skill of the three forecast ensembles Co-EC-fc, As-TP-EC-fc and As-TAO-EC-fc and whether it is influenced by assimilation or not. Figure 5.17 shows the ACC for lead times up to 12 months as function of calendar month. As the forecasts were started every third month, the diagram shows just four starts per year, each representing an ACC calculated over only 7 to 8 forecasts. Hence, one has to keep in mind that the seasonally stratified skills may have large uncertainties.

The seasonal skill of the persistence (figure 5.17 upper left panel) shows that conditions within the Niño3-region are more stable in boreal autumn and winter and less stable at the end of spring/beginning of summer. This is comparable to the outcome of previous studies (e.g. Wright, 1988) and shows that the period over which the skills are computed, although it covers only 7.5 years, is at least a representative period. Thus, as the seasonal skills of the experiments are calculated from the same ensemble sizes and for the same period as those of the persistence, comparisons to seasonal skills of other models are reasonable.

The skills of all three experiments (figure 5.17 lower left and upper and lower right panels) show a seasonal dependence of the ACC values, similar to the spring predictability barrier found in other forecast studies (Latif and Graham, 1992; Kirtman et al., 2000). After a weakening of the forecast skill for April/May/June, models indicate a return of skill for the summer months, which has also been shown with other models (Kirtman et al., 2000). This does not show up in the persistence forecast (figure 5.17 upper left panel).

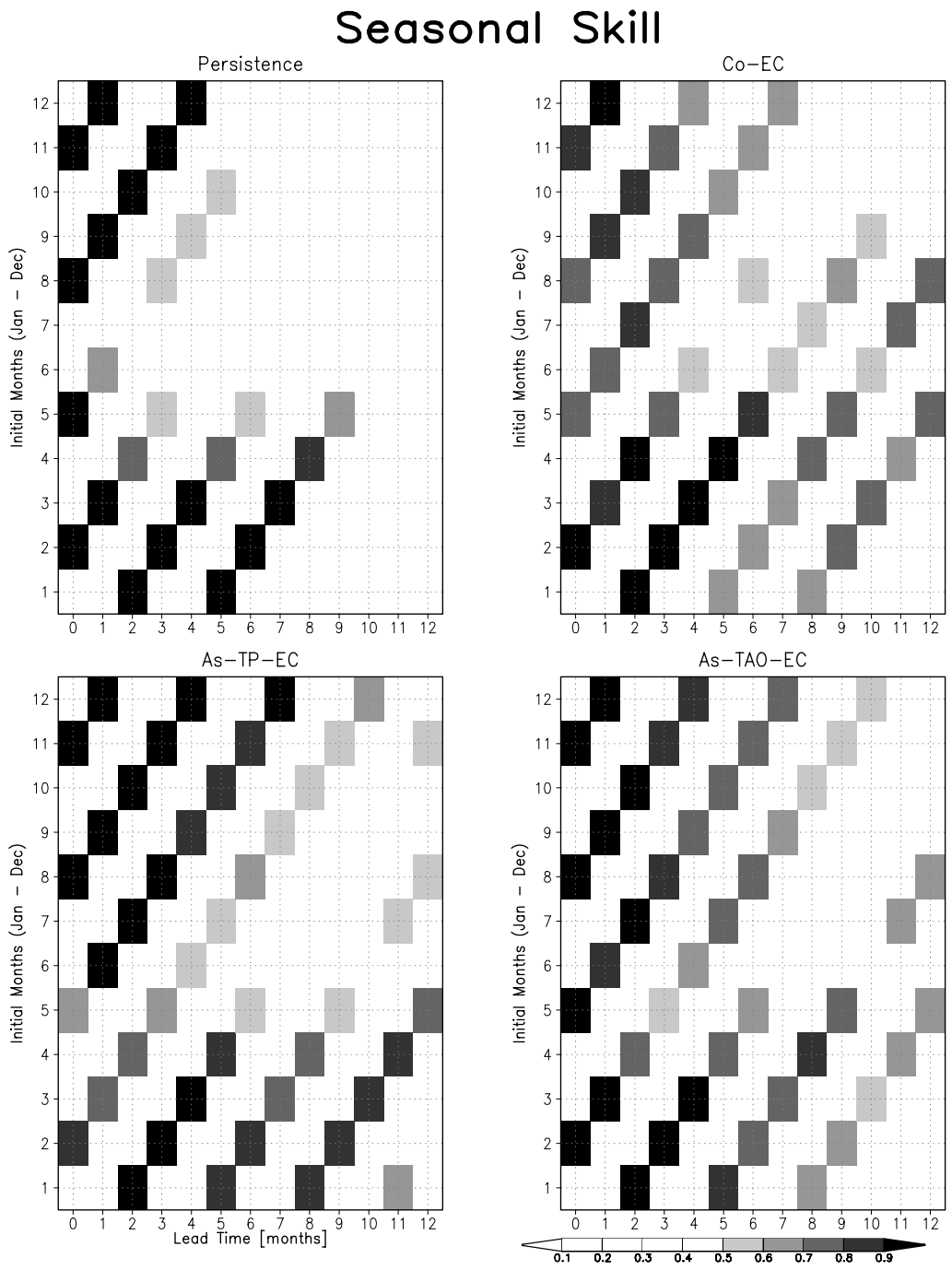

Figure 5.17: *Anomaly correlation coefficients of figure 5.15 as function of calendar month and lead time. Persistence (upper left), forecast ensembles initialised from the control experiment (Co-EC-fc, upper right), forecast ensembles initialised from the T/P assimilation experiment (As-TP-EC-fc, lower left) and forecast ensembles started from the TAO/TRITON assimilation experiment (As-TAO-EC-fc, lower right)*

Chapter 6

Sensitivity to Bivariate Data Assimilation

Fischer (2000) suggested that a multivariate projection, using SSH together with SST for projection onto the subsurface thermal field, improves ocean initial conditions. In contrast to the univariate scheme (chapter 4.2), the bivariate assimilation method (chapter 4.3) allows a representation of more complex vertical structures. ENSO events are preceded by high TA in the subsurface western and central equatorial Pacific, while often at the surface SSTA of the reverse sign still prevail. The bivariate method is therefore particularly important for these states of ENSO when thermal precursors occur. Whether the improvements of the ocean initial conditions produced by this bivariate projection of SLA also affect and improve the ENSO forecast skill is addressed in this chapter.

All experiments in this chapter are forced by NCEP/NCAR re-analysis data (chapter 2.3) and are analysed for the period from January 1993 to December 1996 (table 6.1).

Name	Initialisation	Period	Forcing	Assimilation
Co-NC	clim. Dec[1]	'73-'97	NCEP/NCAR	no
As-TP-NC	Dec'92 of Co-NC	'93-'97	NCEP/NCAR	T/P (univariate)
As-TPSST-NC	Dec'92 of Co-NC	'93-'97	NCEP/NCAR	T/P and SSTA (bivariate)

Table 6.1: *Characteristics of the control experiment (Co-NC), the Topex/Poseidon assimilation experiment (As-TP-NC) and the bivariate assimilation experiment (As-TPSST-NC).*

[1]Started from a 50 year control run, initialised with Levitus climatology (Levitus, 1982)

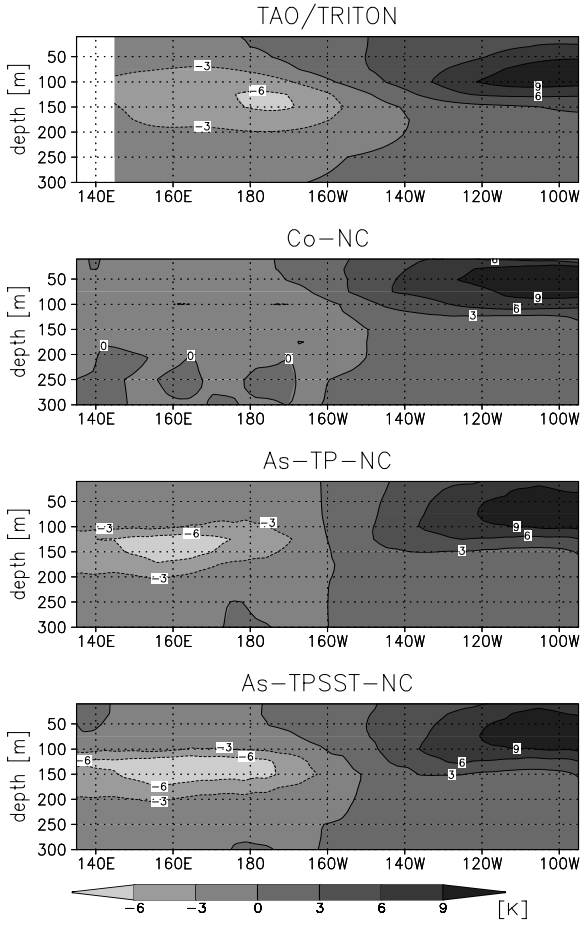

Figure 6.1: *Mean temperature anomalies in December 1997 for the zonal section at the equator: TAO/TRITON observations (upper), control run Co-NC (upper middle), univariate assimilation run As-TP-NC (lower middle), bivariate assimilation run As-TPSST-NC (lower). Anomalies are relative to the annual cycle.*

In figure 6.1, TA in December 1997 relative to the annual cycle derived from the period January 1993 to December 1996 are shown for the zonal section at the equator. The bivariate assimilation scheme (experiment As-TPSST-NC) leads to an improved representation of TA in the central Pacific: positive SSTA stretch further to the west near the surface while negative TA stretch further to the east near 150 m depth.

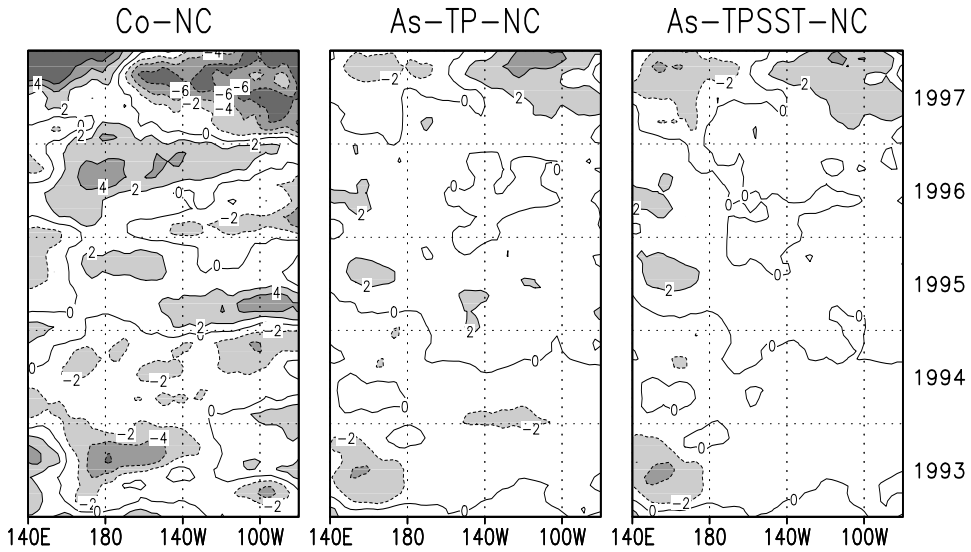

Figure 6.2: *SLA errors [cm] as Hovmöller diagrams along the equator of the three simulations: Co-NC minus T/P observations (left), As-TP-NC minus T/P observations (middle) and As-TPSST-NC minus T/P observations (right).*

The temporal evolutions of SLA errors are shown in figure 6.2. The T/P observations have been averaged to monthly data and interpolated onto the ocean model grid. Annual cycles have been removed before computing the differences. For clarity, a 9-point smoothing over space and time has been applied and differences of more than $\pm$ 2 cm are shaded.

Both assimilation experiments show similar errors in SLA. RMS errors along the equator over the whole period are slightly smaller for experiment As-TP-NC (RMS=1.57 cm) than for experiment As-TPSST-NC (RMS=1.62 cm). Both have strongly reduced errors relative to the experiment without assimilation (Co-NC, RMS=3.16 cm).

While the bivariate experiment shows no improvement of the errors of SLA, there is a positive impact on the SSTA error in particular in 1997 as shown in figure 6.3. The overall error of the experiment As-TP-NC (RMS = 0.59 K) is reduced compared to the experiment without assimilation (Co-NC, RMS = 0.66 K), whereas the bivariate assimilation

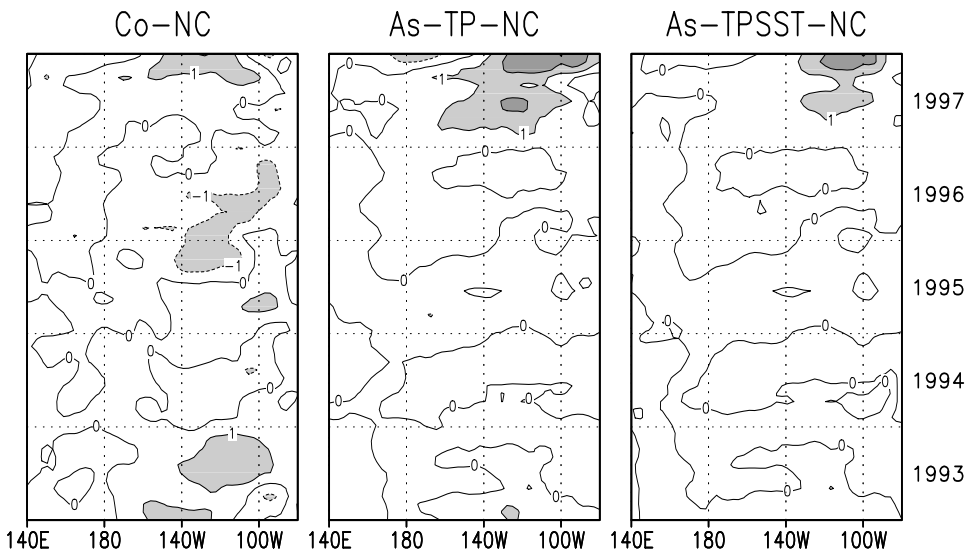

Figure 6.3: *SSTA differences [K] as Hovmöller diagrams along the equator: Co-NC minus Reynolds SSTA (left), As-TP-NC minus Reynolds SSTA (middle) and As-TPSST-NC minus Reynolds SSTA (right).*

(experiment As-TPSST-NC) reduces the error in SSTA at the equator more drastically ($RMS = 0.33\,\mathrm{K}$).

Thus, the bivariate method improves the TA along the equator especially in terms of stratification and reduces the RMS error of equatorial SSTA to about half of the value of the univariate case. The SLA error, however, remains basically unchanged compared to the univariate method.

The forecast ensembles (As-TP-NC-fc and As-TPSST-NC-fc) initialised with the two assimilation experiments As-TP-NC and As-TPSST-NC evolve very similar at one season lead time (figure 6.4). At longer lead times they cannot clearly be distinguished either (figure 6.6). In figures 6.5 and 6.7, the forecast ensemble of Co-NC is displayed additionally to show the differences to the two assimilation ensembles. For clarity only the univariate forecast ensemble (As-TP-NC-fc) is shown in these figures.

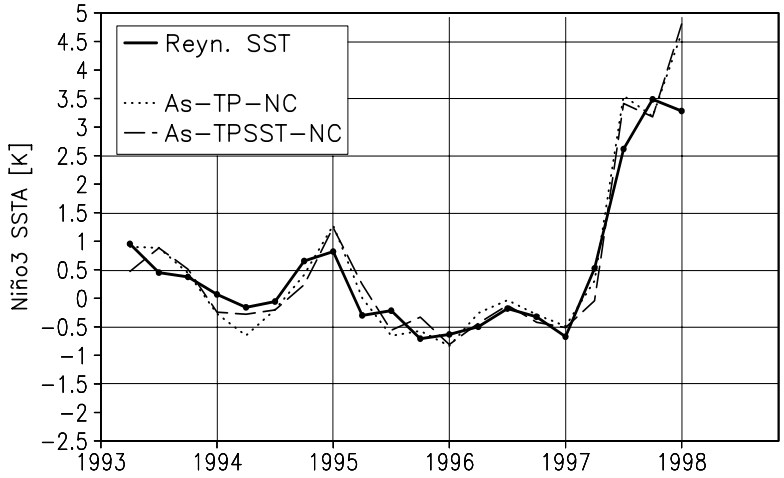

Figure 6.4: *Seasonal means of SSTA averaged over the Niño3 region of: Reynolds SST observations (solid line) and predicted SSTA at lag = 1 season (month 1-3) from the forecast ensemble As-TP-NC-fc (dotted line) and from the forecast ensemble As-TPSST-NC-fc (dashed line).*

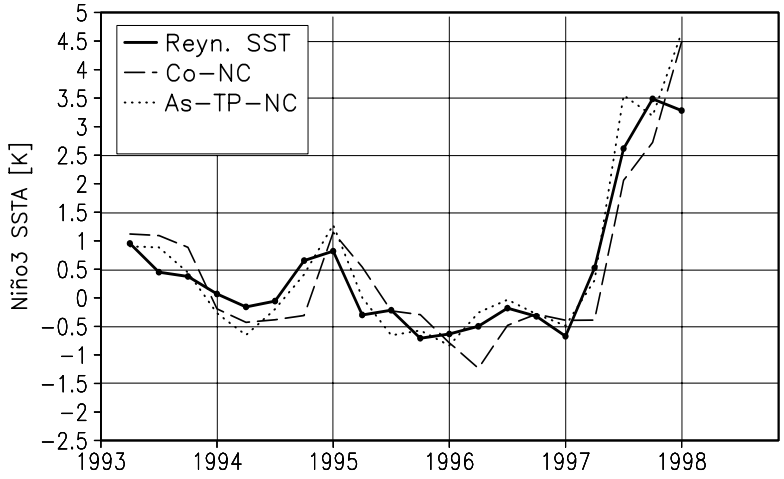

Figure 6.5: *Seasonal means of SSTA averaged over the Niño3 region of: Reynolds SST observations (solid line) and predicted SSTA at lag = 1 season (month 1-3) from the forecast ensemble Co-NC-fc (dashed line) and from the forecast ensemble As-TP-NC-fc (dotted line).*

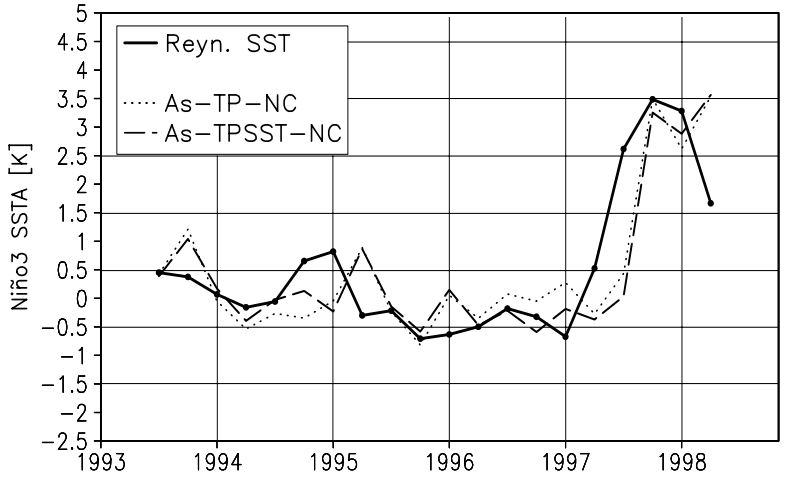

Figure 6.6: *Seasonal means of SSTA averaged over the Niño3 region of: Reynolds SST observations (solid line) and predicted SSTA at lag = 2 seasons (month 4-6) from the forecast ensemble As-TP-NC-fc (dotted line) and from the forecast ensemble As-TPSST-NC-fc (dashed line).*

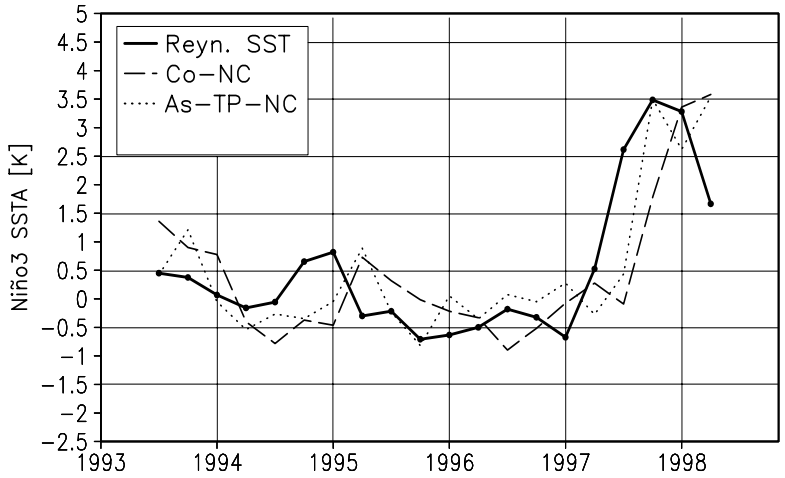

Figure 6.7: *Seasonal means of SSTA averaged over the Niño3 region of: Reynolds SST observations (solid line) and predicted SSTA at lag = 2 seasons (month 4-6) from the forecast ensemble Co-NC-fc (dashed line) and from the forecast ensemble As-TP-NC-fc (dotted line).*

Figure 6.8 shows the anomaly correlation coefficients, figure 6.9 the RMS error between monthly mean SST anomalies of the forecasts from the three experiments and monthly mean observed SST anomalies (Reynolds and Smith, 1994) for the Niño3 region. Both skill measures are very similar for both forecast ensembles.

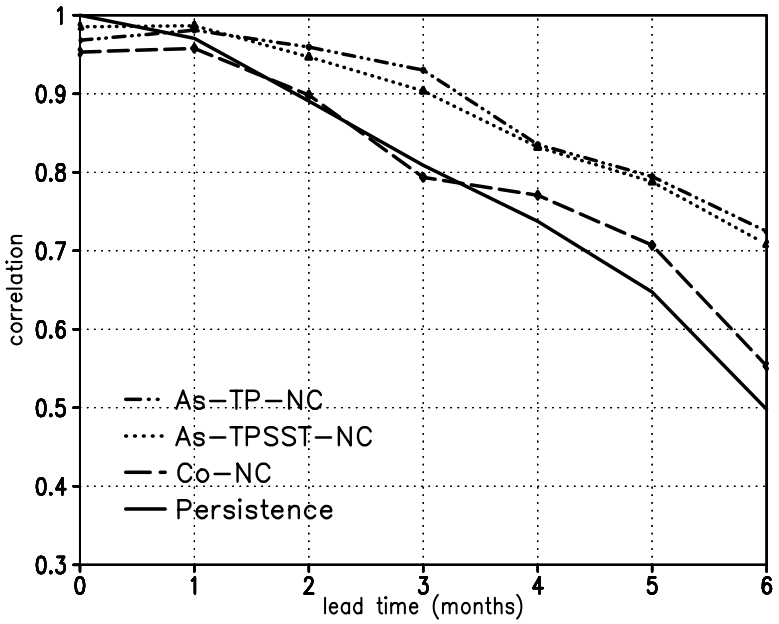

Figure 6.8: *Anomaly correlation coefficients of predicted and observed (Reynolds SST) monthly mean SSTA averaged over all forecasts for the three ensembles Co-NC-fc, As-TP-NC-fc and As-TPSST-NC-fc and for persistence, calculated for the Niño3 region as a function of lead time.*

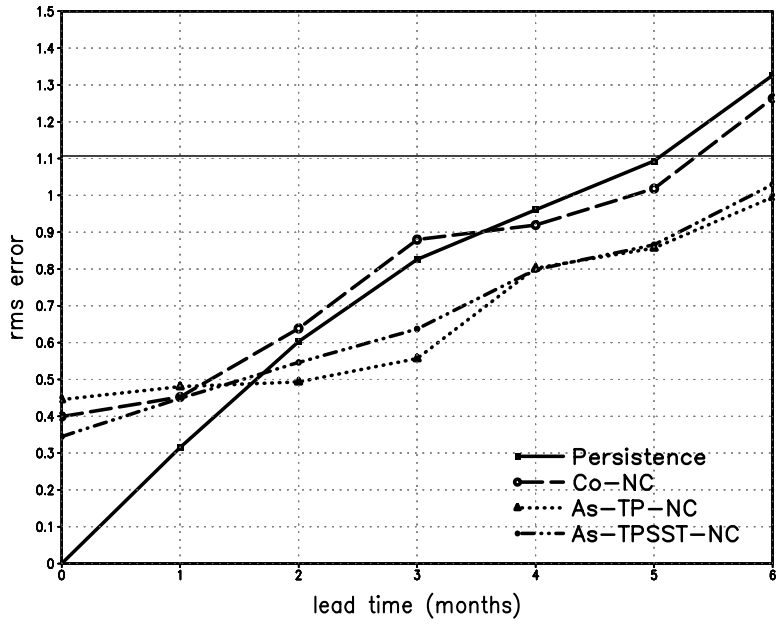

Figure 6.9: *RMS error [K] between monthly mean SSTA of the forecasts from the three ensembles (Co-NC-fc, As-TP-NC-fc and As-TPSST-NC-fc) and those of the Reynolds observations for the Niño3 region as a function of lead time. The RMS of the Niño3 SST observations is marked as a straight line.*

In conclusion, although the bivariate method improves somewhat the ocean initial conditions, this is not reflected in the forecast skill.

Chapter 7

Sensitivity to Different Atmospheric Forcings

In chapters 5 and 6, two different sets of atmospheric forcing fields, one from ECMWF and one from NCEP/NCAR have been used for the initialisation runs. Although both sets of atmospheric forcing fields stem from state of the art re-analyses, they lead to differences in the experiments. In the following, these differences between the experiments are presented and possible underlying reasons are discussed. The results are discussed in the context of T/P data assimilation. Additionally, it is tested, whether these differences have also an influence on the forecast skill. All of these analyses are made for the period from January 1993 to December 1997, unless otherwise annotated, as this period is covered by all of the experiments (tables 5.1 and 6.1).

7.1 Differences in Forcing and Corresponding Ocean States

Vertical temperature profiles of the observations and the experiments Co-NC (NCEP/NCAR forced run without assimilation, table 6.1) and Co-EC (ECMWF forced run without assimilation, table 5.1) along the equator for December 1997 are shown in figure 7.1. In December 1997, Co-NC simulates too small negative TA in the western part of the basin

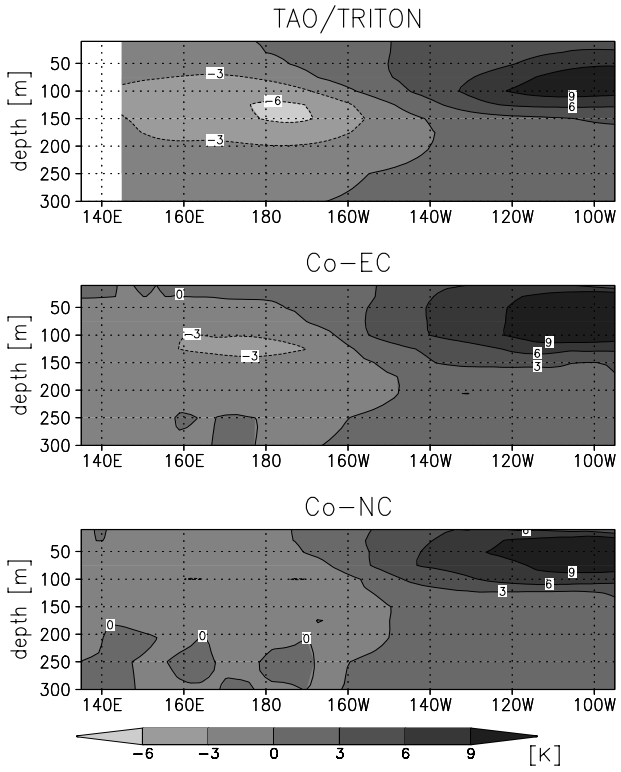

Figure 7.1: *Mean temperature anomalies in December 1997 for the zonal section at the equator: TAO/TRITON observations (upper), control run Co-EC forced with atmospheric fields from ECMWF (middle), control run Co-NC forced with atmospheric fields from NCEP/NCAR (lower). Anomalies are relative to the annual cycle.*

(figure 7.1 lower panel) and the core of the positive TA lies too close to the surface. Experiment Co-EC shows stronger negative TA in the western part of the basin (figure 7.1 middle panel), although they are not as strong as observed. The core of the positive anomalies in the east is simulated deeper than in experiment Co-NC. Thus, figure 7.1 shows that considerable differences of TA between these two model simulations exist, which differ only in their forcing fields.

Co-NC and Co-EC also show differences in their sea surface temperature anomalies (SSTA), e.g. in the Niño3 region, shown in figure 7.2. The SSTA of Co-NC correlates higher with observations ($r = 0.96$) for this area and the considered time period than Co-EC ($r = 0.89$). Especially in the period from 1992 until 1995, the SSTA of Co-EC are unrealistically extreme, for both warm and cold anomalies, which is most likely due to the wind stress.

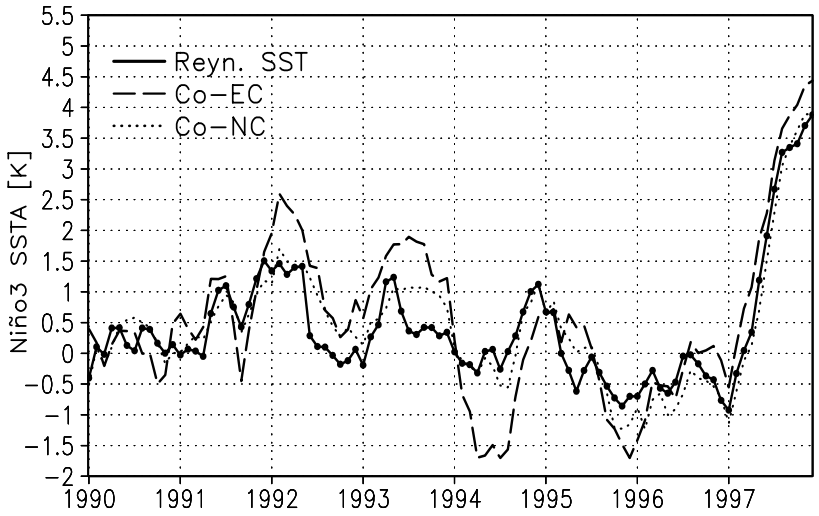

Figure 7.2: *SSTA [K] relative to the annual cycle averaged over the Niño3 region of: Reynolds SST (solid), the ECMWF forced experiment Co-EC (dashed) and the NCEP/NCAR forced experiment Co-NC (dotted).*

The wind stress determines the inclination of the thermocline and the upwelling in the eastern tropical Pacific, and both determine the SST in this region. The wind stress has thus an indirect effect on the variability of the SST in the eastern part of the basin.

The annual mean zonal wind stresses of ECMWF are stronger than those of NCEP/NCAR over most of the Pacific (figure 7.3). In addition, the variability of the ECMWF wind stresses is also higher than those of NCEP/NCAR. In particular, ECMWF wind stresses show stronger anomalies than those of NCEP/NCAR (figure 7.4) at the times, when the model run forced by ECMWF fields shows the largest errors (figure 7.2), e.g. in early 1992 and in 1993.

Up to present wind stresses over the ocean are not sufficiently well known. Therefore, it cannot be distinguished, if either the model over-reacts to the wind stresses or if the wind stresses themselves are unrealistic, or even both. However, similar differences between the wind products of ECMWF and NCEP/NCAR re-analysis are found for the period 1991-1993 by comparison with TAO/TRITON buoy observations by Smull and McPhaden (1998). Studies like this help to identify shortcomings of the re-analysis products, which might lead to their improvement in the future.

As the wind stress determines the inclination of the equatorial thermocline in the Pacific,

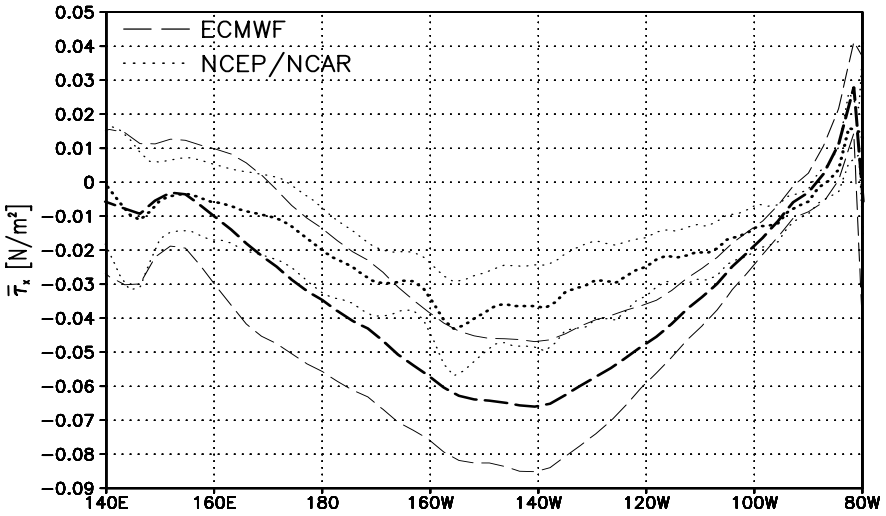

Figure 7.3: *Mean equatorial zonal wind stresses ($\bar{\tau}_x$) for the years 1993 to 1996 [N/m^2] averaged over $\pm 2^\circ$ latitude (thick lines) and the corresponding standard deviations (thin lines) of: ECMWF wind stresses (dashed), NCEP/NCAR wind stresses (dotted).*

the effect of the forcing datasets of both re-analyses on the thermocline is investigated in the following. The depth of the thermocline can be associated with the depth of the 20°C isotherm (D20) (McPhaden et al., 1998). Both terms will be used synonymously in the following. Figure 7.5 displays the D20 along the equator for Co-EC, Co-NC and at four distinct sites from the TAO/TRITON array. It suggests that the higher mean ECMWF wind stress leads to a more inclined mean thermocline within experiment Co-EC than in experiment Co-NC. The thermocline variability of Co-EC is also higher than that of Co-NC, induced by the higher wind stress variability of Co-EC. Although the thermocline of Co-EC is deeper than that of Co-NC, it is still too shallow, compared to the observations. In addition, whereas the observed variability of D20 is captured reasonable well in the west by Co-EC, it is just half of the observed variability in the east and even less for Co-NC.

With the higher than observed SST variability of Co-EC, its surface initial conditions for forecasts exhibit large errors. Therefore the forecast skill of the forecast ensemble Co-EC-fc is lower for the first two months lead time than that of Co-NC-fc (figure 7.6). Their predictive skills are comparable for 3 to 6 months lead time. However, for lead times of 7 months and longer the forecast ensemble Co-EC-fc shows a higher predictive skill. This might be related to the more realistic mean thermocline depth of Co-EC, but this assumption has not yet been proven.

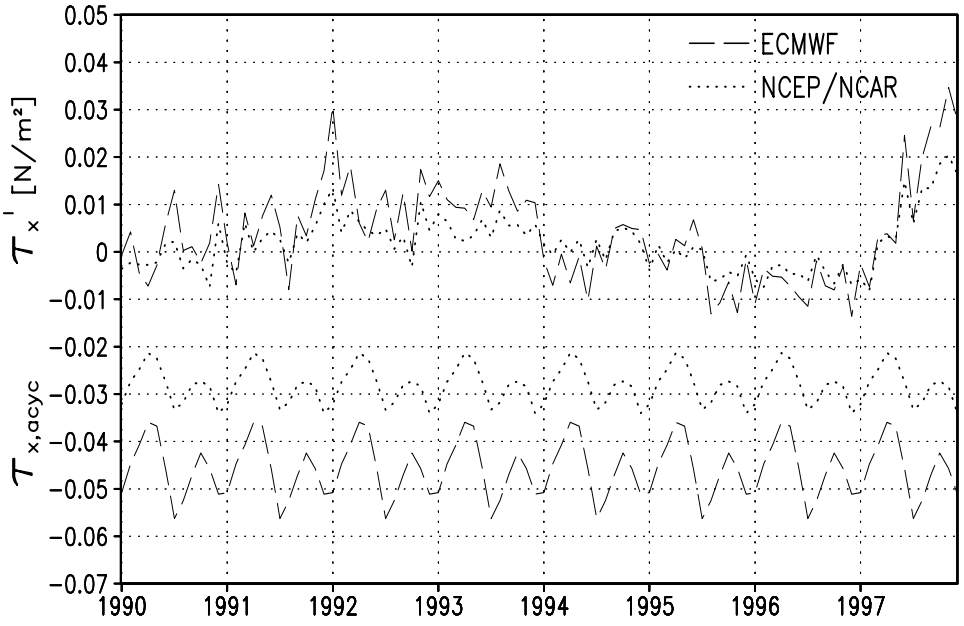

Figure 7.4: *The annual cycles and anomalies of the zonal wind stress [N/m^2] averaged over the Niño3 region of: ECMWF re-analysis (dashed) and NCEP/NCAR re-analysis (dotted).*

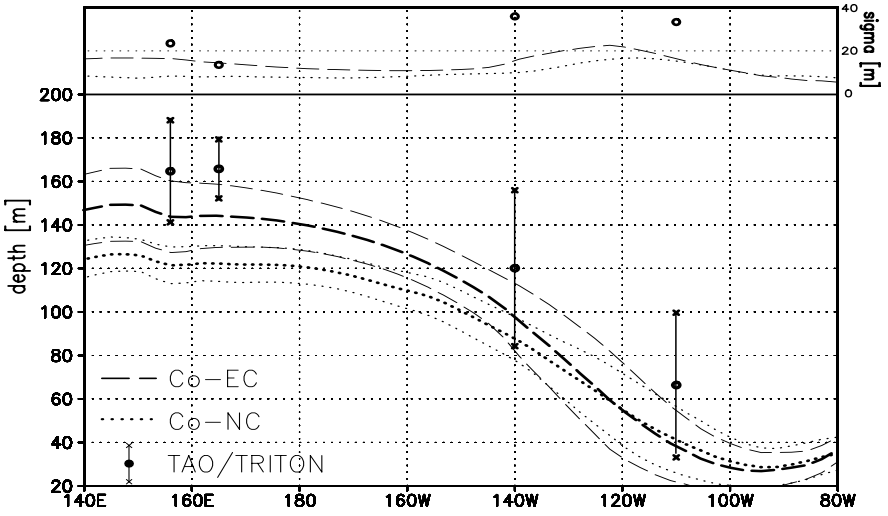

Figure 7.5: *Mean depths of the 20° C isotherm (D20) for the years 1993 to 1996 averaged over ±2° latitude (thick lines) and the corresponding standard deviations (thin lines) of: ECMWF forced run Co-EC (dashed lines), NCEP/NCAR forced run Co-NC (dotted lines) and of TAO/TRITON observations (closed and open circles with error bars of ±1 standard deviation). The standard deviations are displayed additionally in the upper part of the diagram.*

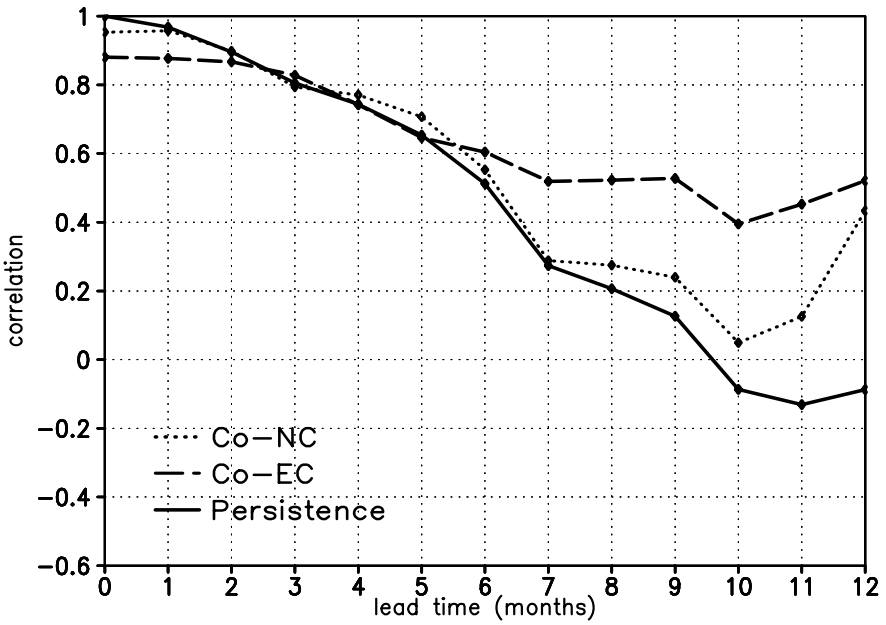

Figure 7.6: *Anomaly correlation coefficients between predicted and observed (Reynolds SST) monthly mean SSTA as an average over all forecasts started from 1993 until 1997 for both ensembles (Co-EC-fc and Co-NC-fc) and for the persistence, calculated for the Niño3 region as a function of lead time.*

In conclusion, the different atmospheric forcing fields from ECMWF and NCEP/NCAR exhibit over the largest part of the equatorial Pacific:

- different mean wind stresses - those of ECMWF being stronger
- different variabilities of wind stresses - those of ECMWF being stronger

For the uncoupled ocean simulations this results in:

- different inclinations of the thermocline - more inclined with ECMWF forcing
- different variability of thermocline - mostly more variable with ECMWF forcing

while for the forecast ensembles it results in:

- different predictive skills - with ECMWF forced initial conditions - worse for the first two months, but better for lead times beyond 6 months.

7.2 Influence of Assimilation

This section investigates the difference between experiments with and without assimilation and the difference between the two experiments with assimilation of Topex/Poseidon data. One is forced by the atmospheric fields of NCEP/NCAR (As-TP-NC, table 6.1), the other by those of ECMWF (As-TP-EC, table 6.1). In section 7.1 it has been shown that the two respective model simulations without assimilation show differences in their thermocline depths, as well as in the predictive skill for lead times of more than half a year. In this section it will be examined whether assimilation has an influence on these differences.

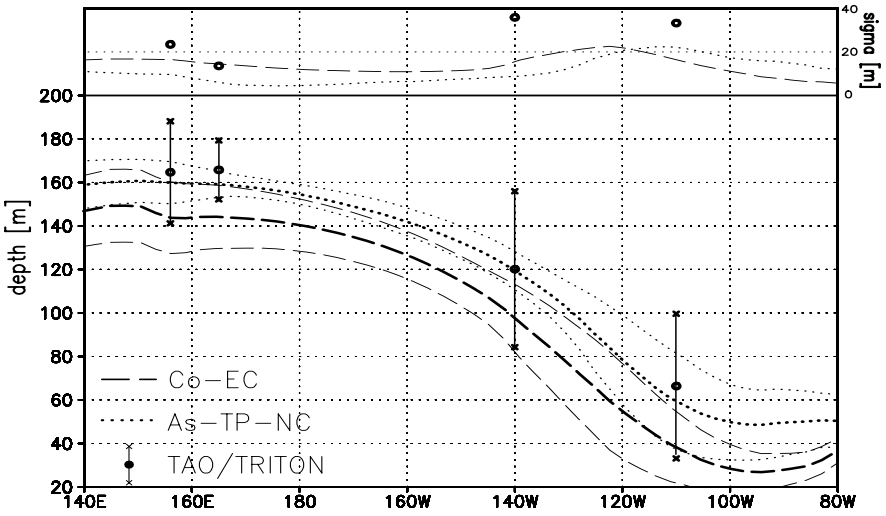

Figure 7.7: *Mean depths of the 20° C isotherm (D20) for the years 1993 to 1996 averaged over ±2° latitude (thick lines) and the corresponding standard deviations (thin lines) of: the ECMWF forced run Co-EC (dashed lines), the NCEP/NCAR forced assimilation run As-TP-NC (dotted lines) and of TAO/TRITON observations (closed and open circles with error bars of ±1 standard deviation). The standard deviations are displayed additionally in the upper part of the diagram.*

In section 7.1 it has been shown that the mean thermocline of Co-NC is up to 20 m shallower in the central-western part of the basin than that of Co-EC (indicated again in figure 7.7). This changes with assimilation. Figure 7.7 shows that the assimilation has overall deepened the thermocline. The thermocline of As-TP-NC, with NCEP/NCAR forcing, is about 10 to 20 m deeper than the thermocline of Co-EC everywhere along the equator. Although the variability is still strongly underestimated in As-TP-NC compared to the observations it has increased in the eastern part of the basin.

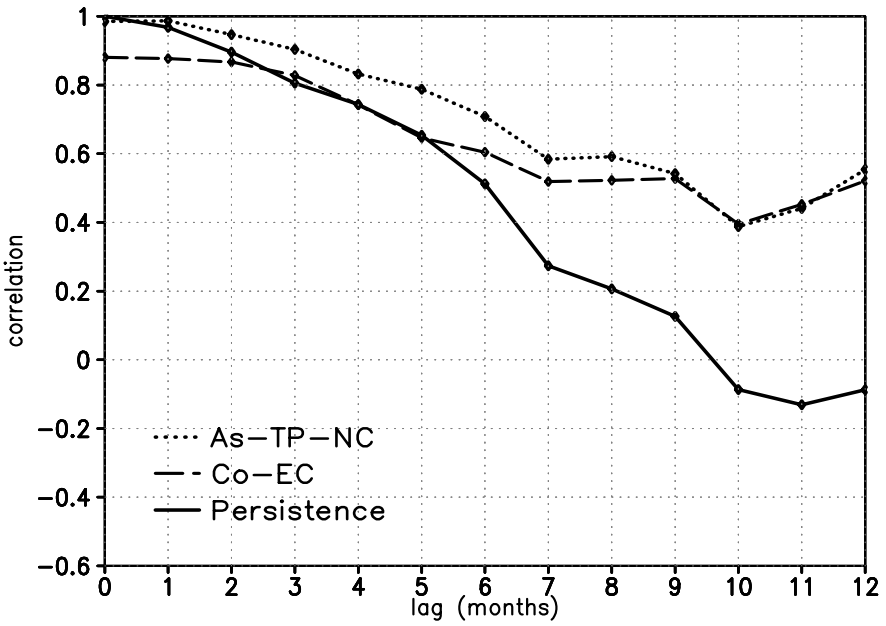

Figure 7.8: *Anomaly correlation coefficients of predicted and observed (Reynolds SST) monthly mean SSTA averaged over all forecasts started from 1993 until 1997 for the forecast ensembles Co-EC-fc, As-TP-NC-fc and for the persistence, calculated for the Niño3 region as a function of lead time.*

The predictive skills of the forecast ensembles, whose initialisation runs were just forced by atmospheric fields from different origin, showed the strongest discrepancies for lead times beyond 6 months. Assimilation improves the predictive skill of the NCEP/NCAR forced ensembles to values similar to those of Co-EC-fc at these long lead times (figure 7.8).

Figure 7.9 shows the depth of the thermocline of the NCEP/NCAR and the ECMWF forced assimilation experiments (As-TP-NC and As-TP-EC). Both, their mean thermoclines and their variabilities cannot be distinguished from each other. Thus, the assimilation of altimeter data corrects for the differences in the atmospheric forcing. These uniform mean thermocline depths are not surprising, although only T/P sea level anomalies are used for the assimilation. The reason for this is that after the projection of the SLA onto the TA, first, a temperature climatology has to be added to them and then the full temperature fields are assimilated into the model (chapter 4). Thus, the mean thermoclines of the assimilation experiments reflect this added climatology. Furthermore, the predictive skills of the forecast ensembles which were both initialized with assimilation experiments are very similar (7.10).

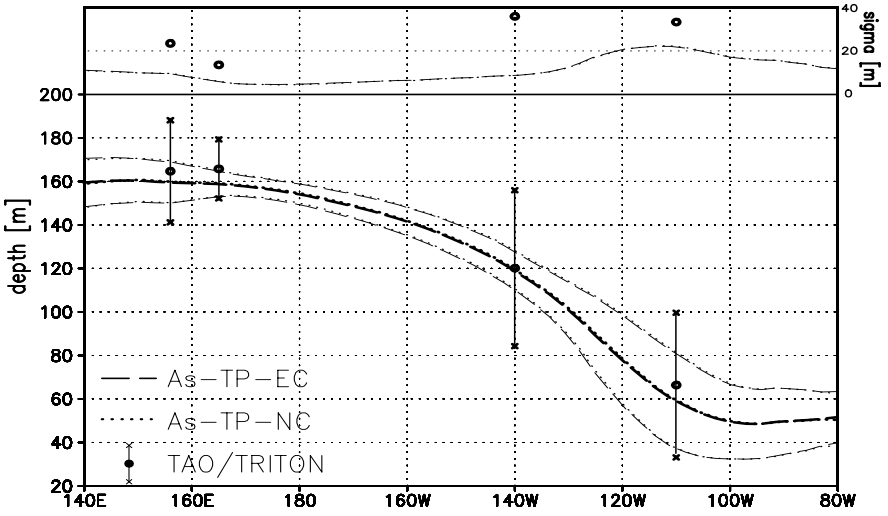

Figure 7.9: *Mean depths of the* $20^\circ C$ *isotherm (D20) for the years 1993 to 1996 averaged over* $\pm 2^\circ$ *latitude (thick lines) and the corresponding standard deviations (thin lines) of: ECMWF forced assimilation run As-TP-EC (dashed lines) and NCEP/NCAR forced assimilation run As-TP-NC (dotted lines) and of TAO/TRITON observations (closed and open circles with error bars of* ± 1 *standard deviation). The standard deviations are displayed additionally in the upper part of the diagram.*

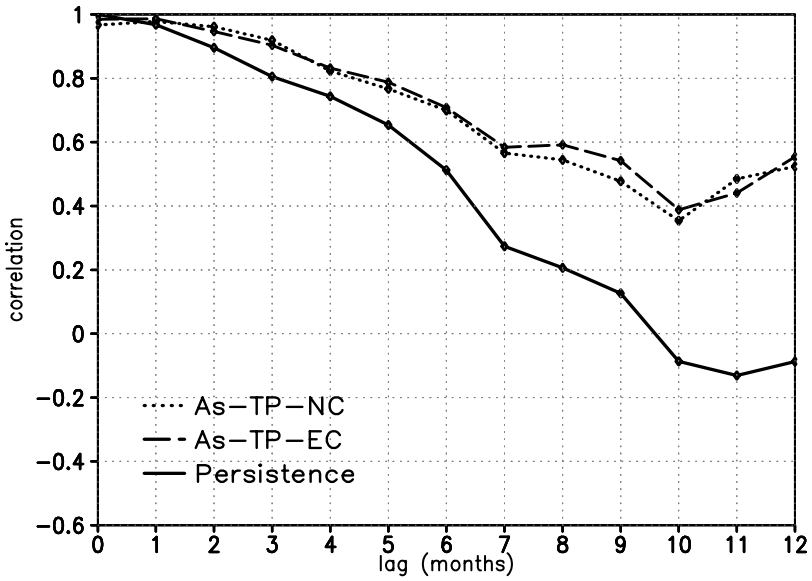

Figure 7.10: *Anomaly correlation coefficients of predicted and observed (Reynolds SST) monthly mean SSTA averaged over all forecasts started from 1993 until 1997 for the forecast ensembles As-TP-EC-fc, As-TP-NC-fc and for the persistence, calculated for the Niño3 region as a function of lead time.*

In conclusion, the results indicate that:

- assimilation of altimeter data in the way it is done within this study corrects for the differences in atmospheric forcing
- experiments with more inclined thermoclines within their initialisation runs show higher predictive skill at lead times beyond half a year

Nevertheless, the significance of the latter could not be proven on the 95% level for the time considered here. Investigations in the future with extended observational time series may shed more light on the indicated relations between forecast skill of lead times beyond 6 months and the inclination of the thermoclines within the initialisation runs.

Chapter 8

Summary, Discussion and Outlook

8.1 Summary

Topex/Poseidon (T/P) sea level anomalies (SLA) were assimilated into an ocean general circulation model, the E-HOPE, via a statistical projection onto the vertical temperature profile. The results of the assimilation were compared to those obtained by assimilating temperature data from the TAO/TRITON array. Furthermore, the impact of T/P data assimilation on the ENSO forecast skill was investigated by conducting an ensemble of forecasts with a hybrid coupled model.

The analyses have shown that the projection of T/P SLA onto the subsurface temperatures give realistic reconstructions. Assimilation of these reconstructed fields leads to an improvement of ocean initial conditions, which in turn results in improvement of the ENSO forecast skill. Thus, the SSH from the Topex/Poseidon satellite mission are valuable for ENSO forecasting and can reduce the errors from other sources like model deficiencies or errors in the atmospheric forcing.

A comparison between the impacts of T/P SLA data and TAO/TRITON in situ temperature measurements yielded no significant differences concerning their forecast skills. Regarding the seasonality of forecast skill a spring predictability barrier was found in all experiments. This is consistent with the results of other modelling studies (Kirtman et al., 2000).

Assimilation of T/P data reduced the errors of the SLA of the ocean initialisation run to half of the errors of the experiment without assimilation. Assimilation of TAO/TRITON data reduced the errors of the temperature anomalies (TA) of the ocean simulation to half of those of the experiment without assimilation. The analyses showed that some of the remaining errors are connected to strong anomalies in rainfall, which led to the conclusion that the remaining errors are mainly caused by unrealistic fresh water flux estimates.

The bivariate approach, using not only SLA but also SSTA for the projection onto the vertical temperature profile, led to improved thermal stratification in the central equatorial Pacific and to improved equatorial SSTA. However, the bivariate approach did not yield any significant difference with respect to the ENSO forecast skill of the univariate case with assimilation of SLA only.

The comparison of ECMWF and NCEP/NCAR atmospheric forcing fields showed that the zonal wind stresses of ECMWF are stronger and more variable over most of the equatorial Pacific. These differences might have induced a stronger inclination and a higher variability of the thermocline over most of the equatorial Pacific in the experiment forced by ECMWF fields. Regarding the forecast skill, the ECMWF experiments exhibit a lower predictive skill than the NCEP/NCAR experiments at short lead times (the first two months), similar predictive skill for medium range lead times (between 3 and 6 months), but a better predictive skill for long lead times (beyond 6 months). This comparison illustrated that if no data assimilation is applied, the choice of the atmospheric forcing considerably influences the ocean analyses and coupled model ENSO forecasts. The comparison also shows that the differences due to these different atmospheric forcing fields vanish with the assimilation of T/P data, which confirms that assimilation can correct for errors in the atmospheric forcing.

8.2 Discussion

Skill scores (the RMS error and the anomaly correlation coefficient (ACC)) have been calculated for the comparison between forecasts with and without assimilation of the different data types and for the sensitivity to the bivariate data assimilation. For lead times longer than one month both, the RMS as well as the ACC skill scores, showed constantly better

values for the forecast ensembles initialised from assimilation runs than either persistence or the forecast ensembles initialised from the control run. As both ENSO forecast skill measures showed the same results, these results appear to be robust and are thus believed, although the significance test of the differences in the RMS error did not support this for all lead times. Proofed significance of the differences of the forecast skills for all lead times might be achieved with larger ensembles.

The comparison of both assimilation experiments, assimilating either T/P SLA or TAO/-TRITON in situ temperature measurements, showed no significant differences in ENSO forecast skill. However, this does not lead to the conclusion that in situ temperature measurements and the T/P satellite measurements are redundant. For small-scale processes as well as verification of model results both are indispensable.

Although the T/P measurements are of unprecedented accuracy (Fu et al., 1994), sea level topographies still contain one large source of uncertainty, the exact geoid. To circumvent these errors, calculation of the sea level deviations (SLD) relative to an estimation of the mean sea level height is common (AVISO, 1998b). Thus, the assimilation of sea level concentrates on either assimilation of sea level deviations relative to a reference period (e.g. Segschneider et al., 1999) or anomalies relative to a reference annual cycle.

The assimilation scheme used here requires an estimation of the climatological annual cycle of three dimensional temperature as well as an estimation of the statistical relation between SLA and the PCs of the vertical EOFs of TA(z). The climatological annual cycle together with the statistics for the assimilation scheme were derived from a former uncoupled ocean model simulation. This model simulation had to cover more than the three reference years to allow reliable statistical derivations for the assimilation scheme. The assimilation scheme uses the annual cycle as a reference cycle and therefore the annual cycle had to be taken from the same simulation. This implies that the assimilation forces the model towards a mean state from another period. However, an improvement of the ENSO forecast skill seems to depend mostly on a reasonable representation of the subsurface temperature anomalies (Latif and Graham, 1992). Therefore an assimilation method based on anomalies as it is used here should be adequate. Improvements of the mean state may lead to a further increase of ENSO forecast skill, as the comparison of different forcings in chapter 7 indicated for lead times beyond half a year.

The results suggest that the errors, which despite assimilation still remain in the ocean analyses are mainly related to the fresh water flux (PME). On the one hand, these errors are induced by the indirect estimation of PME for the ocean simulations and are thus visible in the SLA error of the TAO/TRITON experiment. On the other hand, heavy rainfall varies the salinity of the upper ocean layer and has thus an influence on the sea level. This is a portion of the SLA signal, which is not considered by the assimilation scheme. Errors related to the fresh water flux are thus additionally introduced by the projection of the SLA signal onto the thermal structures only. However, other studies, which have considered PME forcing fields from re-analyses and use other assimilation schemes, show errors of comparable sizes (Ji et al., 2000; Segschneider et al., 2000a). Furthermore, estimations of the fresh water flux over the oceans have large uncertainties (WCRP, 2000) and even fresh water fluxes from re-analyses might lead to inconsistencies in ocean analyses. Nevertheless, also subsurface salinity variations may have an additional effect on the SLA and further investigations are needed to separate the surface and subsurface salinity effects.

Therefore, at least one of the two variables, i.e. SSS or PME should be available and considered for correct SLA assimilation in the western tropical Pacific. SSS are not yet available continuously in time and space. But it is under development to recover natural microwave emissions of the ocean which are a function of SSS and temperature to estimate SSS continuously (Koblinsky, 1998; Le Vine et al., 2000). PME on the other hand seems already to be roughly estimable as the depicted products of Xie and Arkin (1997) and Graßl et al. (2000) have shown in chapter 5.1. These two datasets, however, show large differences and, as stated above, include large uncertainties. Contributions for a further enhancement of the accuracy of rainfall estimates in the future might be derived from rainfall estimates of the Topex/Poseidon satellite (Quartly et al., 1999).

One sensitivity study was looking at the differences between ECMWF and NCEP/NCAR wind stresses and their influences on the results. Daily equatorial ECMWF wind stresses were stronger and more variable than those of NCEP/NCAR for the period 1993-96. This is consistent with findings from other studies, e.g. from Smull and McPhaden (1998), who investigated annual mean surface winds for the period between 1991-93, and of the WCRP (2000) in which climatological mean zonal surface stresses were compared for the period 1981-92. Kessler (1996) analysed surface winds as regional averages over tropical boxes from 1982-95 and found that the zonal wind of NCEP/NCAR re-analysis is on the

contrary sometimes even stronger than ECMWF re-analysis. It is concluded here that large uncertainties exist in the estimation of the surface wind stresses and that these uncertainties reflect themselves in uncertainties of the ocean state estimation.

8.3 Outlook

It has been shown that the assimilation of T/P SLA led to an improvement of the simulated SLA, which was connected with a more realistic simulation of the upper ocean thermal field. The results further suggest that the remaining error in the simulation of SLA is mostly related to surface fresh water fluxes. In particular, high rainfall seems to play a major role of the sea level signal, especially in the western tropical Pacific. Thus investigations of the fraction to which anomalous rainfall contributes to the signal of SLA are needed to be realised in the future.

The assimilation scheme, used in this study, might be enlarged to also account for the fresh water fluxes. This could be done with a multivariate projection, projecting PME as well as SLA onto SSS and TA(z). The remaining errors of the ocean simulations related to the fresh water fluxes might be overcome by this extension. Furthermore, it would yield an implicit estimation of the fraction to which anomalous rainfall contributes to the signal of SLA. However, an uncoupled ocean model simulation driven by realistic PME forcing would be needed for the statistics of this extended assimilation scheme. As mentioned above, estimations of the fresh water flux over the oceans still have large uncertainties. Therefore increased efforts to estimate precipitation and evaporation over the oceans would be useful to yield the best possible results for the assimilation of sea level.

Soon, measurements of sea level with the T/P satellite will cover 10 years of data. Furthermore, the follow-on spacecraft of the T/P satellite, Jason-1, has recently been launched and both together with the ERS-satellites give rise to the hope of a further extended period of sea level data with high accuracies. Such an extended period of data will allow larger number of forecasts and thus better statistical estimates. Thus, the significance of the impact of T/P data assimilation on the ENSO forecast skill might be proven more rigorously. In addition, such an extended period might also help to shed more light on the relation between the inclination of the thermocline and the predictability for lead times of

more than half a year.

Several ENSO forecasts are published operationally. They can, for example, be found on the Internet at the following address: *"http://iri.ucsd.edu/hot_nino/sst_fcst"*. One of these models is run at the Scripps Institution of Oceanography in La Jolla, California. It consists of an older version of the E-HOPE model than the one used here and is also coupled to a statistical atmosphere. The current forecasts of that coupled model can be followed at: *"http://meteora.ucsd.edu/~pierce/elnino/elnino.html"*. In the future, the assimilation module developed for the T/P data in this study might be integrated into that model version and might thus lead to improved ocean initial conditions and improved ENSO forecasts of that model as well. A method to calculate T/P SLD in near real time has already been developed and allows the use of T/P SLD with a time delay of 2-3 days. This enables the sea level data to be applied not only for studies of the past but also for a look into the future by means of operational forecasts including sea level data assimilation.

Currently, a new EU project has just been started, to investigate "enhanced ocean data assimilation and climate prediction" (ENACT) with more complex assimilation schemes like the adjoint method and the Kalman filter. The results of this work here will provide information about details, which have to be considered for these future studies and will help to interpret their results.

Danksagung (Acknowledgements)

Zu guter Letzt möchte ich mich bei allen Kollegen und Freunden bedanken, die mir während der Arbeit an meiner Dissertation geholfen haben und mich unterstützt haben.

Insbesondere möchte ich meinem Betreuer, Mojib Latif, danken für das Ermöglichen der lehrreichen Jahre auf dem spannenden Forschungsgebiet rund um El Niño/Southern Oscillation, die ich in seiner Arbeitsgruppe am MPI verbringen konnte. Desweiteren möchte ich ihm für seine hilfreichen Ratschläge danken. Herrn Prof. W. Alpers danke ich für die Begutachtung der Arbeit, sowie die ersten Impulse zu dieser Doktorarbeit, die ich bei meiner Diplomarbeit in seiner Arbeitsgruppe über den Bezug der Satellitenaltimetrie zum ENSO Phänomen sammeln konnte.

Jochen Segschneider danke ich herzlich für die Anregung zu kulinarischen Genüssen als Ausgleich zur Arbeit, sowie die Möglichkeit der intensiven Diskussion mit der Arbeitsgruppe für saisonale Vorhersagen am ECMWF in Großbritannien. Ihm - wie auch Saskia Esselborn, Simon Marsland und Noel Keenlyside - möchte ich außerdem danken für die vielen Hinweise beim Korrekturlesen von Manuskripten dieser Arbeit. Allen meinen Kollegen, insbesondere aber Ute Merkel, danke ich für die nette Arbeitsatmosphäre, ein stets offenes Ohr und die zahlreichen Diskussionen, von denen ich viel profitieren konnte.

Bedanken möchte ich mich auch für die aufmunternden "Nicht Übertreiben"-Ratschläge meines Flurnachbarn Ernst Maier-Reimer, ohne die ich wohl manchmal den Weg nicht rechtzeitig nach Hause gefunden hätte.

Die Altimeterdaten stellte die Space Oceanography Division der Firma Collecte Localisation Satellites in Toulouse, Frankreich im Rahmen des EU-Projektes DUACS (ENV4-CT96-0357) zur Verfügung. NCEP/NCAR, Boulder, Colorado lieferte einen Satz Antriebsdaten. Magdalena Balmaseda vom ECMWF, Großbritannien danke ich für die Bereitstellung der ECMWF-Antriebsdaten, sowie Stefan Hagemann für die Niederschlags- und Verdunstungs-Datensätze.

Aber mein größter Dank gilt meinen Eltern und Axel.

List of Acronyms

ACC	Anomaly Correlation Coefficient
ADCP	Acoustic Doppler Current Profiler
CLIVAR	Climate Variability and Predictability
CLS	Collecte Localisation Satellites (company in Toulouse, France)
CNES	Centre National d'Études Spatiales
CORSSH	Corrected Sea Surface Heights
DORIS	Détermination d'Orbite et Radiopositionnement Intégrés par Satellite
D20	Depth of the 20°C Isotherm
ENSO	El Niño Southern Oscillation
EOF	Empirical Orthogonal Function
GCOS	Global Climate Observing System
GISST	Global sea-Ice and Sea Surface Temperatures
GOOS	Global Ocean Observing System
GPS	Global Positioning System
HCM	Hybrid Coupled Model
HH	Historical Homogeneous
HOPE	Hamburg Ocean Primitive Equation model
JAMSTEC	Japan Marine Science and Technology Center
NASA	National Aeronautics and Space Administration
NCEP	National Centers for Environmental Prediction
NCAR	National Center for Atmospheric Research
NRT	Near Real Time
NWP	Numerical Weather Prediction
OGCM	Ocean General Circulation Model

PME	Precipitation minus evaporation
PMEL	Pacific Marine Environmental Laboratory
SLA	Sea Level Anomaly/ies
SLD	Sea Level Deviations
SSH	Sea Surface Heights
SSS	Sea Surface Salinity
SST	Sea Surface Temperature
SSTA	Sea Surface Temperature Anomaly/ies
TA	Temperature Anomaly/ies
TAO	Tropical Atmosphere Ocean
TOGA	Tropical Ocean Global Atmosphere
TRITON	Triangle Trans Ocean Buoy Network
XBT	Expendable Bathythermographs

Bibliography

Arakawa, A. and V. R. Lamb (1977). "Computational Design of the Basic Dynamical Processes of the UCLA General Circulation Model." *Meth. Comput. Phys.*, 17: 173–265.

AVISO (1996). "AVISO User Handbook: Merged TOPEX/POSEIDON Products, AVI-NT-02-101-CN, Ed. 3.0." Tech. rep., CLS Space Oceanography Division, Toulouse, France.

AVISO (1998a). "AVISO User Handbook: Corrected Sea Surface Heights, AVI-NT-011-311-CN, Ed. 3.1." Tech. rep., CLS Space Oceanography Division, Toulouse, France.

AVISO (1998b). "AVISO User Handbook: Sea Level Anomalies, AVI-NT-011-312-CN, Ed. 3.1." Tech. rep., CLS Space Oceanography Division, Toulouse, France.

AVISO (1999). "AVISO/CALVAL Yearly Report: 6 Years of TOPEX/POSEIDON data (GDR-Ms), AVI-NT-011-316-CN, Ed. 1.0." Tech. rep., CLS Space Oceanography Division, Toulouse, France.

AVISO (2001). "AVISO/CALVAL Yearly Report: 8 Years of TOPEX/POSEIDON data (GDR-Ms) - Synthesis Validation Report -, SMM-NT-M5-EA-12962-CN, Ed. 1.0." Tech. rep., CLS Space Oceanography Division, Toulouse, France.

Barnett, T., M. Latif, N. Graham, M. Flügel, S. Pazan, and W. White (1993). "ENSO and ENSO-related predictability. Part I: Prediction of equatorial Pacific sea surface temperature with a hybrid coupled ocean-atmosphere model." *J. Climate*, 6: 1545–1566.

Bergthorsson, P. and B. Doos (1955). "Numerical weather map analysis." *Tellus*, 7: 329–340.

Carton, J. A., B. S. Giese, X. Cao, and L. Miller (1996). "Impact of altimeter, thermistor, and expendable bathythermograph data on retrospective analyses of the tropical Pacific Ocean." *J. Geophys. Res.*, 101(C6): 14,147–14,159.

Chambers, D. P., B. D. Tapley, and R. H. Stewart (1998). "Measuring heat storage changes in the equatorial Pacific: a comparison between TOPEX altimetry and Tropical Atmosphere-Ocean buoys." *J. Geophys. Res.*, 103(C9): 18,591–18,597.

Conover, W. (1980). Practical Nonparametric Statistics. John Wiley & Sons, New York, USA.

Cooper, M. and K. Haines (1996). "Altimetric assimilation with water property conservation." *J. Geophys. Res.*, 101(C1): 1059–1077.

Daley, R. (1991). Atmospheric Data Analysis. Cambridge University Press, 457 pp.

DKRZ, D.-M. U. S. G. (October 1992). "ECHAM3 - Atmospheric General Circulation Model." DKRZ-Reports 6, DKRZ, Hamburg, Germany.

Eckert, C. and M. Latif (1997). "Predictability of a Stochastically Forced Hybrid Coupled Model of El Niño." *J. Climate*, 10: 1488–1504.

Esselborn, S. (2001). "Meereshöhen und ozeanische Zirkulation im Nordatlantik zwischen 1992 und 1998." Ph.D. thesis, Universität Hamburg, Germany.

Fischer, M. (1996). "Der Einfluß von Datenassimilation auf ENSO Simulationen und Vorhersagen." Ph.D. thesis, Universität Hamburg, Germany.

Fischer, M. (2000). "Multivariate projection of surface data onto subsurface sections." *Geophys. Res. Lett.*, 27(6): 755–757.

Fischer, M. and M. Latif (1995). "Assimilation of temperature and sea level observations into a primitive equation model of the tropical Pacific." *J. Mar. Sys.*, 6: 31–46.

Fischer, M., M. Latif, M. Flügel, and M. Ji (1997). "The Impact of Data Assimilation on ENSO Simulations and Predictions." *Mon. Wea. Rev.*, 125(5): 819–830.

Fu, L. L., E. J. Christensen, J. Yamarone, C. A., M. Lefebvre, Y. Menard, M. Dorrer, and P. Escudier (1994). "TOPEX/POSEIDON mission overview." *J. Geophys. Res.*, 99: 24,369–24,381.

Gavart, M. and P. De Mey (1997). "Isopycnal EOFs in the Azores Current region: a statistical tool for dynamical analysis and data assimilation." *J. Phys. Oceanogr.*, 27(10): 2146–2157.

Gibson, J. K., P. Kållberg, S. Uppala, A. Hernandez, A. Nomura, and E. Serrano (1999). "ECMWF Re-Analysis Project Report Series - 1. ERA-15 Description, Version 2." Tech. rep., ECMWF, Reading, England.

Goswami, B. and J. Shukla (1991). "Predictability of a coupled ocean-atmosphere model." *J. Climate*, 4(1): 3–22.

Graßl, H., V. Jost, R. Kumar, J. Schulz, P. Bauer, and P. Schlüssel (November 2000). "The Hamburg Ocean-Atmosphere Parameters and Fluxes from Satellite Data (HOAPS): A Climatological Atlas of Satellite-Derived Air-Sea-Interaction Parameters over the Oceans." MPI Reports 312, MPI for Meteorology, Hamburg, Germany.

Hasselmann, K. (1976). "Stochastic climate models, Pt. 1, Theory." *Tellus*, 26(6): 473–485.

Ji, M., R. W. Reynolds, and D. W. Behringer (2000). "Use of TOPEX/POSEIDON sea level data for ocean analyses and ENSO prediction: some early results." *J. Climate*, 13(1): 216–231.

Kalnay, E., M. Kanamitsu, R. Kistler, W. Collins, D. Deaven, L. Gandin, M. Iredell, S. Saha, G. White, J. Woollen, Y. Zhu, M. Chelliah, W. Ebisuzaki, W. Higgins, J. Janowiak, K. C. Mo, C. Ropelewski, J. Wang, A. Leetmaa, R. Reynolds, R. Jenne, and D. Joseph (1996). "The NCEP/NCAR 40-year reanalysis project." *Bull. Amer. Meteorol. Soc.*, 77(3): 437–471.

Katz, E., A. J. Busalacchi, M. Bushnell, F. I. Gonzalez, L. Gourdeau, M. J. McPhaden, and J. Picaut (1995). "A comparison of coincidental time series of the ocean surface height by satellite altimeter, mooring, and inverted echo sounder." *J. Geophys. Res.*, 100(C12): 25,101–25,108.

Kessler, W. (1996). "Estimation of Wind Variability in the Tropical Pacific." In: "Assessment of the Pacific Observing System for Analyses, Model-Testing and El Niño Forecasts," Report of the CLIVAR upper ocean panel, The International Research Programme on Climate Variability and Predictability (CLIVAR), pp. 25–35.

Kessler, W. S., M. C. Spillane, M. J. McPhaden, and D. E. Harrison (1996). "Scales of variability in the equatorial Pacific inferred from the Tropical Atmosphere-Ocean Buoy Array." *J. Climate*, 9(12 Part I): 2999–3024.

Kirtman, B. P., J. Shukla, M. Balmaseda, N. Graham, C. Penland, Y. Xue, and S. Zebiak (October 2000). "Current Status of ENSO Forecast Skill, A Report to CLIVAR NEG." Report, Climate Variability and Predictability (CLIVAR) Numerical Experimentation Group (NEG).

Koblinsky, C. (1998). "Sea Surface Salinity from Space." In: "CLIVAR Upper Ocean Panel (Third Session)," Report of the CLIVAR upper ocean panel, The International Research Programme on Climate Variability and Predictability (CLIVAR).

Latif, M., D. Anderson, T. Barnett, M. Cane, R. Kleeman, A. Leetmaa, J. O'Brien, A. Rosati, and E. Schneider (1998). "A review of the predictability and prediction of ENSO." *J. Geophys. Res.*, 103(C7): 14,375–14,393.

Latif, M. and M. Flügel (1991). "An investigation of short-range climate predictability in the tropical Pacific." *J. Geophys. Res.*, 96(C2): 2661–2673.

Latif, M. and N. E. Graham (1992). "How much predictive skill is contained in the thermal structure of an oceanic GCM?" *J. Phys. Oceanogr.*, 22(8): 951–962.

Le Traon, P., F. Nadal, and N. Ducet (1998). "An Improved Mapping Method of Multi-satellite Altimeter Data." *J. Atmos. Ocean. Technol.*, 15: 522–534.

Le Vine, D. M., J. B. Zaitzeff, E. J. D'Sa, J. L. Miller, C. Swift, and M. Goodberlet (2000). "Sea surface salinity: Toward an operational remote-sensing system." In: "Satellites, Oceanography and Society," No. 63 in Elsevier Oceanography Series, chap. 19, Elsevier Science B.V., P.O.Box 211, 1000 AE Amsterdam, The Netherlands, pp. 321–335.

Levitus, S. (1982). "Climatological Atlas of the Worlds Ocean." Prof. paper 13, NOAA, US Govt. printing office, Washington D.C., 173pp.

Levitus, S., R. Burgett, and T. P. Boyer (1994). "World Ocean Atlas 1994, Volume 3: Salinity." Noaa atlas nesdis, NODC, NOAA/NESDIS, E/OC21, Washington D.C., 20335 USA, 97pp.

Lorenz, E. N. (1956). "Empirical orthogonal functions and statistical weather prediction." Statistical Forecast Project Report 1, MIT, Dept. of Meteor., MIT, Boston, 49pp.

McPhaden, M. J. (1999). "Genesis and Evolution of the 1997-98 EL Niño." *Science*, 283: 950–954.

McPhaden, M. J., A. J. Busalacchi, R. Cheney, K. S. Gage, D. Halpern, M. Ji, P. Julian, G. Meyers, G. T. Mitchum, P. P. Niiler, J. Picaut, R. W. Reynolds, N. Smith, and K. Takeuchi (1998). "The Tropical Ocean-Global Atmosphere observing system: A decade of progress." *J. Geophys. Res.*, 103(C7): 14,169–14,240.

Mellor, G. L. and T. Ezer (1991). "A Gulf Stream model and an altimetry assimilation scheme." *J. Geophys. Res.*, 96: 8779–8795.

Meyers, G., H. Phillips, N. Smith, and J. Sprintall (1991). "Space and time scales for optimal interpolation of temperature - Tropical Pacific Ocean." *Prog. Oceanog.*, 28: 189–218.

Neelin, J. D., D. S. Battisti, A. C. Hirst, F.-F. Jin, Y. Wakata, T. Yamagata, and S. E. Zebiak (1998). "ENSO theory." *J. Geophys. Res.*, 103(C7): 14,261–14,290.

van Oldenborgh, G. J., G. Burgers, S. Venzke, C. Eckert, and R. Giering (1999). "Tracking down the ENSO delayed oscillator with an adjoint OGCM." *Mon. Wea. Rev.*, 127(7): 1477–1495.

Oschlies, A. and J. Willebrand (1996). "Assimilation of GEOSAT altimeter data into an eddy-resolving primitive equation model of the North Atlantic Ocean." *J. Geophys. Res.*, 101(C6): 14,175–14,190.

Parker, D. E., C. K. Folland, M. N. Ward, M. Jackson, and K. Maskell (1995). "Marine surface data for analysis of climate fluctuations of interannual to century timescales." In: Martinson, D. G. e. a. (ed.), "Natural Climate Variability on Decadal to Century Time scales," National Research Council, National Academy Press, Washington, pp. 241–250.

Perigaud, C. M., C. Cassou, B. Dewitte, L. L. Fu, and J. D. Neelin (2000). "Using data and intermediate coupled models for seasonal-to-interannual forecasts." *Mon. Wea. Rev.*, 128(9): 3025–3049.

Philander, S. G. (1990). El Niño, La Niña, and the Southern Oscillation. Academic Press, 1250 Sixth Avenue, San Diego, California 92101, USA.

Picaut, J., A. J. Busalacchi, M. J. McPhaden, L. Gourdeau, F. I. Gonzalez, and E. C. Hackert (1995). "Open-ocean validation of TOPEX/POSEIDON sea level in the western equatorial Pacific." *J. Geophys. Res.*, 100(C12): 25,109–25,127.

Press, W. H., B. Flannery, S. Teukolsky, and W. Vetterling (1988). Numerical Recipies. Cambridge University Press, 735 pp.

Quartly, G. D., M. A. Srokosz, and T. H. Guymer (1999). "Global precipitation statistics from dual-frequency TOPEX altimetry." *J. Geophys. Res.*, 104(D24): 31,489–31,516.

Reynolds, R. W. and T. M. Smith (1994). "Improved Global Sea Surface Temperature Analysis Using Optimum Interpolation." *J. Climate*, 7(C7): 929–948.

Rienecker, M. M. and D. Adamec (1995). "Assimilation of altimeter data into a quasi-geostrophic ocean model using optimal interpolation and eofs." *J. Mar. Sys.*, 6: 125–143.

Roeckner, E., K. Arpe, L. Bengtsson, S. Brinkop, L. Dümenil, M. Esch, E. Kirk, F. Lunkeit, M. Ponater, B. Rockel, R. Sausen, U. Schleese, S. Schubert, and M. Windelband (October 1992). "Simulation of the present-day climate with the ECHAM model: Impact of model physics and resolution." MPI Reports 93, MPI for Meteorology, Hamburg, Germany.

Rothstein, L. M., D. L. T. Anderson, E. S. Sarachik, and P. J. Webster (eds.) (June 1998). The TOGA Decade, vol. 103, C7 of *J. Geophys. Res. special issue*. American Geophysical Union.

Schöttle, S. (1997). "Untersuchungen über die Meereshöhenvariabilität in den tropischen Ozeanen von 1992 bis 1995 unter Verwendung von Radar-Altimeterdaten des TOPEX/POSEIDON-Satelliten." Diploma thesis, institut für Meereskunde der Universität Hamburg, Germany.

Schöttle, S. and M. Latif (2000). "Assimilation of Topex/Poseidon data improves ENSO hindcast skill." *CLIVAR Newsletter Exchanges*, 5(3): 8–10.

Segschneider, J., J. Alves, D. L. T. Anderson, M. Balmaseda, and T. N. Stockdale (1999). "Assimilation of Topex/Poseidon Data into a Seasonal Forecast System." *Phys. Chem. Earth*, 24(4): 369–374.

Segschneider, J., D. L. T. Anderson, and T. N. Stockdale (September 2000a). "Towards the use of altimetry for operational seasonal forecasting." *J. Climate*, 13(17): 3115–3138.

Segschneider, J., D. L. T. Anderson, J. Vialard, M. Balmaseda, T. N. Stockdale, A. Troccoli, and K. Haines (December 2000b). "Initialization of seasonal forecasts assimilating sea level and temperature observations." Technical Memorandum 320, European Centre for Medium-Range Weather Forecasts (ECMWF), Reading, England.

Shum, C. K., J. C. Ries, and B. D. Tapley (1995). "The accuracy and applications of satellite altimetry." *Geophys. J. Int.*, 121: 321–336.

da Silva, A. M., C. C. Young-Molling, and S. Levitus (1994). "Atlas of Surface Marine Data 1994, Volume 1: Algorithms and Procedures." NOAA Atlas NESDIS 6, NODC, NOAA/NESDIS, E/OC21, Washington D.C., 20335 USA.

Smull, B. F. and M. J. McPhaden (1998). "Comparison of NCEP/NCAR and ECMWF reanalysed fields with TOGA TAO buoy observations over the tropical Pacific." In: "Proceedings of the 1st WCRP Intl. Conf. on Reanalyses, WCRP-104, WMO/TD 876," WMO, Geneva, pp. 227–230.

Sprintall, J. and G. Meyers (1991). "An optimal XBT sampling network for the eastern Pacific Ocean." *J. Geophys. Res.*, 96(C6): 10,539–10,552.

Stammer, D. and C. Wunsch (1996). "The determination of the large-scale circulation of the Pacific Ocean from satellite altimetry using model Green's functions." *J. Geophys. Res.*, 101(C8): 18,409–18,432.

Stockdale, T. N., A. J. Busalacchi, D. E. Harrison, and R. Seager (1998). "Ocean modeling for ENSO." *J. Geophys. Res.*, 103(C7): 14,325–14,355.

Trenberth, K. E., G. W. Branstator, D. Karoly, A. Kumar, N.-C. Lau, and C. Ropelewski (1998). "Progress during TOGA in understanding and modeling global teleconnections associated with tropical sea surface temperatures." *J. Geophys. Res.*, 103(C7): 14,291–14,324.

Troccoli, A. and K. Haines (1999). "Use of the temperature-salinity relation in a data assimilation context." *J. Atmos. Ocean. Technol.*, 16(12): 2011–2025.

UNESCO (1983). "Algorithms for the computation of fundamental properties of seawater." Tech. Rep. 44, UNESCO Technical Papers in Marine Science.

Vialard, J. and P. Delecluse (1998). "An OGCM Study for the TOGA Decade. Part I: Role of Salinity in the Physics of the Western Pacific Fresh Pool." *J. Phys. Oceanogr.*, 28(6): 1071–1088.

WCRP (November 2000). "Final report of the Joint WCRP/SCOR Working Group on Air-Sea Fluxes." WMO/TD - No. 136 112, WCRP, editor: Taylor, P.K.

White, W. B., S. E. Pazan, and M. Inoue (1987). "Hindcast/forecast of ENSO events based upon the redistribution of observed and model heat content in the western Tropical Pacific, 1964-86." *J. Phys. Oceanogr.*, 17(2): 264–280.

Wolff, J.-O., E. Maier-Reimer, and S. Legutke (April 1997). "The Hamburg Ocean Primitive Equation Model." Technical Report 13, DKRZ, Hamburg, Germany.

Wright, B. (1988). "Correlation structure of the El Nino/Southern Oscillation phenomenon." *J. Climate*, 1(6): 609–625.

Wyrtki, K. (1975). "Fluctuations of the dynamic topography in the Pacific Ocean." *J. Phys. Oceanogr.*, 5: 450–459.

Xie, P. and P. A. Arkin (1997). "Global precipitation: a 17-year monthly analysis based on gauge observations, satellite estimates, and numerical model outputs." *Bull. Amer. Meteorol. Soc.*, 78(11): 2539–2558.

MPI-Examensarbeit-Referenz:

Examensarbeit Nr. 1-67 bei Bedarf bitte Anfragen:
MPI für Meteorologie, Abtlg.: PR, Bundesstr. 55, 20146 Hamburg

Examensarbeit Nr. 68 Februar 2000	**Die direkte Strahlungswirkung von Aerosolteilchen auf ein Klimamodell** Anke Maria Allner
Examensarbeit Nr. 69 Februar 2000	**Räumliche und zeitliche Variabilität von Wasserisotopen im polaren Niederschlag** (Spatial and Temporal Variability of Water Isotopes in Polar Precipitation) Martin Werner
Examensarbeit Nr. 70 März 2000	**Bestimmung des turbulenten Impulsflusses mit Hilfe von Doppler- und Interferometriemessungen eines Radar-RASS-Systems** Lutz Hirsch
Examensarbeit Nr. 71 Mai 2000	**Entwicklung und Test eines massenerhaltenden semi-Lagrangschen Transportverfahrens auf einer Kugel** Markus Peter Olk
Examensarbeit Nr. 72 Mai 2000	**Quantification of Natural Climate Variability in Paleoclimatic Proxy Data Using General Circulation Models: Application to Glacier Systems** Bernhard K. Reichert
Examensarbeit Nr. 73 Mai 2000	**Validation of Clouds in the ECHAM4 Model Using a Dynamical Adjustment Technique** Hans-Stefan Bauer
Examensarbeit Nr. 74 Juni 2000	**The Dynamical Link Between the Troposphere and Stratosphere and its Potential to Affect Climate** Judith Perlwitz
Examensarbeit Nr. 75 Juli 2000	**Fernerkundung von Eis- und Mehrschichtbewölkung über Meeresuntergrund aus Messungen rückgestreuter Solarstrahlung** Claudio Costanzo
Examensarbeit Nr. 76 Juli 2000	**Large-scale SST variability in the midlatitudes and in the tropical Atlantic** Dietmar Dommenget
Examensarbeit Nr. 77 Juli 2000	**HOAPS: Eine neue Klimatologie des Süßwasserflusses an der Meeresoberfläche abgeleitet aus Satellitendaten** Volker Jost
Examensarbeit Nr. 78 September 2000	**The potential influence of natural climate variability and uncertainty in the design of optimal greenhouse gas emission policies** Victor Ocaña

MPI-Examensarbeit-Referenz:

Examensarbeit Nr. 1-67 bei Bedarf bitte Anfragen:
MPI für Meteorologie, Abtlg.: PR, Bundesstr. 55, 20146 Hamburg

Examensarbeit Nr. 79 Oktober 2000	**Messungen des Reflexionsvermögen der Meeresober-fläche im infraroten Spektralbereich mit dem "Ocean Atmosphere Sounding Interferometer System" (OASIS)** Lars Fiedler
Examensarbeit Nr. 80 November 2000	**Vertikalmessungen der Aerosolextinktion und des Ozons mit einem UV-Raman-Lidar** Volker Matthias
Examensarbeit Nr. 81 Dezember 2000	**Photochemical Smog in Berlin-Brandenburg: An Investigation with the Atmosphere-Chemistry Model GESIMA** Susanne E. Bauer
Examensarbeit Nr. 82 Juli 2001	**Komponenten des Wasserkreislaufs in Zyklonen aus Satellitendaten –Niederschlagsfallstudien-** Christian-Philipp Klepp
Examensarbeit Nr. 83 Juli 2001	**Aggregate models of climate change: development and applications** Kurt Georg Hooss
Examensarbeit Nr. 84 Februar 2002	**Ein Heterodyn-DIAL System für die simultane Messung von Wasserdampf und Vertikalwind: Aufbau und Erprobung** Stefan Lehmann
Examensarbeit Nr. 85 April 2002	**Der Wasser- und Energiehaushalt der arktischen Atmosphäre** Tido Semmler

ISSN 0938 - 5177